

## ABSTRACT

Title of dissertation: CHARGE FORM FACTOR OF  
THE NEUTRON THROUGH  $\vec{d}(\vec{e}, e'n)$   
AT  $Q^2 = 1.0 \text{ (GeV}/c)^2$

Nikolai Aleksandrovich Savvinov, Doctor of Philosophy, 2003

Dissertation directed by: Professor James J. Kelly  
Department of Physics

Elastic electromagnetic form factors of the nucleon are of fundamental importance for our understanding of its internal structure. Experiment E93-026 at the Thomas Jefferson National Accelerator Facility (JLab) determined the electric form factor of the neutron,  $G_E^n$ , through quasielastic  $\vec{d}(\vec{e}, e'n)p$  scattering using a longitudinally polarized electron beam and a frozen polarized  $^{15}\text{ND}_3$  target. The knocked out neutrons were detected in a segmented plastic scintillator detector in coincidence with the scattered electrons. The form factor was extracted by comparing the experimental beam-target asymmetry with full theoretical calculations based on different values of  $G_E^n$ . The dissertation discusses the experimental setup, data acquisition and analysis for the  $Q^2 = 1.0 \text{ (GeV}/c)^2$  point, and implications of the experimental results for our understanding of the nucleon electromagnetic structure.

CHARGE FORM FACTOR OF THE NEUTRON

THROUGH  $\vec{d}(\vec{e}, e'n)$  AT  $Q^2 = 1.0 (GeV/c)^2$

by

Nikolai Aleksandrovich Savvinov

Dissertation submitted to the Faculty of the Graduate School of the  
University of Maryland, College Park in partial fulfillment  
of the requirements for the degree of  
Doctor of Philosophy  
2003

Advisory Committee:

Professor James J. Kelly, Chair/Advisor  
Professor Xiangdong Ji  
Professor Elizabeth J. Beise  
Professor Philip G. Roos  
Professor Alice C. Mignerey

© Copyright by  
Nikolai Aleksandrovich Savvinov  
2003

To the memory of my father.

# Contents

<b>1</b>	<b>Introduction</b>	<b>1</b>
<b>2</b>	<b>Basic concepts and definitions</b>	<b>5</b>
2.1	Nucleon form factors . . . . .	5
2.2	Charge and magnetization densities . . . . .	9
2.3	Charge radius of the neutron . . . . .	13
<b>3</b>	<b>Previous <math>G_E^n</math> experiments</b>	<b>15</b>
3.1	Rosenbluth separation . . . . .	15
3.2	Unpolarized elastic $e - d$ scattering . . . . .	18
3.3	Hybrid analysis of the elastic $e - d$ data . . . . .	22
3.4	Polarized measurements . . . . .	23
<b>4</b>	<b>Experimental technique</b>	<b>27</b>
4.1	Polarized scattering from a free nucleon . . . . .	27
4.2	Deuteron target . . . . .	29
<b>5</b>	<b>Experimental setup</b>	<b>34</b>

5.1	Polarized electron beam . . . . .	35
5.1.1	Accelerator . . . . .	35
5.1.2	Hall C beamline . . . . .	37
5.1.3	Raster magnets . . . . .	40
5.1.4	Chicane magnets . . . . .	41
5.2	Hall C High Momentum Spectrometer . . . . .	41
5.3	Polarized target . . . . .	44
5.3.1	Magnet . . . . .	44
5.3.2	Refrigerator . . . . .	45
5.3.3	Insert . . . . .	47
5.3.4	Microwaves . . . . .	47
5.3.5	NMR and data acquisition . . . . .	48
5.3.6	Target material . . . . .	49
5.4	Neutron detector . . . . .	50
5.4.1	Configuration and position . . . . .	51
5.4.2	Gain monitoring . . . . .	54
5.4.3	Gain matching . . . . .	55
5.5	Electronics and data acquisition . . . . .	55
5.5.1	Electronics . . . . .	56
5.5.2	Triggers and events . . . . .	60

**6 Analysis software 65**

6.1	Overview . . . . .	65
6.2	Syncfilter . . . . .	67
6.3	Hall C replay engine . . . . .	69
6.3.1	HMS event reconstruction . . . . .	70
6.3.2	Neutron detector event reconstruction . . . . .	73
6.3.3	Kinematic calculations . . . . .	78
6.4	Inclusive simulations . . . . .	81
6.4.1	Cross-section model . . . . .	81
6.4.2	QFS parameters . . . . .	85
6.4.3	Deuterium cross sections . . . . .	85
6.4.4	Radiative effects . . . . .	87
6.4.5	Acceptance effects . . . . .	92
6.4.6	Composite target models . . . . .	94
6.4.7	Comparison of simulation results to experimental data . . . . .	95
6.5	Coincidence Monte Carlo simulations . . . . .	96
6.5.1	Basics of MCEEP . . . . .	97
6.5.2	Customization of MCEEP . . . . .	101
6.5.3	Output and results . . . . .	104
<b>7</b>	<b>Data analysis</b>	<b>106</b>
7.1	Data replay . . . . .	106
7.1.1	Runs selection . . . . .	107

7.1.2	Detector calibrations . . . . .	108
7.1.3	Replay procedure . . . . .	109
7.2	Cut optimization . . . . .	110
7.3	Target polarization . . . . .	113
7.3.1	Baseline subtraction . . . . .	113
7.3.2	TE constants . . . . .	115
7.4	Beam polarization . . . . .	116
7.4.1	Hall A current leakage . . . . .	117
7.4.2	Results . . . . .	118
7.5	Packing fraction . . . . .	120
7.5.1	Method of determination . . . . .	120
7.5.2	Event selection . . . . .	121
7.5.3	Procedure and results . . . . .	122
7.6	Dilution factor . . . . .	124
7.6.1	Pion contamination . . . . .	126
7.6.2	Misorientation of the 4K shield . . . . .	126
7.6.3	Stick 3 rotation . . . . .	127
7.6.4	Results . . . . .	131
7.7	Corrections . . . . .	132
7.7.1	Radiative corrections . . . . .	132
7.7.2	Paddle inefficiency . . . . .	133

7.7.3	Electronics deadtime . . . . .	135
7.7.4	Accidental background subtraction . . . . .	136
7.7.5	Multi-step reactions contamination . . . . .	139
7.8	Results . . . . .	141
7.8.1	Extraction of $G_E^n$ . . . . .	141
7.8.2	Kinematic uncertainties . . . . .	146
7.8.3	Other experimental uncertainties . . . . .	146
7.8.4	Reaction mechanism dependence . . . . .	148
7.8.5	Parametrization of $G_E^n$ . . . . .	149
<b>8</b>	<b>Theoretical predictions of <math>G_E^n</math></b>	<b>151</b>
8.1	Asymptotic behavior . . . . .	151
8.1.1	Dimensional scaling laws . . . . .	151
8.1.2	Perturbative QCD calculations. . . . .	153
8.1.3	Comparison with experiment . . . . .	157
8.2	Dispersion relations . . . . .	162
8.3	Vector Meson Dominance . . . . .	163
8.4	Quark models . . . . .	166
8.4.1	Nonrelativistic quark models . . . . .	166
8.4.2	Relativistic constituent quark models . . . . .	168
8.5	Diquark model . . . . .	172
8.6	Soliton model . . . . .	177

8.7 Overview . . . . .	179
<b>9 Discussion</b>	<b>183</b>
<b>10 Summary and outlook</b>	<b>188</b>
<b>A Principles of operation of the E93026 polarized target</b>	<b>190</b>
A.1 Dynamic nuclear polarization . . . . .	190
A.2 NMR polarization measurement . . . . .	192
<b>B Measuring beam polarization with the Hall C Møller polarimeter</b>	<b>196</b>
<b>Bibliography</b>	<b>198</b>

# List of Figures

2.1	One-photon-exchange diagram for electron-nucleon scattering. . . . .	6
2.2	Nucleon charge and magnetization densities. . . . .	11
3.1	Longitudinal-transverse separation. . . . .	16
3.2	Best Rosenbluth data for $G_E^n$ . . . . .	18
3.3	Elastic measurements of $G_E^n$ . . . . .	20
3.4	Sick and Schiavilla's extraction of $G^n$ . . . . .	23
3.5	Polarized measurements of $G_E^n$ . . . . .	26
4.1	Polarized electron-nucleon scattering. . . . .	29
4.2	Meson exchange currents . . . . .	31
4.3	Isobar currents . . . . .	31
4.4	The vector beam-target asymmetry $A_{ed}^V$ . . . . .	33
5.1	Schematic view of the JLab accelerator . . . . .	36
5.2	Hall C beamline elements . . . . .	38
5.3	Layout of the Hall C Møller polarimeter . . . . .	39
5.4	Rastered beam . . . . .	41

5.5	Chicane magnets. . . . .	42
5.6	Hall C High Momentum Spectrometer . . . . .	43
5.7	Main components of the UVa polarized target. . . . .	45
5.8	Target cryostat and magnet. . . . .	46
5.9	Target ladder carrying target cells. . . . .	48
5.10	The neutron detector. . . . .	52
5.11	HMS trigger electronics. . . . .	57
5.12	Neutron detector electronics. . . . .	58
5.13	Laser trigger . . . . .	59
5.14	Helicity scaler electronics. . . . .	60
5.15	Trigger setup. . . . .	63
6.1	Data analysis software. . . . .	66
6.2	A proton event in the neutron detector . . . . .	75
6.3	QFS versus NE4 data for transverse scattering . . . . .	88
6.4	Comparison between SLAC NE3 data and simulations . . . . .	91
6.5	HMS momentum acceptance. . . . .	93
6.6	HMS acceptance . . . . .	93
6.7	Comparison between single-arm data and simulation results. . . . .	96
6.8	Coincidence Monte Carlo compared to data . . . . .	105
7.1	Figure of merit for different kinematic cuts . . . . .	111
7.2	NMR signal on different stages of the offline analysis. . . . .	114

7.3	TE calibration constants for various groups . . . . .	115
7.4	Results of Møller measurements and their parameterizations. . . . .	119
7.5	Packing fraction for stick 4 . . . . .	123
7.6	The $Z_{BEAM}$ distribution . . . . .	128
7.7	A top view of the cup inside the 4K shield . . . . .	129
7.8	Target insert rotation . . . . .	130
7.9	The number of HMS events as a function of the gate width . . . . .	136
7.10	Hits meantime distribution . . . . .	137
7.11	Relative track excess versus the background level . . . . .	139
7.12	The $G_E^n$ extraction plot. . . . .	143
7.13	Statistical properties of neutron asymmetries . . . . .	144
7.14	Proton asymmetries . . . . .	145
7.15	Results of JLab E93-026 compared with other experimental data. . . . .	150
8.1	Elastic $e - N$ scattering amplitude at high $Q^2$ . . . . .	152
8.2	A two-gluon exchange hard scattering diagram for $F_2^p$ . . . . .	156
8.3	Asymptotic behavior of the proton magnetic form factor . . . . .	158
8.4	Recent data on the proton form factor ratio. . . . .	159
8.5	Magnetic form factors of the nucleon . . . . .	181
8.6	The $G_E/G_M$ ratio for the proton. . . . .	182
8.7	The electric form factor of the neutron . . . . .	182
9.1	Charge and magnetization densities of the neutron . . . . .	187

A.1	The effect of spin-spin interaction on levels and states of an electron-nucleon system in an external magnetic field . . . . .	193
A.2	Positive and negative polarization enhancement . . . . .	194

# Chapter 1

## Introduction

“What does matter consist of?” is one of the most ancient and fundamental questions. It is more than just a mere curiosity; one hopes that the myriad phenomena around us and thousands of empirical laws governing them can be reduced to a few basic constituents and the rules of their interaction. This was the basis of the determinism of the XVII century – an attitude that claimed that everything was calculable and predictable. The XX century, with establishing of probabilistic nature of the microscopic world, with discovery of deterministic chaos, and with the realization of the enormous computational difficulties that may arise in application of simple theories to practice, has shattered this optimism. Still, there is no doubt that understanding the primary constituents of matter will shed light on the most exciting and challenging puzzles of the modern science.

During the last two centuries science has made a lot of progress in this direction. It has been known for more than a century that ordinary matter is made of atoms. It has also been known since Rutherford’s famous experiment in 1911

that an atom consists of a heavy nucleus surrounded by light electrons. Further experiments that followed in 1920-s and 1930-s revealed that nuclei, in their turn, are comprised of *protons* and *neutrons*, two particles similar in mass and strong interaction properties, but differing in electric charge and magnetic moment. And finally, vast experimental evidence starting with the hard scattering experiments of 1960-s has convinced the scientific community that nucleons (as well as all other strongly interacting particles) consist of point-like quarks interacting by means of gluon exchange, even though quarks have never been observed directly.

The answer to the next important question, *how* matter is made, i.e. how the elementary constituents interact strongly with each other, is to be given by quantum chromodynamics (QCD). Even though the QCD Lagrangian is known, it is very hard to solve it because of the extreme nonlinearity of the problem<sup>1</sup>. The only method which allows model-independent QCD calculations to be made from first principles, so-called lattice QCD, has only recently produced promising results. A more practical approach to the problems of physics of strong interactions is to construct models that emphasize the most important aspects of QCD, and to test them by confronting them with the data.

Much about the electromagnetic structure of the nucleons can be learned by probing them with virtual photons in electron-nucleon scattering. In particular, it

---

<sup>1</sup>At high momentum transfers the *asymptotic freedom* of QCD (i.e. weakening of the strong interaction due to screening of the color charge at  $Q^2 \rightarrow \infty$ ) allows to solve it perturbatively. These results are often accurate only to logarithmic corrections and it is not always clear at what  $Q^2$  the asymptotic behavior sets in.

gives access to electromagnetic form factors of the nucleon (EMFFN). These form factors not only provide a testing ground for QCD-inspired models, but also are important in many areas of particle and nuclear physics, including nuclear charge radii, parity-violating experiments, and many others.

Of the four elastic form factors of the nucleon, the charge form factor of the neutron  $G_E^n$  is perhaps the most intriguing one. If the SU(6) spin-flavor symmetry of QCD were exact, this quantity would vanish at all momentum transfers. Therefore the non-zero experimental values of  $G_E^n$  are a clear signature of dynamical SU(6)-breaking effects<sup>2</sup>, and thus by studying  $G_E^n$  we can achieve a better understanding of spin-dependent interactions between the quarks.

At the same time,  $G_E^n$  has proven to be the most elusive form factor to measure. The reason for that is fourfold: first, since there is no free neutron target, experiments on neutron form factors inevitably involve model-dependent nuclear corrections. Second, since neutrons do not carry electric charge, they are much harder to detect than the protons. Third, time-of-flight momentum measurements for the neutron are usually less accurate than the magnetic spectrometer measurements for the proton. Fourth, due to its small magnitude, the electric form factor is completely overshadowed by a much larger contribution from the magnetic form factor in the cross section, at least at experimentally accessible  $Q^2$ .

Therefore, the large theoretical demand for the accurate information on  $G_E^n$

---

<sup>2</sup>Recently it has been shown [1] that kinematic SU(6) breaking via Melosh rotations can be important, too. However, the value of  $G_E^n$  cannot be explained by relativistic effects alone.

(especially at high  $Q^2$ ) is far from being satisfied. A number of new-generation experiments on  $G_E^n$  employing spin degrees of freedom are currently underway, recently completed, or expected to run in near future. These experiments, being less susceptible to the model dependence and various systematic errors than traditional cross-section measurements, are bringing our knowledge of  $G_E^n$  to a new level. The experiment described here is a part of this experimental program.

The rest of the dissertation is organized as follows: in the next chapter (Chapter 2) we will present the definition and interpretation of the elastic form factors. In Chapter 3 we will discuss previous measurements of the neutron charge form factor. As the last preparation for the discussion of the experiment, we introduce the basics of polarized electron-deuteron scattering in Chapter 4. Chapters 5-10 deal with the experimental details; Chapter 5 describes the experimental setup, Chapter 6 describes the software used in the data analysis, and Chapter 7 is devoted to the data analysis itself and its results. In Chapter 8 we will review various theoretical models and calculations on the subject. Chapter 9 discusses the implications of our and other recent experimental results for the electromagnetic structure of the nucleon. The summary and the outlook are given in the Chapter 10.

# Chapter 2

## Basic concepts and definitions

### 2.1 Nucleon form factors

Let us consider electron-nucleon scattering. Since the electromagnetic interaction is relatively weak (the electromagnetic coupling constant  $\alpha \ll 1$ ), it can be treated perturbatively. In terms of Feynman diagrams, rapid convergence of the perturbation series means that the contribution of the one-virtual-photon-exchange diagram (see Figure 2.1) dominates<sup>1</sup>. In this approximation, the invariant matrix element becomes [2]

$$\mathcal{M} = \frac{4\pi\alpha}{Q^2} \langle \vec{k}_f \lambda_f | j_\mu^e | \vec{k}_i \lambda_i \rangle \langle \vec{p}_f s_f | j_\mu^N | \vec{p}_i s_i \rangle \quad (2.1)$$

where  $\alpha = 1/137$  is the fine structure constant,  $Q^2 = -q_\mu q^\mu$  is the four-momentum transfer squared,  $k_{i,f}$  and  $\lambda_{i,f}$  are the momentum and helicity of the initial and the final state of the electron,  $p_{i,f}$  and  $s_{i,f}$  denote the initial and final spin and

---

<sup>1</sup>The discrepancy between  $G_E^p/G_M^p$  measurements via Rosenbluth separation and with recoil polarimetry have caused some concern with about validity of this approximation. See also the footnote on page 157.

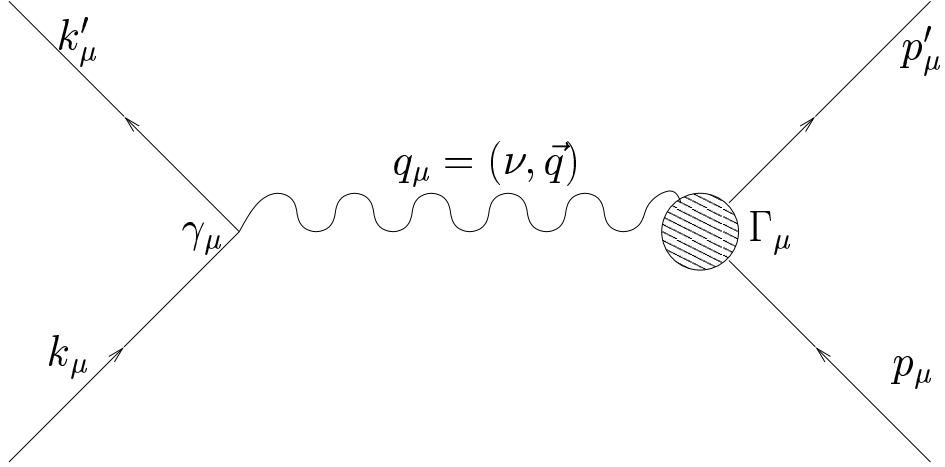


Figure 2.1: One-photon-exchange diagram for electron-nucleon scattering.

momentum of the struck nucleon, and  $j_\mu^A$  is the current operator for the particle  $A = \{e, N\}$ . It is convenient to introduce lepton and nucleon response tensors as

$$\eta_{\mu\nu}^A = N_A \langle j_\mu^A j_\nu^{A\dagger} \rangle \quad (2.2)$$

where  $N_A$  is a constant normalization factor ( $2m_e^2$  for the electron and  $1/(2m_N^2)$  for the nucleon) and angle brackets denote averaging over the initial states and summing over the final states.

For the electron the unpolarized current is given by

$$\langle \vec{k}_f \lambda_f | j_\mu^e | \vec{k}_i \lambda_i \rangle = \bar{u}_f \gamma_\mu u_i. \quad (2.3)$$

Using (2.3), spinor normalization relations and trace theorems it is straightforward

to calculate the leptonic tensor for unobserved helicities to be

$$\eta_{\mu\nu}^e = 2(k_{i\mu}k_{f\nu} + k_{f\mu}k_{i\nu} - k_i k_f g_{\mu\nu}), \quad (2.4)$$

where the electron mass has been neglected.

Let us now turn to the electromagnetic current of the nucleon. If the nucleon were a point-like particle then we would obtain (2.3) for the nucleon current and eventually the famous Mott formula (2.7) for the scattering cross-section. However, as indicated by anomalous magnetic moments of the neutron and the proton, the nucleon has additional electromagnetic structure. This structure can be parametrized in terms of form factors  $F_i(Q^2)$  such that

$$\begin{aligned} j_\mu^N &= e\bar{u}(\vec{p}_f)[\gamma_\mu F_1 + (\kappa/2m_N)F_2 i\sigma_{\mu\nu}q^\nu + q_\mu F_3 \\ &\quad + \gamma_\mu \gamma_5 F_4 + q_\mu \gamma_5 F_5]u(\vec{p}_i), \end{aligned} \quad (2.5)$$

where  $\kappa$  and  $m_N$  are the anomalous magnetic moment and the mass of the nucleon, correspondingly. Parity and current conservation rule out terms with  $F_3$ ,  $F_4$  and  $F_5$ , and the remaining terms result in the following expression for the electron-nucleon scattering cross-section:

$$\frac{d\sigma}{d\Omega_{lab}} = \sigma_{Mott} f_{rec} \left[ \left( F_1^2 + \frac{\kappa^2 Q^2}{4m_N^2} F_2^2 \right) + \frac{Q^2}{2m_N^2} (F_1 + \kappa F_2)^2 \tan^2 \frac{\theta}{2} \right], \quad (2.6)$$

where

$$\sigma_{Mott} = \frac{\alpha^2 \cos^2(\theta/2)}{4E_i^2 \sin^4(\theta/2)} \quad (2.7)$$

is the cross-section of scattering from a point-like particle,  $\theta$  is the scattering angle,  $E_{i,f}$  is the initial and final energy of the electron, and  $f_{rec} = E_f/E_i$  is a recoil factor.

The functions  $F_1(Q^2)$  and  $F_2(Q^2)$  are known as Dirac and Pauli form factors of the nucleon. For practical purposes it is more convenient to use linear combinations of  $F_1(Q^2)$  and  $F_2(Q^2)$  (so called Sachs form factors), which do not give rise to an interference term in the expression for the cross-section:

$$G_E(Q^2) = F_1(Q^2) - \tau \kappa F_2(Q^2) \quad (2.8)$$

$$G_M(Q^2) = F_1(Q^2) + \kappa F_2(Q^2), \quad (2.9)$$

where  $\tau = Q^2/4m_N$  is a kinematic factor. Rewritten in terms of Sachs form factors formula (2.6) becomes the famous Rosenbluth formula:

$$\frac{d\sigma}{d\Omega} = \sigma_{Mott} f_{rec} \left[ \frac{G_E^2(Q^2) + \tau G_M^2(Q^2)}{1 + \tau} + 2\tau G_M^2(Q^2) \tan^2 \frac{\theta}{2} \right]. \quad (2.10)$$

Finally, one often uses isotopic form factors of the nucleon:

$$G_{E,M}^{IS} = \frac{1}{2}(G_{E,M}^p + G_{E,M}^n) \quad (2.11)$$

$$G_{E,M}^{IV} = \frac{1}{2}(G_{E,M}^p - G_{E,M}^n), \quad (2.12)$$

where  $G_{E,M}^{IV}$  and  $G_{E,M}^{IS}$  are the isovector and isoscalar form factors, correspondingly.

## 2.2 Charge and magnetization densities

In order to understand the physical meaning of the EMFFN, let us consider classical electromagnetism. For instance, the diffraction pattern from an object with a non-trivial shape differs from that for a point-like obstacle by a *factor* which describes the shape or *form* of the object (a *form-factor*). The classical form-factor is just the Fourier transform of the optical density of the object (one often says that the diffraction pattern is a spatial Fourier transform of the object).

As we shall presently see, in quantum mechanics there exists a very similar relation between the charge form factor and the spatial charge density. However, in the relativistic case, in general there is more than one form factor: for example, for the nucleons, as we have already seen, there are two. This is due to the purely relativistic phenomenon of spin. In general, the electromagnetic structure of a spin- $j$  object has to be described by  $2j + 1$  form factors associated with it.

To clarify the meaning of the EMFFN let us consider electron-nucleon scatter-

ing in the so-called Breit (or “brick wall”) frame, defined by the requirement that the momenta of the incident and the scattered electron have equal magnitudes and opposite directions. In this frame, there is no energy transfer and therefore  $Q^2 = q^2$ . With this, the matrix elements of the electromagnetic current in the Breit frame simplify to [3]:

$$\begin{aligned}\langle \vec{q}/2, s_f | j_0^N | -\vec{q}/2, s_i \rangle &= 2M G_E(q^2) \delta_{s_f, s_i}, \\ \langle \vec{q}/2, s_f | \vec{j}^N | -\vec{q}/2, s_i \rangle &= 2M G_M(q^2) \chi_f^\dagger i\vec{\sigma} \times \vec{q} \chi_i,\end{aligned}\tag{2.13}$$

where  $\chi_{i,f}$  are initial and final state spinors of the nucleon. Equations 2.13 can be used to show that  $G_E$  is related to a close analog of the classical charge density  $\rho(\vec{r})$  by [4]

$$\rho(\vec{r}) = \int \frac{d^3q}{(2\pi)^3} e^{-i\vec{q}\vec{r}} \frac{M}{E(\vec{q})} G_E(q^2),\tag{2.14}$$

where  $E(\vec{q})$  is the neutron energy in the Breit frame defined by  $\vec{q}$ . A similar relationship can be written for the magnetization density and the magnetic form factor.

One should be cautioned, however, that the interpretation of the charge form factor of the neutron as a measure of the charge density distribution is non-relativistic. In reality the physical meaning of the  $G_E^n$  is obscured by relativistic effects, because one needs to boost the charge density (2.14) from the Breit frame to the rest frame of the neutron, and the boost is interaction-dependent in the instant form formulation.

Some difficulties can be circumvented by using light-cone or point-form formu-

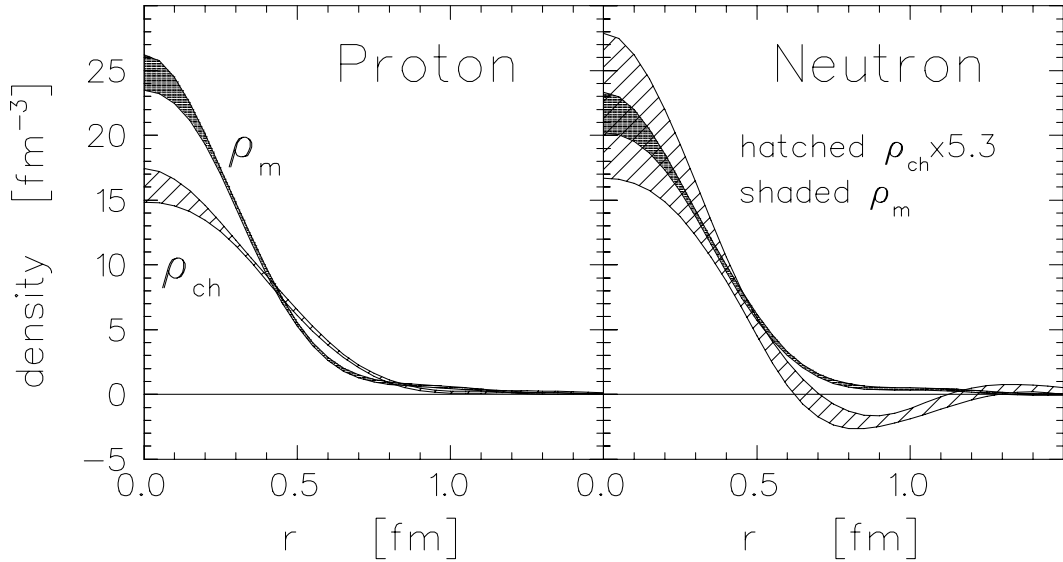


Figure 2.2: Nucleon charge and magnetization densities.

lations, where boost generators are kinematical. However, on the fundamental level, the problem in the interpretation of form factors is due to the fact that EMFFN are defined via transition matrix elements between states with different momenta, and therefore are related to *transition* (rather than rest frame) charge and magnetization densities. Kelly [5] has studied various relativistic prescriptions for the density extraction recently used in the literature. He found that all of them can be represented in the form:

$$\tilde{\rho}_{ch}(k) = G_E(Q^2)(1 + \tau)^{\lambda_E} \quad (2.15)$$

$$\mu \tilde{\rho}_m(k) = G_M(Q^2)(1 + \tau)^{\lambda_M}, \quad (2.16)$$

where the intrinsic form factors  $\tilde{\rho}(k)$  are related to the densities by a usual Fourier

transform

$$\tilde{\rho}(k) = \frac{2}{\pi} \int_0^\infty dr r^2 j_0(kr) \rho(r), \quad (2.17)$$

and  $k$  is the intrinsic spatial frequency defined as

$$k^2 = \frac{Q^2}{1 + \tau}. \quad (2.18)$$

The choice of parameters  $\lambda_E$  and  $\lambda_M$  is determined by the model: soliton models of Ji [6] and Holzwarth [7] use  $\lambda_E = 0$  and  $\lambda_M = 1$ , and the cluster models of Licht and Pignamenta [8] and that of Mitra and Kumari [9] use  $\lambda_E = \lambda_M = 1$  and  $\lambda_E = \lambda_M = 2$ , correspondingly. The form factor data were fitted using complete sets of functions. Two expansions were considered, Fourier-Bessel expansion (FBE) and Laguerre-Gaussian expansion (LGE). The paper is focused on the case  $\lambda_E = \lambda_M = 2$  (which ensures correct asymptotic behaviour of the fits), but other choices of parameters were also studied. As expected, it has been found that the results are practically independent of the choice of the expansion basis. The choice of parameters  $\lambda_E$  and  $\lambda_M$  only affected the details of the density distributions, while all essential features were independent of the model. The results of this study are shown in Figure 2.2. The extracted densities are rather “soft”, in contrast to the results of non-relativistic inversions, which produce an unphysical cusp at the origin. Suppression of the cusp is a result of a high  $k$  constraint  $\rho(k) \lesssim \rho(k_m)k^{-4}$  to get the normalization right.

## 2.3 Charge radius of the neutron

If one starts with the Fourier integral representation of the neutron charge form factor

$$G_E(Q^2) = \int d^3r \rho(r) e^{-i\vec{q}\cdot\vec{r}},$$

and then expands both sides into a Taylor series around  $q \rightarrow 0$  (since we are working in the Breit frame,  $Q^2 = q^2 \rightarrow 0$ ):

$$G_E(Q^2) = G_E(0) + Q^2 \left. \frac{dG_E(Q^2)}{dQ^2} \right|_{Q^2=0} + \dots = Q^2 \left. \frac{dG_E(Q^2)}{dQ^2} \right|_{Q^2=0} + \dots$$

$$e^{-i\vec{q}\cdot\vec{r}} = 1 - i\vec{q}\cdot\vec{r} + \frac{1}{2}(i\vec{q}\cdot\vec{r})^2 + \dots$$

and calculates resulting integrals, it is straightforward to see that the first two terms on the right hand side vanish (first one due to zero net charge and the second one due to parity considerations), whereas for the remaining terms one has:

$$Q^2 \left. \frac{dG_E}{dQ^2} \right|_{Q^2=0} = \int \frac{1}{2} (iqr)^2 \cos^2 \theta \rho(r) d^3r = -\frac{2\pi}{3} Q^2 \int r^4 \rho(r) dr = -\frac{1}{6} Q^2 r_{En}^2, \quad (2.19)$$

where  $r_{En}^2$  is the neutron charge radius  $r_{En}^2 = \int r^2 \rho(r) d^3r$ . Cancelling a factor of  $Q^2$  and rearranging the terms we have for the neutron charge radius

$$r_{En}^2 = -6 \left. \frac{dG_E}{dQ^2} \right|_{Q^2=0}. \quad (2.20)$$

If one uses Equation 2.9 to express the  $r_{En}^2$  in terms of Dirac and Pauli form factors, one gets for  $Q^2 \approx 0$

$$G_E^n \approx -\frac{1}{6}r_{En}^2 Q^2 = F_1^n - \kappa_n \frac{Q^2}{4m^2} F_2^n, \quad (2.21)$$

and further, remembering that  $F_2^n(0) = 1$  and  $\kappa_n = \mu_n$ , and introducing the radius  $r_{1n}$  associated with the Dirac form factor  $r_{1n}^2 = -6 \frac{dF_1(Q^2)}{dQ^2}$ ,

$$r_{En}^2 = r_{1n}^2 + \frac{3\mu_n}{2m^2}. \quad (2.22)$$

The second term in Equation 2.22 is known as the *Foldy term* and takes its origin in so-called *zitterbewegung* (jitter motion) of the nucleon. The value of the Foldy term ( $-0.126 \text{ fm}^2$  [10]) is very close to the experimental value of the charge radius ( $-0.113 \pm 0.005 \text{ fm}^2$ ), which made some theorists believe that  $G_E^n$  does not describe the rest frame charge distribution. However, Isgur [11] has shown that if some simplifying assumptions are made, this Foldy terms exactly cancels against a term coming from the Dirac form factor. The discussion whether the Foldy term is dominating  $G_E^n$  or it cancels via Isgur's cancellation mechanism, is still open.

# Chapter 3

## Previous $G_E^n$ experiments

### 3.1 Rosenbluth separation

One simple way of measuring nucleon form factors is suggested by the Rosenbluth formula (2.10): by measuring the electron-nucleon scattering cross-section for two different kinematics with common  $Q^2$  one obtains two linear equations for squares of the form factors. This approach has a simple graphical interpretation, with the help of so-called reduced cross-section

$$\sigma_R = \frac{d\sigma}{d\Omega} \frac{\epsilon(1+\tau)}{\sigma_{Mott}} = G_M^2(Q^2) + (\epsilon/\tau)G_E^2(Q^2),$$

where  $\epsilon = [1 + 2(1 + \tau) \tan^2 \theta_e/2]^{-1}$  is the transverse polarization of the virtual photon. If one plots  $\sigma_R$  versus  $\epsilon$  for a fixed  $Q^2$  (and therefore  $\tau$ ), then the slope of the line is proportional to  $G_E^2$ , while the intercept gives  $G_M^2$  (see Figure 3.1).

This technique can be applied directly to protons by using a hydrogen target. For the neutron, the simplest target available is deuteron. In the case of quasifree

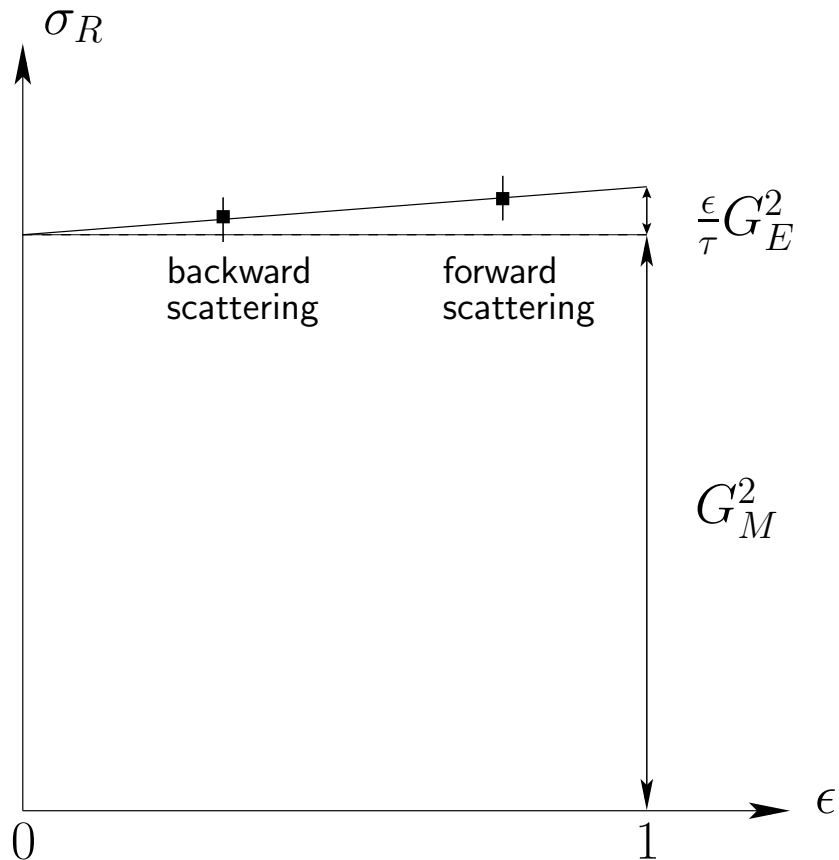


Figure 3.1: Longitudinal-transverse separation.

scattering the cross-section is, to a good approximation, an incoherent sum of scattering cross-sections from individual nucleons<sup>1</sup>. The proton contribution has to be either subtracted or eliminated by experimental means (for example, by making a coincidence with the knocked-out neutron or an *anti*-coincidence with the knocked-out proton), thus giving rise to additional systematic uncertainties.

Several such measurements were done in 1960's and 1970's (see [2] for a review), following the pioneering work by Hofstadter and collaborators [12]. The results are

---

<sup>1</sup>A discussion of validity of the impulse approximation with application to polarized electron-deuteron scattering can be found in 4.2.

inconclusive and in most of the works the authors had obtained negative values of  $(G_E^n)^2$  for one or more data points. In 1992 the Rosenbluth approach was again applied to neutron form factors by Lung *et al.* [13]. Despite improvements in the beam technology, their results suffer from very large uncertainties, and for the higher- $Q^2$  points the measured values of  $(G_E^n)^2$  were again found to be negative.

The reason for failure of the Rosenbluth method for the neutron is unfavorable error propagation due to the dominance of the  $G_M^n$  term in the cross-section. The difficulties of the method are illustrated in Figure 3.1. Since  $(G_M^n)^2 \gg (G_E^n)^2$  (at least for experimentally accessible kinematics), the  $\epsilon/\tau(G_E^n)^2$  term does not contribute more than a few percent to  $\sigma_R$  (e.g. about 4% at  $Q^2 = 1$  (GeV/c)<sup>2</sup>). The slope of the Rosenbluth fit, being almost parallel to the abscissa, receives a very large error magnification factor (a few percent error in the cross section will translate into a 200% uncertainty in  $(G_E^n)^2$ ).

Under these conditions, an exact measurement of the slope of the Rosenbluth plot requires not only high accuracy of the cross-section measurement for as widely separated  $\epsilon$  as possible, but also a very tight control over contributions from many-body currents.

A plot of best Rosenbluth results for  $G_E^n$  is given in Figure 3.2. For comparison with other data we will later present in this chapter, a commonly used Galster parametrization is also plotted.

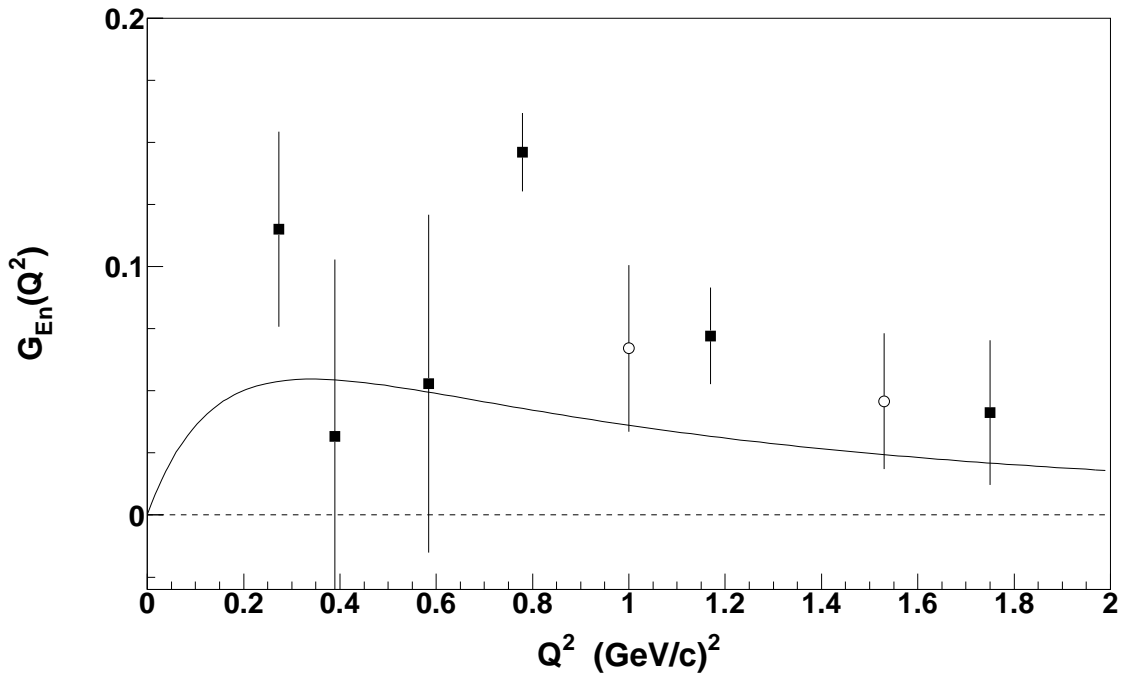


Figure 3.2: Best Rosenbluth data for  $G_E^n$ . Symbols are: filled squares [14], [15]. The solid line is the standard Galster fit [16].

### 3.2 Unpolarized elastic $e - d$ scattering

Since the deuteron is a spin-1 particle, the most general form of conserved current without parity and time-reversal violating terms involves three form factors:  $G_E$  (electric),  $G_Q$  (quadrupole) and  $G_M$  (magnetic). By introducing structure functions  $A(Q^2)$  and  $B(Q^2)$  one can bring the expression for the  $e - d$  scattering cross-section into a form resembling the Rosenbluth formula:

$$\frac{d\sigma}{d\Omega} = \sigma_{Mott} f_{rec} [A(Q^2) + B(Q^2) \tan^2(\theta_e/2)]. \quad (3.1)$$

The deuteron structure functions can be expressed in terms of the form factors of the deuteron, as follows:

$$A(Q^2) = G_E^2(Q^2) + \frac{8}{9}\tau^2 G_Q^2(Q^2) + \frac{2}{3}\tau G_M^2(Q^2) \quad (3.2)$$

$$B(Q^2) = \frac{4}{3}\tau(1 + \tau)^2 G_M^2(Q^2), \quad (3.3)$$

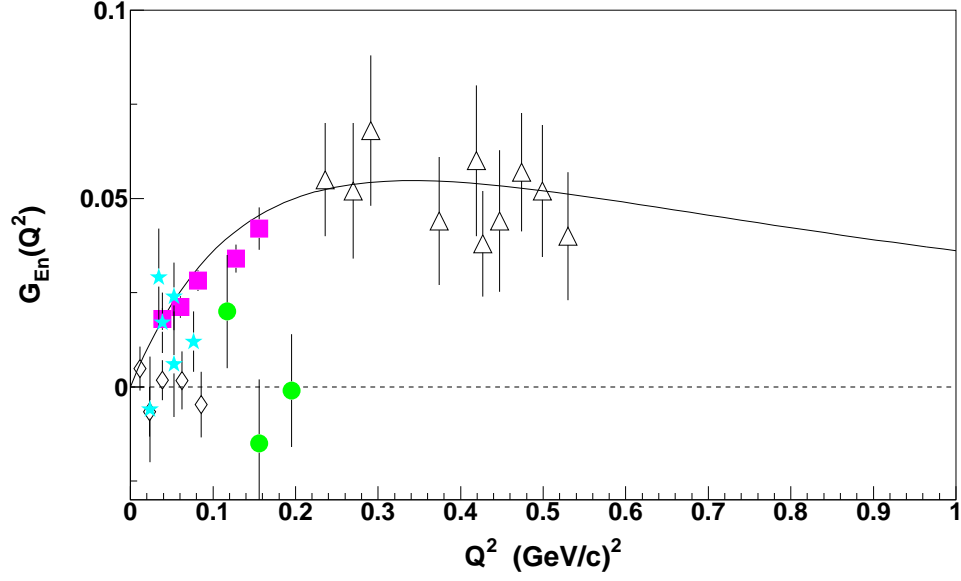
where  $\tau$  is a kinematic factor,  $\tau = Q^2/4M_D$ . In the non-relativistic impulse approximation the deuteron quadrupole and charge form factors become directly proportional to the isoscalar charge form factor  $G_E^s$  with the proportionality factors  $C_E$  and  $C_Q$  known as "body form factors" or "structure integrals":

$$C_E = \int_0^\infty [u^2(r) + w^2(r)] j_0(\frac{1}{2}qr) dz \quad (3.4)$$

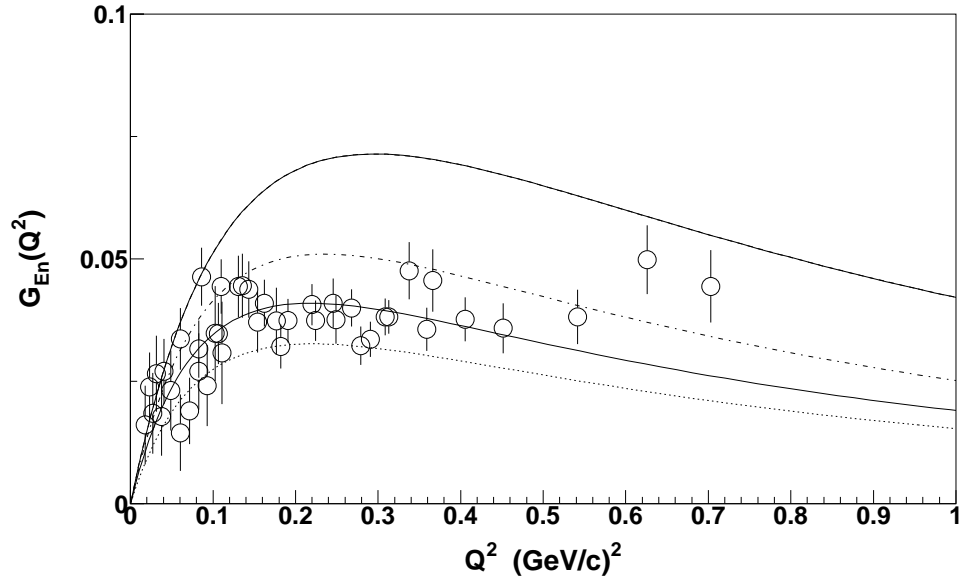
$$C_Q = \frac{3}{\tau\sqrt{2}} \int_0^\infty \left[ u(r)w(r) - \frac{w^2(r)}{2\sqrt{2}} \right] j_2(\frac{1}{2}qr) dr. \quad (3.5)$$

These depend on the deuteron  $S$ - and  $D$ -wave functions  $u(r)$  and  $w(r)$  and therefore introduce model-dependence into the method. The procedure for determining  $G_E^n$  from the elastic  $e - d$  cross-section consists of a few steps:

- determining structure function  $A(Q^2)$  using Rosenbluth separation
- subtracting from it the small contribution coming from  $G_{M_n}$
- calculating the IA value of  $A(Q^2)$  as  $A_{exp}(Q^2) - \Delta A_{MEC}(Q^2) - \Delta A_{rel}(Q^2)$
- picking an  $N - N$  interaction potential and calculating structure integrals



(a)



(b)

Figure 3.3: Elastic measurements of  $G_E^n$ , (a) – 1960-1980's data: triangles [16], diamonds [17], stars [18], circles [19], squares [20], the solid line is the standard Galster parametrization; (b) – 1990 data of Platchkov *et al.* [21] extracted with the Paris potential. Lines are fits to the same data extracted with Paris (solid), RSC (dotted), Argonne (dash-dotted), Nijmegen (dash-dotted) potentials.

- calculating the nucleon isoscalar form factor:

$$G_{IS}^2(Q^2) = A(Q^2)/(C_E^2(Q^2) + C_Q^2(Q^2))$$

- choosing a parametrization for  $G_{E_p}$  and subtracting it from the isoscalar nucleon form factor to get  $G_E^n$ .

First elastic measurements of  $G_E^n$  were performed in 1960's at  $Q^2 < 0.2$  (GeV/c)<sup>2</sup> at SLAC [17] and Orsay [18], [19]. In 1971 the elastic data on  $G_E^n$  has been extended to higher  $Q^2$  by a measurement at DESY by Galster *et al.* [16]. In a later work by Simon *et al.* [20] the data were analyzed with the inclusion of the effects from meson exchange currents and isobar configurations.

The most recent measurement of  $G_E^n$  using the above approach was carried out by Platchkov *et al.* for  $Q^2$  up to 0.7 (GeV/c)<sup>2</sup> [21]. The relativistic and MEC effects for the kinematics covered were estimated to be of order of 10%, and were corrected for, with the systematic uncertainty due to this correction of about 5%. These uncertainties resulted in an uncertainty of about 20% for the extracted value of  $G_E^n$ . The results extracted with different  $N - N$  interaction potentials are shown in Figure 3.3(b). The open circles correspond to the Paris potential. For clarity, for the other potentials only the fits to the extracted data points (not data points themselves) are shown. As one can see, the model-dependence of the results is of order of 30 – 40%.

### 3.3 Hybrid analysis of the elastic $e - d$ data

The extraction of  $G_E^n$  as described in the previous section relies on the charge and the quadrupole form factors of the deuteron (after removing a small contribution from the magnetic form factor to the cross section). Recently it has been shown that of the two form factors the quadrupole one has less sensitivity to two-body currents and the choice of the  $N - N$  potential [22]. Schiavilla and Sick have used this fact to extract  $G_E^n$  using the quadrupole form factor  $G_Q$  and the polarized observable  $t_{20}$  (we call their approach a *hybrid* one since it uses both polarized and unpolarized data). In their analysis, they first fit the world data on the  $e - d$  elastic cross-section with flexible parameterizations for the deuteron form factors, and then extract  $G_E^n$  by comparing the theoretical predictions of the quadrupole form factor with the experimental values. The theoretical prediction is the average of five different theoretical calculations performed with different  $N - N$  interaction potentials. For the proton form factors, the Hoehler parametrization [23] is used, and  $G_E^n$  is taken in the Galster [16] form <sup>2</sup>. A deviation of the theoretical prediction from the experimental data is taken as an indication of deviation of the  $G_E^n$  from the adopted parametrization, and the value of  $G_E^n$  is adjusted such that a perfect agreement between the theoretical and the experimental values of  $G_Q$  is reached.

The extracted  $G_E^n$  values are shown in Figure 3.4. The error bars included the spread in theoretical predictions on  $G_Q$ . One can see that Sick and Schiavilla's

---

<sup>2</sup>To be more accurate, they use both Galster and Hoehler parameterizations for  $G_E^n$ . However, in the  $Q^2$  range of interest the two are very close to each other.

data roughly follow the Galster parameterization, although the error bars are fairly large (since the points are correlated, they really represent an error band rather than independent errors).

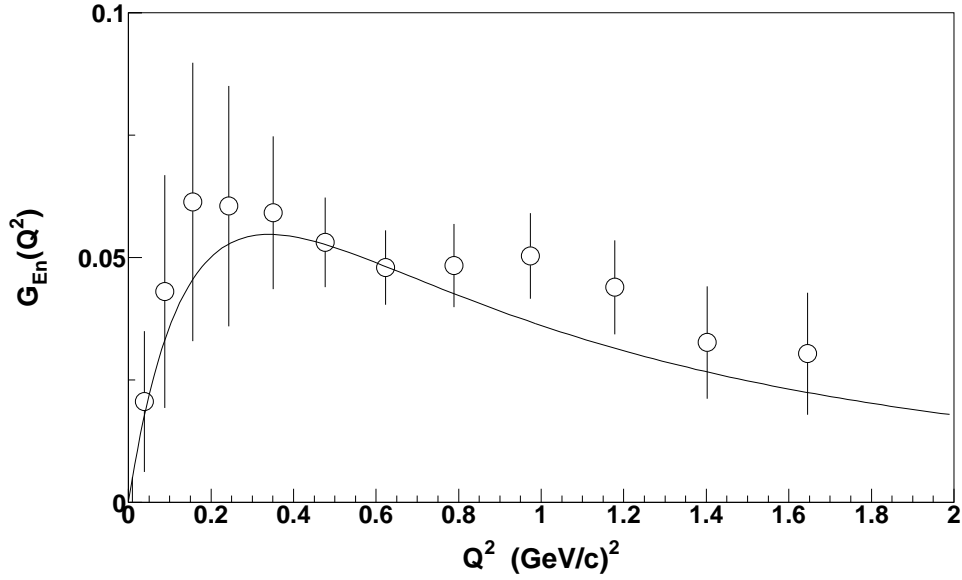


Figure 3.4: Sick and Schiavilla’s extraction of  $G^n$ . The solid line is the standard Galster parametrization.

### 3.4 Polarized measurements

To use spin degrees of freedom for determination of  $G_E^n$  was first suggested by Dombey [24] in late 1960’s. The idea is that various polarization observables (especially beam-target asymmetry and the recoil polarization) in  $e - d$  scattering are sensitive to  $G_E^n$ . For instance, in plane wave impulse approximation (PWIA) the

polarization transfer to the recoil nucleon is given by:

$$P_{eN}^x = -P_B \cdot \frac{\sqrt{2\tau\epsilon(1-\epsilon)}}{\epsilon G_E^2 + \tau G_M^2} \cdot G_E G_M \quad (3.6)$$

$$P_{eN}^y = 0 \quad (3.7)$$

$$P_{eN}^z = P_B \cdot \frac{\tau\sqrt{1-\epsilon^2}}{\epsilon G_E^2 + \tau G_M^2} G_M^2, \quad (3.8)$$

where  $P_B$  is the beam polarization. A similar set of equations can be written down for the components of the spin-correlation vector in scattering from a polarized nucleon<sup>3</sup>. However, it should be mentioned that the formalism of polarization transfer and polarized target scattering is only identical in one-photon approximation. Two photon exchange contributions may in general affect the results of the two methods differently.

Polarized experiments offer several important advantages over traditional cross-section-based measurements, including reduced susceptibility to experimental systematic errors (like neutron detector efficiencies, etc.) and lower sensitivity to two-body currents. Since polarized scattering experiments require high intensity polarized beams in combination with either a polarized target or a recoil polarimeter, the first such experiments did not occur until early 1990's, when technological advances made them possible.

The first recoil polarization measurement of  $G_E^n$  was performed in early 1990's at MIT-Bates [25] with a neutron polarimeter calibrated at Indiana University Cy-

---

<sup>3</sup>Scattering from a polarized deuterium target will be considered in detail in Section 4.

clotron Facility. Despite low statistical accuracy (due to low 0.8% duty factor of the accelerator) that experiment was an important demonstration of feasibility of the method. Another measurement with this technique was performed at MAMI at  $Q^2 = 0.15$  and  $Q^2 = 0.34$  [26]. The most recent polarization transfer  $G_E^n$  experiment was conducted at the Jefferson Lab at  $Q^2$  up to 1.45 [27]. These data provide the most accurate high- $Q^2$  data on  $G_E^n$  to date.

Early  $G_E^n$  experiments employing the beam-target asymmetry were performed with the polarized  ${}^3\text{He}$  target. In a  ${}^3\text{He}$  nucleus, about 86% of the nuclear polarization is carried by a neutron, and therefore it can be used as an effective neutron target, as originally suggested by Blankleider and Woloshyn [28]. From the experimental point of view,  ${}^3\text{He}$  is very convenient (high luminosity and small dilution afford a very good figure-of-merit). On the other hand, since a  ${}^3\text{He}$  nucleus is more complicated than a deuteron, unfolding nuclear effects becomes a more difficult task.

The analysis of the first measurements with the  ${}^3\text{He}$  polarized target neglected final state interactions and thus resulted in  $G_E^n$  values significantly lower than other polarized data [29],[30]. A later reanalysis of the data of [30] in [31] with inclusion of the FSI has brought this data point into a better agreement with the results obtained with other measurements. Another recent reanalysis of PWIA results from [32] performed by Bermuth *et al.* [33] has also somewhat improved the agreement with the phenomenological Galster parametrization which is roughly followed by other experimental points at this region.

Since the polarized deuteron target is used in the experiment presented in this dissertation, we shall devote the next chapter to explore this method in detail. Only two measurements have been taken with this method in the past, one of them being the 1998 run of the present experiment [34], which yielded an accurate measurement of  $G_E^n$  at this kinematics ( $Q^2 = 0.5$ ) at that time. In an earlier experiment at NIKHEF [35] the technique was successfully tested for the first time at  $Q^2 = 0.21$ .

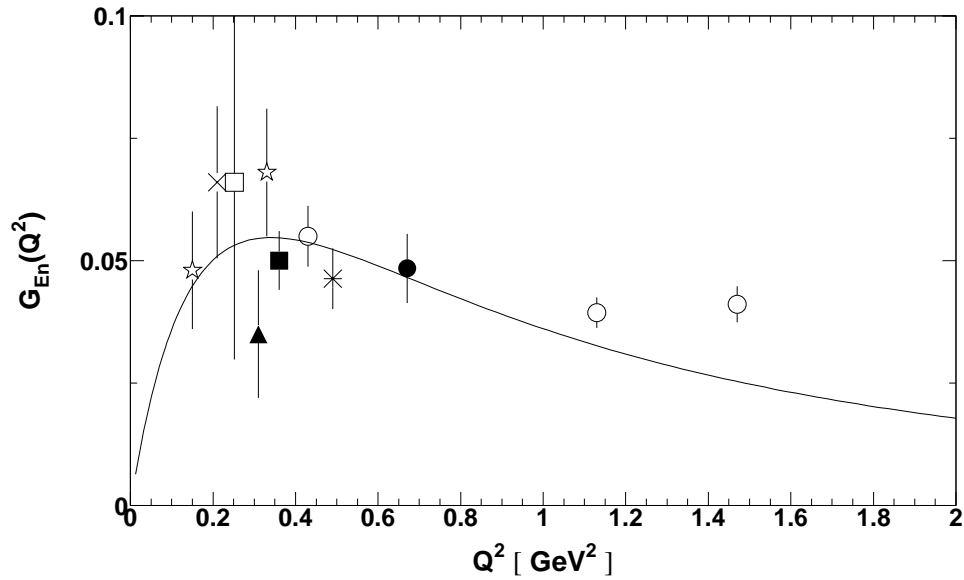


Figure 3.5: Polarized measurements of  $G_E^n$ . Recoil polarimetry data: open circles [27], open square [25] and open stars [26]. Polarized  $^3\text{He}$  data: filled square [31], filled circle [33] and filled triangle [29]. Polarized  $d$  target: cross-hair [35] and asterisk [34]. The solid line is the standard Galster parametrization.

# Chapter 4

## Experimental technique

### 4.1 Polarized scattering from a free nucleon

In Section 2.1 we have already considered the case of unpolarized electron-nucleon scattering. In the polarized case the Rosenbluth cross-section (2.10) is modified to:

$$\left(\frac{d\sigma}{d\Omega}\right)^{pol} = \left(\frac{d\sigma}{d\Omega}\right)^{unpol} (1 + h\vec{A}_{eN} \cdot \vec{P}_T), \quad (4.1)$$

where  $h$  is the beam helicity,  $\vec{P}_T$  is the target polarization,  $\vec{A}_{eN}$  is the beam-target asymmetry with components

$$A_{eN}^x = -\frac{2\sqrt{2}M\rho'_{LT}G_E G_M}{\rho_L(G_E)^2 + \rho_T(G_M)^2} \quad (4.2)$$

$$A_{eN}^y = 0 \quad (4.3)$$

$$A_{eN}^z = -\frac{\rho'_T(G_M)^2}{\rho_L(G_E)^2 + \rho_T(G_M)^2}, \quad (4.4)$$

and  $\rho_\alpha, \rho'_\alpha$  ( $\alpha = L, T, LT$ ) are elements of the virtual photon density matrix which only depend on the kinematics and the target polarization angles  $\theta^*, \phi^*$  (see Figure 4.1). As first pointed by Dombey [24], the sensitivity of the asymmetry (4.2)-(4.4) to the electric form factor can be used for experimental determination of  $G_E^n$ . This sensitivity is maximized for the case of in-plane target polarization perpendicular to the momentum transfer, i.e.  $\phi^* = 0$  and  $\theta^* = \pi/2$ . The beam-target asymmetry then simplifies to:

$$A_{en}^V = \frac{-2\sqrt{\tau(1+\tau)} \tan(\theta_e/2) G_E G_M}{(G_E)^2 + \tau[1 + 2(1+\tau) \tan^2(\theta_e/2)](G_M)^2}. \quad (4.5)$$

On the other hand, from the definition (4.1) the asymmetry can be expressed in terms of cross-sections for different helicities,  $\sigma_+$  (for  $h = +1$ ) and  $\sigma_-$  (for  $h = -1$ ):

$$A_{en}^V = \frac{1}{P_B P_T} \frac{\sigma_+ - \sigma_-}{\sigma_+ + \sigma_-}, \quad (4.6)$$

where we added beam polarization  $P_B$  to the denominator to account for possibility of  $P_B < 100\%$ . In the experiment, the cross-sections  $\sigma_{+,-}$  are proportional to detector yields  $N_{+,-}$ , with proportionality factors that carry little or no helicity dependence, i.e.

$$A_{en}^V = \frac{1}{P_B P_T} \frac{N_+ - N_-}{N_+ + N_-}. \quad (4.7)$$

Equations 4.5 and 4.7 contain all information necessary for experimental determination of  $G_E^n$  by scattering polarized electron beam off a free polarized nucleon target.

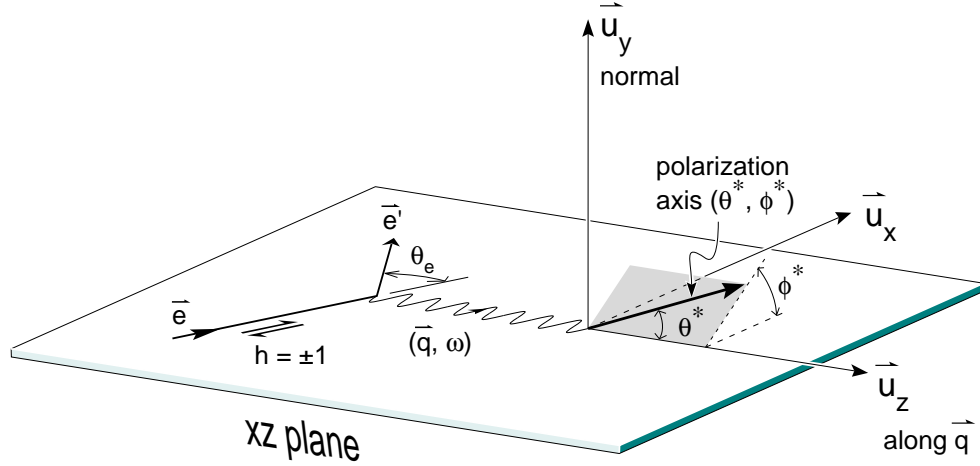


Figure 4.1: Polarized electron-nucleon scattering.

## 4.2 Deuteron target

The formalism of the previous section is self-sufficient in case of a proton. For the neutron, however, the problem is the lack of a free neutron target (unbound neutron decays into a proton, an electron and an anti-neutrino with the lifetime of about 15 minutes). The best surrogate for the neutron target is the deuteron.

In the impulse approximation (i.e. neglecting interactions between the nucleons), the electron-deuteron scattering asymmetry  $A_{ed}^V$  is equal to that of a free neutron,  $A_{en}^V$  (up to a correction factor  $\gamma$  due to the  $D$ -state admixture). However, the relationship of the spin-dependent scattering cross-section to the asymmetry becomes more complicated, since deuteron possesses tensor asymmetry [36]:

$$\left(\frac{d\sigma}{d\Omega}\right)^{pol} = \left(\frac{d\sigma}{d\Omega}\right)^{unpol} [1 + hA_e + P^V A_d^V + P^T A_d^T + h(P^V A_{ed}^V + P^T A_{ed}^T)], \quad (4.8)$$

where  $P_{V(T)}$  is the vector (tensor) polarization,  $A_e$  is the single-spin beam asymme-

try,  $A_d^T$  is the single-spin tensor target asymmetry, and  $A_{ed}^T$  is the tensor beam-target asymmetry. Fortunately, in the experiment, the events are normally sampled symmetrically in the azimuthal angle, and for this case the contributions from  $A_e$ ,  $A_d^V$  and  $A_{ed}^T$  vanish. The remaining  $A_d^T$  term is suppressed by low tensor polarization of the deuteron.

Since the deuteron is a weakly bound system, the impulse approximation is a reasonable first guess. However, for a precise measurement of  $G_E^n$  one needs to take into account reaction mechanisms listed below.

**Meson exchange currents (MEC)** are due to the fact that the nucleons in the deuteron are interacting by meson exchange. Thus, apart from the quasifree scattering amplitude, there will be contributions from direct coupling to the electromagnetic current of the exchanged meson. A few basic MEC diagrams are given on the Fig.4.2.

**Isobar currents (IC)** arise from intermediate excitation of nucleon resonances and from the resonance component of the deuteron wavefunction. Unlike the free case, the scattering from a resonant state cannot be discriminated versus scattering from the ground-state configuration since the pion, emitted in the resonance decay may be reabsorbed by the other nucleon.

**Final state interactions (FSI)** may be important since the final state is a system of two interacting nucleons rather than two plane waves. To the leading order FSI

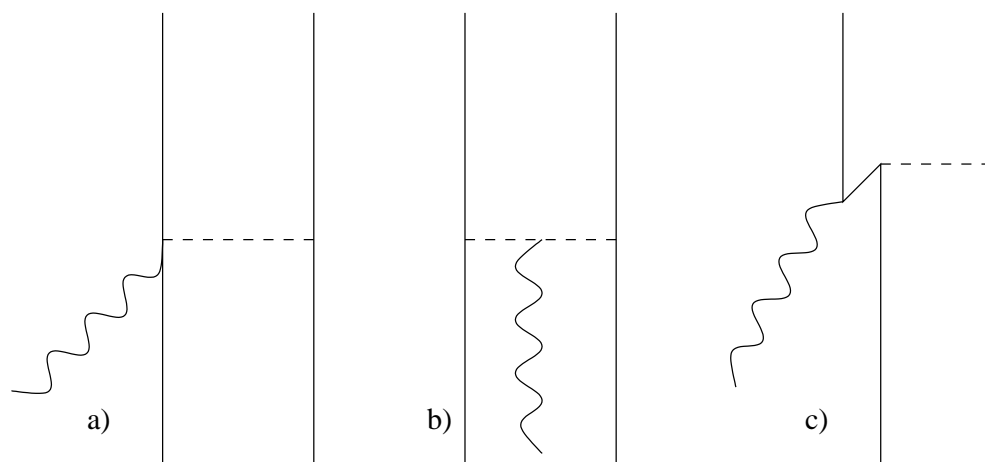


Figure 4.2: Meson exchange currents: a) contact diagram, b) pion-in-flight diagram, c) pair diagram.

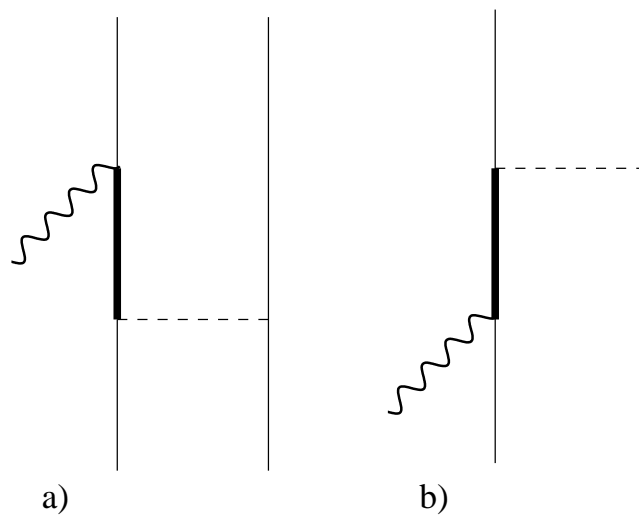


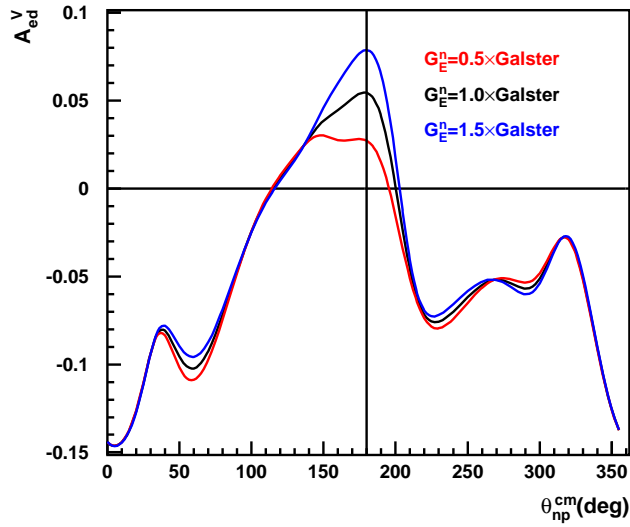
Figure 4.3: Isobar currents: a) coupling to the resonance component of the deuteron wavefunction, b) excitation of the struck nucleon to an intermediate resonance state.

can be considered as rescattering of the struck nucleon by the residual nucleus (or nucleon, in case of the deuteron).

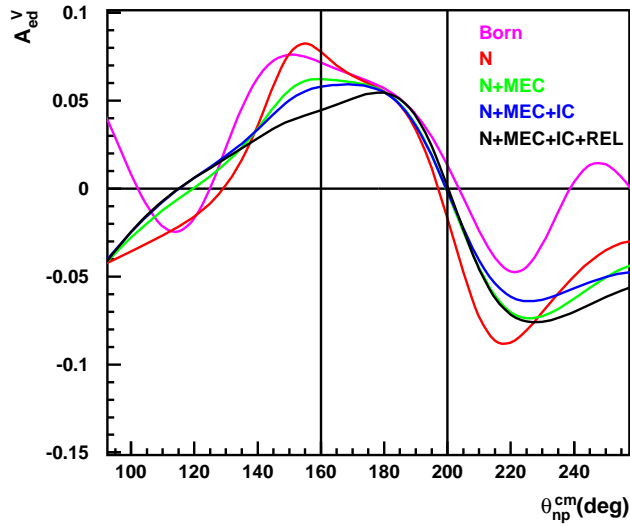
For this experiment relativistic calculations including all these contributions were performed by H. Arenhövel [37] following formalism developed by him and other collaborators in [36], [38], [39]. The calculations were carried out over a kinematic grid representing our experimental acceptance (see Section 6.5.2) for six different models: PWBA, N + MEC, N + MEC + IC, N + REL, PWBA + REL, N + MEC + IC + REL, where PWBA means plane wave Born (or impulse) approximation, N = PWBA + FSI, and REL means “relativistic effects”.

In Figure 4.4 one can see the sensitivity of the  $A_{ed}^V$  to the charge form factor of the neutron (a) and interaction effects and relativistic corrections (b). The asymmetry is plotted versus the angle between the  $n - p$  relative momentum and the momentum transfer  $\vec{q}$  in the deuteron center-of-mass frame,  $\theta_{np}^{cm}$ . The case of  $\theta_{np}^{cm} = 180^\circ$  corresponds to the quasifree kinematics, i.e. the struck neutron emitted along the direction of the momentum transfer. The vertical lines in the Figure 4.4(b) roughly correspond to the experimental acceptance.

As one can see, at the quasifree kinematics the vector beam-target asymmetry is both sensitive to  $G_E^n$  and insensitive to many-body currents and relativistic effects, which makes it ideal for measuring  $G_E^n$ . In order to account for the variation of  $A_{ed}^V$  within the kinematical acceptance, it is necessary to perform acceptance averaging of the theoretical calculations using Monte Carlo simulations (see Section 6.5).



(a) Sensitivity to the value of the neutron form factor.



(b) Sensitivity to nuclear and relativistic effects .

Figure 4.4: The vector beam-target asymmetry  $A_{ed}^V$  versus  $n - p$  breakup angle in the deuteron center-of-mass system  $\theta_{np}^{cm}$ . The case  $\theta_{np}^{cm} = 180^\circ$  corresponds to the quasifree kinematics.

# Chapter 5

## Experimental setup

The experimental setup of the 2001 run of E93-026 was very similar to that of the 1998 run, described in references [40] and [41]. The key elements of the setup were the same: the High Momentum Spectrometer of Hall C, the UVa polarized target, the custom built neutron detector and data acquisition (DAQ) electronics.

Important hardware changes since 1998 included:

- redesign of the neutron detector (added new scintillators, changed the layout, added vertical sticks for position calibration)
- minor upgrades of the target
- removal of the chicane magnet  $BZ_2$  that was causing high background in 1998
- DAQ system was reconfigured to take data in an open-trigger mode.

In the remainder of this chapter we will briefly review the main ingredients of the experimental apparatus.

## 5.1 Polarized electron beam

In this section we will describe the elements responsible for producing, accelerating and steering the polarized electron beam as well as basic devices used for measuring its properties.

### 5.1.1 Accelerator

The Jefferson Lab accelerator was designed to provide a highly polarized continuous wave electron beam to three experimental halls simultaneously. Polarized electrons are produced by photo-emission from a strained gallium arsenide cathode. To ensure simultaneous delivery of the beam to the three physics halls, the photo-cathode is illuminated by three separate laser systems. The electrons emitted by the three lasers operating at 499 MHz pulse frequency are combined in a 1497 MHz beam, from which beams to individual halls are extracted after acceleration.

The initial acceleration to 45 MeV takes place in the injector area. The orientation of the electron spin in the injector (“injection angle”) determines the degree of longitudinality of the electron polarization after spin precession in magnetic elements of arcs and beamlines of the experimental halls. For each configuration of polarization and energy in the three halls the injection angle needs to be calculated separately [42].

From the injector the beam is delivered to the north linac, where it is accel-

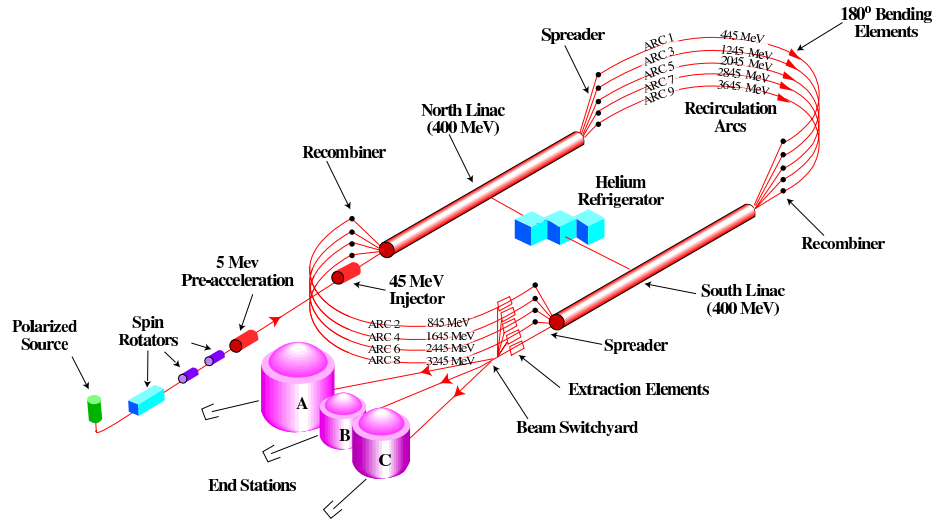


Figure 5.1: Schematic view of the JLab accelerator (Figure by J. Grames).

ated in radio frequency (RF) cavities by 400 MeV<sup>1</sup>. Then the beam goes through the east recirculation arc to the south linac to be further accelerated by 400 MeV. Finally, the beam reaches the switchyard, where it can be either extracted to any of the three experimental halls or steered through the west arc for another pass of acceleration (up to five passes in total).

The helicity of the beam was pseudo-randomly flipped with the frequency of 30 Hz. The beam current asymmetry (BCA) was minimized with the use of an asymmetry feedback system. The BCA was typically below 1000 ppm. Other basic properties of the CEBAF beam delivered to the E93-026 are listed in Table 5.1.

<sup>1</sup>This is the nominal value. For E93-026 the linac gain was set to 569 MeV.

Table 5.1: Basic beam properties (for E93-026)

energy	3481 MeV
relative energy spread	$< 10^{-4}$
current	100 nA
polarization	75%
repetition rate	499 MHz/hall
bunch time width	330 fsec
transverse size	100 $\mu m$
emittance	$< 10^{-9}$ m rad

## 5.1.2 Hall C beamline

### Superharps

A superharp (a wire scanner) is a device which provides a beam profile measurement with a high precision ( $\sim 10 \mu m$ ). It consists of a movable frame, two vertical wires and one horizontal wire. The signals from the wires in combination with the position encoder readouts provide sufficient information for determination of the beam profile. Superharps permit the measurement of the beam energy by using the relation between the field integral (calculated using the magnetic field map) and the deflection angle (measured with superharps). The accuracy of this method is  $10^{-4}$  for relative energy measurements and  $10^{-3}$  for absolute ones. Detailed information on Hall C superharps can be found in references [43] and [44].

### Beam position monitors

The beam position and incident angle were determined by a series of beam position monitors (BPMs) located in Hall C arc and beamline. A BPM consists of four antennas rotated by  $45^\circ$  with respect to the vertical direction. When the beam

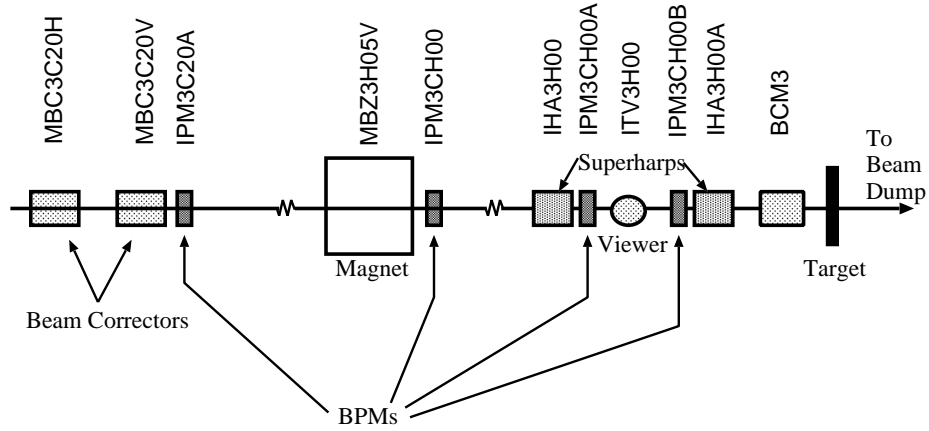


Figure 5.2: Hall C beamline elements [40].

passes through the beamline, each of the antennas picks up the beam’s fundamental frequency. The digitized signals from the antennas are then used to calculate the center of gravity in the BPM coordinates, from which the relative beam position in the beamline is calculated. The absolute position of BPMs was calibrated against survey measurements. Details on BPM operation can be found in [45].

The beam position near the target was determined by a secondary emission monitor (SEM) [41]. SEM readings were also used to calibrate the beam position versus the slow raster current. The SEM and the BPMs provided an accuracy of about 1 mm.

### Beam current monitors

Beam current and total charge passing through the target were measured with the use of beam current monitors (BCMs). Hall C is equipped with two BCMs. The BCMs are RF cavities positioned coaxially with the beamline. The RF cavities serve as cylindrical waveguides whose transverse magnetic mode  $TM_{10}$  is excited by

the beam's fundamental frequency (1497 MHz). The signal is then downconverted in frequency and sent to an rms-DC converter whose output is proportional to the beam current.

During data taking, the performance of BCM1 was unstable, and thus all calculations involving beam charge were based on readings from BCM2. Both BCMs read 10 – 15 nA above zero in the absence of the beam. A software cut on the beam current was used to prevent overestimation of the charge passing through the target due to these zero readings (see Section 6.2 for details). The calibration of BCMs was performed using the injector Faraday cup. The accuracy of the BCMs was estimated to be 5% [46].

### Møller polarimeter

The Hall C Møller polarimeter [47] provided high-precision measurement of the beam polarization. A schematic view of the polarimeter is shown in Figure 5.3.

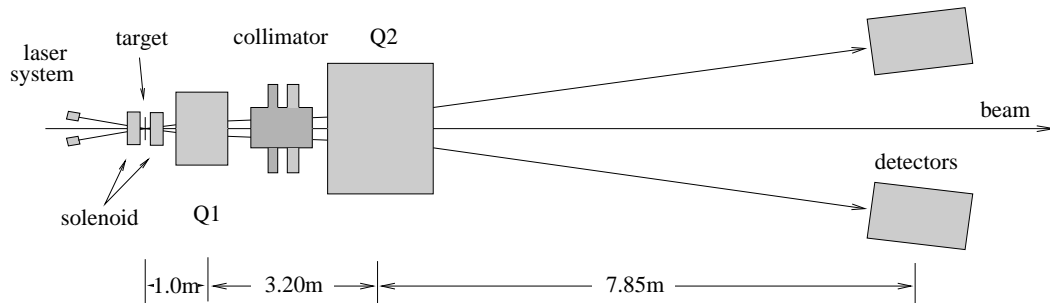


Figure 5.3: Layout of the Hall C Møller polarimeter [47].

The  $10\mu m$  iron target was polarized to 8% with a 4 T superconducting solenoid. A system of movable collimators in combination with a two-quadrupole optical system

was used to suppress Mott background, providing a signal-to-noise ratio of 1000:1. Recoil and scattered electrons were detected in two lead-glass counters. A statistical accuracy of about 1% could be obtained in about 20 minutes of measurement time.

### 5.1.3 Raster magnets

The electron beam was rastered over a 2.2 cm diameter with the Hall C raster system. The purpose of beam rastering was to ensure uniform distribution of target polarization over the target face to improve the accuracy of the NMR measurement. The raster system consists of the slow raster and the fast raster. Each raster subsystem consists of two magnets driving the beam in x and y directions, a power resonance loop and a raster pattern generator. The fast raster smeared the beam over a spot of dimensions of 1 mm  $\times$  1 mm while the slow raster generated a pseudo-spiral pattern with the radius of 1.1 cm (see Figure). The amplitude of slow raster currents was modulated at 0.95 Hz. To minimize induced experimental asymmetries the frequency of the modulation was synchronized with the beam helicity flip. The shape of the amplitude modulation was chosen to approximate the  $A(t) = \sqrt{R_0^2 - \alpha t}$  dependence for which the beam charge deposited at raster radius  $r$  approximately constant (see Figure 5.4). The details of the Hall C raster system can be found in references [40] and [48].

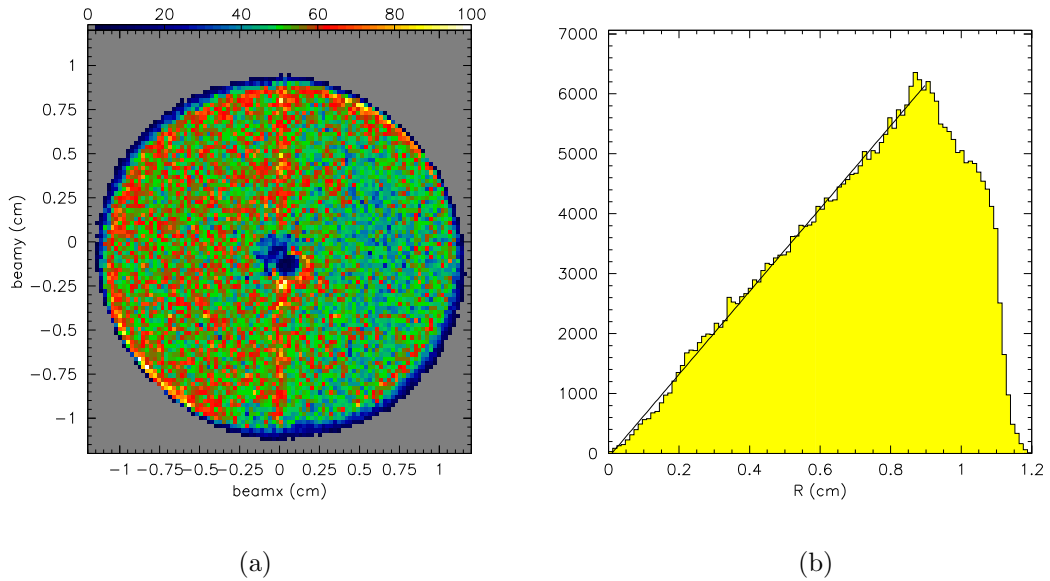


Figure 5.4: Rastered beam: (a) distribution over the target face, (b) radial profile. The straight line fitted to the radial distribution shows that the latter is approximately linear, i.e. the beam charge deposited per unit area is roughly constant.

### 5.1.4 Chicane magnets

The polarized target requires a 5 Tesla magnetic field for its normal operation. This field bends incident electrons down. To ensure normal incidence of the electron beam onto the target surface a system of two chicane magnets was used (see Figure 5.5). A detailed description of the chicane system is given in [49]<sup>2</sup>.

## 5.2 Hall C High Momentum Spectrometer

The High Momentum Spectrometer (HMS) is a standard piece of equipment of TJNAF Hall C. The spectrometer can be rotated about the target, providing a wide

<sup>2</sup>This description includes the BZ2 magnet which was not used in the 2001 run of E93-026.

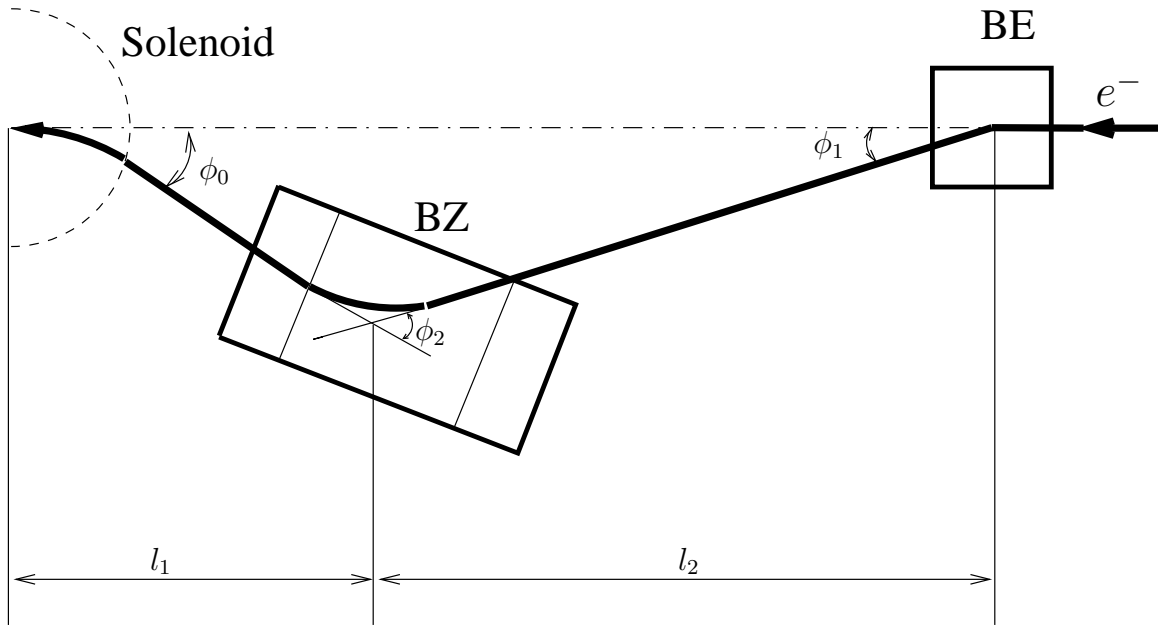
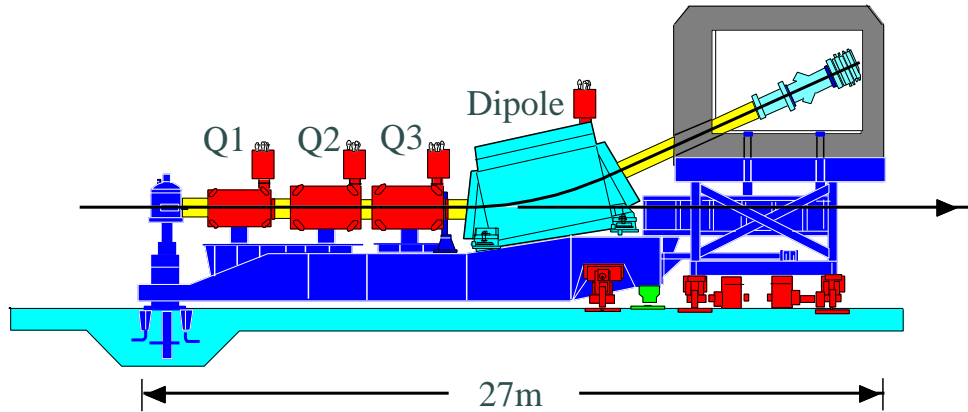


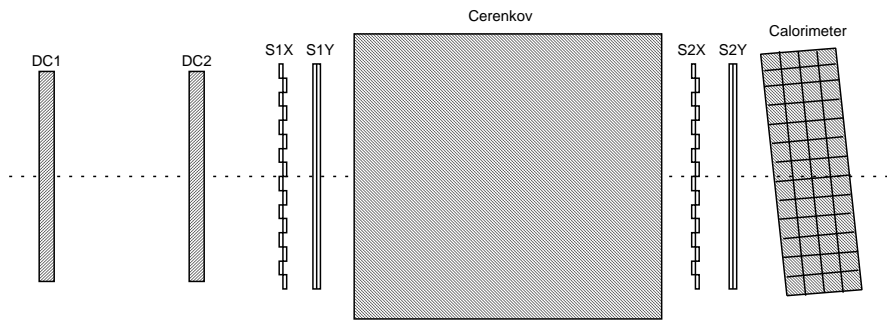
Figure 5.5: Chicane magnets. The dimensions and angles shown on the picture are:  $l_1 = 4.84$  m,  $l_2 = 13.87$  m,  $\phi_0 = 2.3^\circ$ ,  $\phi_1 = 0.8^\circ$ ,  $\phi_2 = 3.1$ .

range of measurable scattering angles. The basic subsystems of the HMS include the collimator system, the magneto-optical system and the detector package located in a shielded hut.

Two different collimators can be installed in the HMS entrance: the octagonal pion collimator was used for normal data taking, while the sieve slit was used for spectrometer optics checkout. Three quadrupole magnets and one dipole magnet comprised the magneto-optical system of the spectrometer. Quadrupole magnets Q1 and Q3 focused rays in the dispersive direction, Q2 focused transverse rays and the dipole magnet provided a vertical bend of  $25^\circ$  into the detector hut. The detector package consisted of two drift chambers for tracking, two sets of x-y hodoscopes for timing and forming the primary trigger, a gas Čerenkov detector and a lead glass



(a)



(b)

Figure 5.6: Hall C High Momentum Spectrometer: (a) – entire spectrometer, (b) – contents of the detector hut. Note that the calorimeter is tilted in order to prevent loss of particles in gaps between the blocks.

shower counter for particle identification. The basic characteristics of the HMS are listed in Table 5.2.

Table 5.2: HMS characteristics.

Maximum central momentum	7.4 GeV/c
Momentum resolution	0.04%
Solid angle acceptance	5.9 msr
Scattering angle resolution	0.8 mrad
Out-of-plane angle resolution	1.0 mrad
Extended target acceptance	15 cm
Vertex reconstruction accuracy	5 mm*

\* Minimum value. In general momentum dependent.

## 5.3 Polarized target

The UVa cryogenic polarized target has been used in SLAC experiments E143, E155 and E155x prior to being used in E93-026 and is documented in references [40], [41], [50], [51]. The target was polarized using the dynamic nuclear polarization (DNP) mechanism (see Appendix A.1). This technique requires the target material ( $^{15}ND_3$ ) to be placed at a low temperature (about 1K) in a strong magnetic field (5 Tesla). To transfer the electron polarization to the nuclei, the material must be additionally radiated by the microwave power. Further, the target polarization must be continuously monitored. The main components of the target system are shown in Figure 5.7.

In the remainder of the section we will describe each of these components.

### 5.3.1 Magnet

The 5 Tesla superconducting magnet was provided by Oxford Instruments. It consisted of two sets of coils, approximately 50 cm in outer diameter and approximately

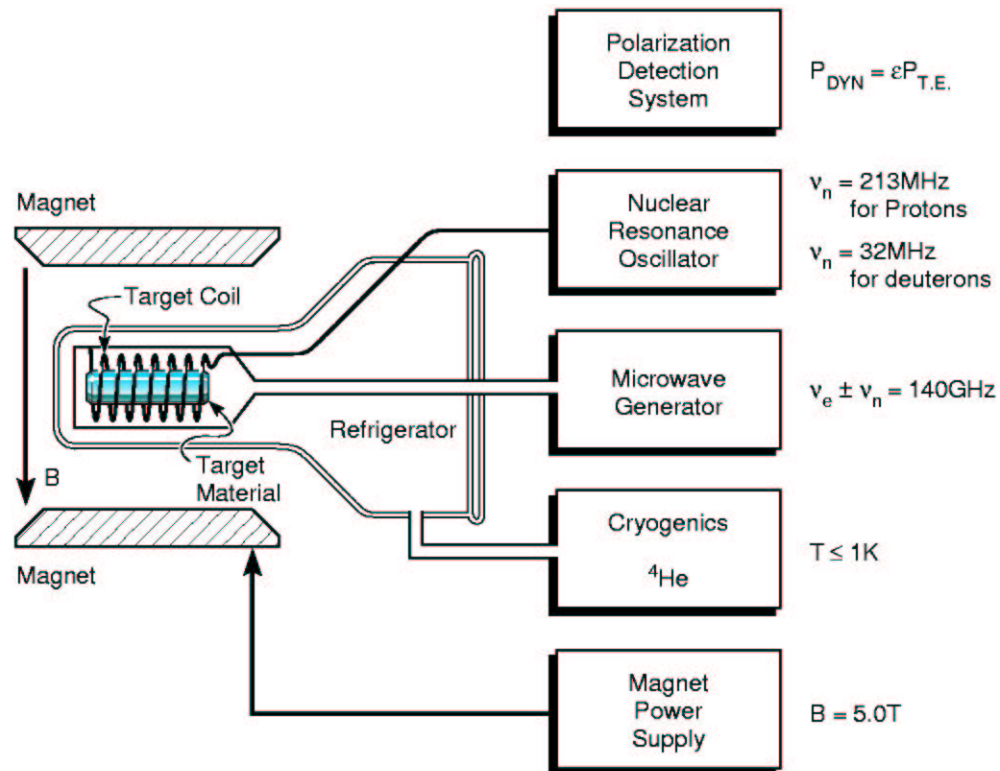


Figure 5.7: Main components of the UVa polarized target.

8 cm apart at the core (Figure 5.8). The shape of magnet was such that its parts did not interfere with the acceptance of the spectrometer and allowed taking data in two orientations, perpendicular and parallel to the magnetic field. The magnet produced a 5 T magnetic field uniform to  $1 \times 10^{-4}$  over the target cell volume and stable to  $1 \times 10^{-6}$  per hour.

### 5.3.2 Refrigerator

The  $^4\text{He}$  evaporation refrigerator was installed vertically along the center of the magnet. Liquid helium for refrigerator operation was supplied from the magnet

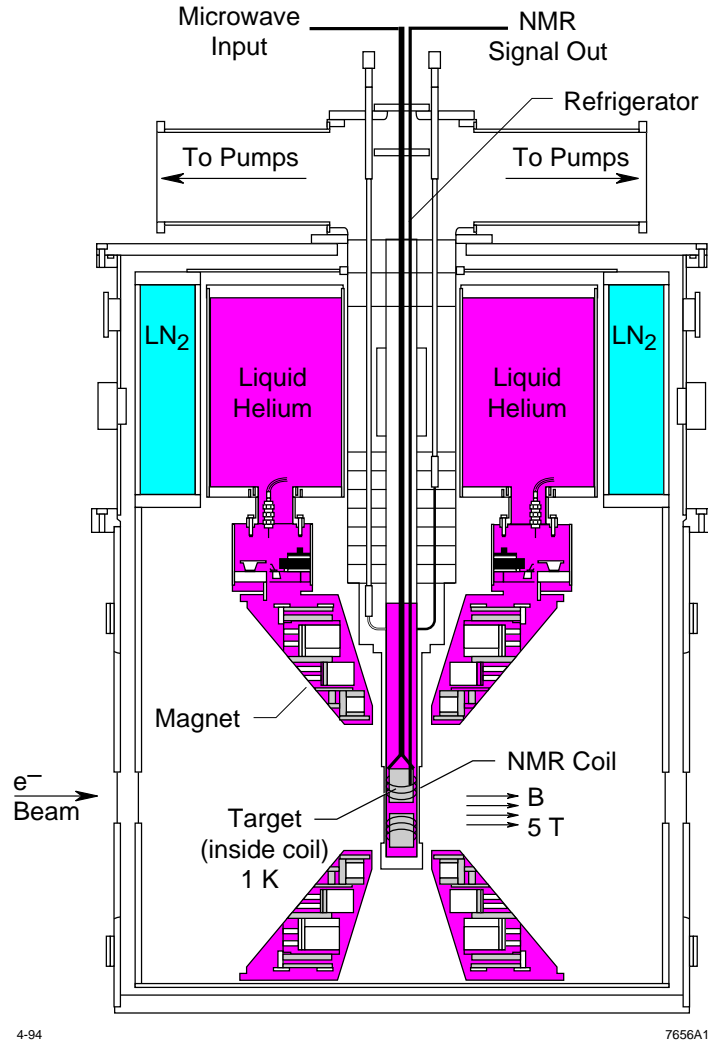


Figure 5.8: Target cryostat and magnet.

dewar through a short transfer line into a separator. The function of the separator was to separate the liquid and the gas phases of helium and feed the liquid into the target chamber either directly or through a system of heat exchangers. Three mechanical pumps removed up to 1.5–2 Watts of heat deposited in target by beam and microwave radiation.

### 5.3.3 Insert

The insert carrying targets cells, microwave guides and horns, NMR instrumentation, anneal heater and temperature sensors was set along the central bore of the target (see Figure 5.9). The targets were two  $^{15}\text{ND}_3$  targets (“top” and “bottom”), carbon, empty cup and two holes, 8 mm and 10 mm in diameter. A stepper motor was used to move the insert in the vertical direction so that any target could be placed in the beam path. Having two  $^{15}\text{ND}_3$  targets in the same insert reduced experiment downtime due to restoration of material polarization properties after beam radiation damage (“target anneal”). The hole targets were used for target alignment. Data taken with empty and carbon targets was used to calibrate inclusive simulations (see Section 6.4).

### 5.3.4 Microwaves

The microwave system provided photons driving the polarization-enhancing transitions. The microwave power was generated by an Extended Interaction Oscillator (EIO) tube at frequencies around the electron spin resonance frequency (140 GHz) and could be tuned in a range of 2 GHz. The exact choice of the frequency was determined by the desired sign of the polarization of the material. The microwaves were delivered from the generator to the microwave horn in the target insert through a waveguide. A horn switch allowed one to choose which of the two  $\text{ND}_3$  targets to polarize. A change in the helium boil-off was used to estimate that about 1 Watt of



Figure 5.9: Target ladder carrying target cells. The targets are (from top to bottom): top  $^{15}\text{ND}_3$  (the purple spot is due to the radiation damage), 10 mm hole, 8 mm hole (partially obscured by the microwave horn of the bottom  $^{15}\text{ND}_3$  cell), bottom  $^{15}\text{ND}_3$ , carbon and empty.

microwave out of 20 Watts generated reached the target cell.

### 5.3.5 NMR and data acquisition

The target polarization was continuously measured by the NMR technique (see Appendix A.2). The NMR system used two copper-nickel coils, one for the bottom target and one for the top target. The signal from coils was sent through a  $\lambda/2$  cable to the Liverpool  $Q$ -meter. Calibration constants for the NMR signal were provided

by a series of thermal equilibrium (TE) measurements. A target data acquisition computer used Labview interface to display online values of the target polarization as well as other critical parameters of the target system (temperature, helium pressure, microwave frequency and power etc.). The online target polarizations served mostly for data taking guidance (the figure of merit of the experiment dictates a minimum polarization below which targets should be switched or annealed) and for a quick online analysis. The actual target polarization numbers used in calculation of the  $A_{ed}^V$  were obtained in a full offline analysis (see Section 7.3 for details).

### 5.3.6 Target material

As the source of polarized deuterons frozen deuterated ammonia was chosen. This choice was determined by high maximum polarization (up to 40%) and high radiation damage resistance of this material. Additionally,  $^{15}\text{ND}_3$ , than the usual  $^{14}\text{ND}_3$  ammonia, was used, since in  $^{14}\text{N}$  both unpaired nucleon spins contribute to the experimental asymmetries, whereas in  $^{15}\text{N}$  only the proton asymmetry is contaminated and needs a correction. The purities of the target material were 98% for the nitrogen and 99% for the deuterium.

The target material was fabricated by shattering frozen ammonia and sifting the crystals to obtain the fragments of the desired size (1-3 mm). Free paramagnetic radicals needed by dynamic nuclear polarization were introduced by means of irradiation in an electron beam. Of the seven batches of material used during

Table 5.3: Average polarizations and total radiation doses for various targets.

	positive polarization		negative polarization	
	$\langle P_t \rangle, \%$	$Q_{tot}, \text{C}$	$\langle P_t \rangle, \%$	$Q_{tot}, \text{C}$
stick 3 top	+23.7	$2.39 \cdot 10^{-3}$	-21.3	$1.25 \cdot 10^{-2}$
stick 3 bottom	+21.5	$1.73 \cdot 10^{-2}$	-19.3	$1.94 \cdot 10^{-2}$
stick 4 top	+28.7	$9.77 \cdot 10^{-3}$	-24.4	$1.90 \cdot 10^{-2}$
stick 4 bottom	+28.1	$1.60 \cdot 10^{-2}$	-24.2	$1.81 \cdot 10^{-2}$

the experiment, two were obtained by *in situ* cold (1.5 K) irradiation while the remaining five were “tempered” (i.e. let warm until disappearance of the purple color created by irradiation). It was found that the “tempered” loads of the material had higher average polarization. [52].

Average polarization breakup by cell and material load is given in Table 5.3. All four material batches given in the table have been prepared by “tempering”. The overall average was +24.9% for positive polarization and -22.4% for the negative one. An average radiation dose between anneals was about  $200 \times 10^{-14}$  electrons (0.32 mC), which corresponds to about 9 hours of the beam time with the nominal current (100 nA). A typical anneal took about 1 hour and the temperatures were about 100 K. The details on the target material performance and preparation can be found in [52] and [53].

## 5.4 Neutron detector

The neutron detector was assembled from plastic scintillators arranged in vertical planes. The design of the neutron detector was determined by optimizing the figure-

of-merit (FOM) within experimental constraints (number of available scintillators and slots for neutron detector signals). The simulation for optimizing the neutron detector FOM used detector efficiencies calculated by KSUVAX program and vertical distributions generated by the customized version of MCEEP (see Section 6.5). The detector layout as determined from these simulations is shown in Figure 5.10 and described below.

### 5.4.1 Configuration and position

The front two layers consisted of 1 cm thick scintillators (called *paddles*) for tagging charged particles. The bulk of the neutron detector was made up by three kinds of scintillators called *bars* (see Table 5.5(a)). The placement of bars was dictated by considerations of rates. Front planes and top counters tend to have higher rate, therefore they were filled with narrower bars. To improve the detection and identification of protons, the first paddle plane and the first bar plane were extended vertically. In addition to paddles and bars, two plastic scintillators (called *sticks*) were included in the detector between the third and fourth bar planes for calibrating the horizontal position. A detailed description of the neutron detector layout is given in Table 5.5(b).

Each scintillator had a photomultiplier tube (PMT) attached to each end. The scintillator and the PMTs were connected through BC-800 lightguides. The mean of the left and right PMT TDC signals provided the time of the hit while

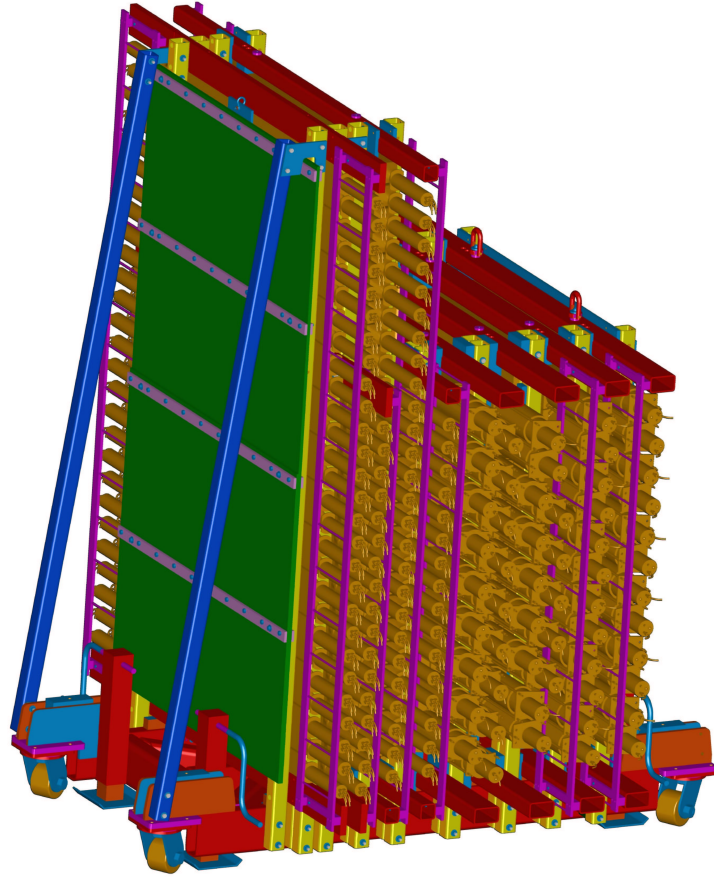


Figure 5.10: The neutron detector.

the difference was used for estimating the horizontal hit position. The two types of PMT tubes used were 2 inch Phillips 2262 (paddles and 10 cm bars) and Hamamatsu R1250 (15 cm bars). The scintillators with the attached PMTs were held by frames mounted on a movable platform. From the direction of target the neutron detector was protected from low-energy background by a lead shielding (with total lead thickness of 25 mm before counters 1-14 in paddle plane 1 and 15 mm before counters 15-27, counting from the bottom). Protection from the background coming from the beamline was provided by concrete walls built around the neutron detector.

Table 5.4: Neutron detector scintillators (a) and their layout (b).

type	material	cross section	length	phototube	qty
paddles	BC-408	11 cm $\times$ 1 cm	160 cm	Phillips 2262	44
10 cm bars	BC-408	10 cm $\times$ 10 cm	160 cm	Phillips 2262	48
15 cm bars	BC-408	trapezoid*	160 cm	Hamamatsu R1250	28
20 cm bars	BC-408	trapezoid**	160 cm	Hamamatsu R1250	28
sticks	BC-408	2 cm $\times$ 2 cm	200 cm	Phillips 2262	2

\*Top width 12 cm, bottom width 15.4 cm, height 15 cm.

\*\*Top width 7.2 cm, bottom width 11.4 cm, height 20 cm.

plane	type of counters	# of counters	packing*	height
1	paddles	27	0.5 cm overlap	61.2 cm
2	paddles	17	0.5 cm overlap	61.2 cm
3	10 cm bars	26	0.6 cm	66.7 cm
4	10 cm bars	16	0.6 cm	67.7 cm
5	20 cm bars	18	0.6 cm	65.7 cm
6	10 cm & 15 cm bars	10+4	0.6 cm**	73.8 cm
7	15 cm bars	12	0.6 cm	66.6 cm
8	15 cm bars	12	0.6 cm	66.6 cm

\* Vertical distance between adjacent counters.

\*\* 1.6 cm between the 15 cm and 20 cm bars.

The neutron detector was positioned so that the momentum transfer vector pointed approximately into its center. That allowed to emphasize quasielastic events and improve the dilution factor. The front plane of the detector was placed at the distance of 595 cm from the target to allow a comfortable time-of-flight separation of 8 nanoseconds between gammas from delta electroproduction and nucleons.

### 5.4.2 Gain monitoring

It is possible for the gains of the PMTs to change during the experiment. They may drift over a long period of time or they may sag due to high rates in the detector. It is therefore desirable to monitor gains of PMTs. The experiment E93-026 used a laser pulser for that purpose.

The nitrogen laser was located in a specially designated room in the counting house. The 337 nm UV light generated by the laser was transformed by the scintillator radiator into visible blue light ( $\lambda \sim 400 \text{ nm}$ ). This light was transported by an 80 m long 1 mm diameter silica fiber to the primary distribution box in the experimental hall, where the signal was split 1:25. Outputs from this box were connected to a 1:64 splitter via a 10 m long 1 mm diameter silica fiber. Outputs from the splitter were then sent to both ends of the bars. The light output was monitored by a PIN diode.

By comparing the ADC of the laser signal to its known intensity ( $300 \mu\text{J}$  per pulse) it is possible to monitor photomultiplier gains and perform energy calibrations of the neutron detector.

The laser pulser logic for E93-026 is described in the next section. The details on the design and implementation of the Hall C gain monitoring system can be found in [54].

### 5.4.3 Gain matching

The gains of bar PMTs were matched using cosmic data. A cosmic trigger was defined as (OR of top detectors) AND (OR of bottom detectors). Additionally, in the offline analysis the vertical acceptance was restricted by requiring hits in four consecutive bars. The gain matching procedure consisted of taking cosmic data at three different high voltage (HV) settings for each PMT and then fitting the cosmic peak versus HV. The new HV was chosen such that the cosmic peak was observed in ADC channel  $1100 \pm 100$ .

The paddles were gain matched using the beam. The bottom part of the detector was calibrated with the target field turned off because otherwise it does not have enough statistics. The proton peak was placed in ADC channel  $1200 \pm 100$ . The details of the gain matching procedure can be found in [55].

The thresholds were set to 45 mV for bars and 60 mV for paddles. These values were obtained by examination of ADC spectra (they were chosen so that the low energy background did not exceed the height of the proton peak).

## 5.5 Electronics and data acquisition

In this section we will consider the data acquisition system of the experiment. We will start by overviewing the electronics for various components of the experimental setup. Then we will describe how the signals from these components are combined

together to form triggers. The section will be concluded with a brief description of the event building procedure.

### **5.5.1 Electronics**

#### **HMS electronics**

The HMS logic was a standard one (see [56] for a detailed description). The electron trigger was fired by hodoscopes (a hit in 3 of 4 planes was required for that). There was no hardware pion rejection. The standard software cut required three or more Čerenkov photoelectrons. The signal from the shower counter was not used.

#### **Neutron detector electronics**

The neutron detector electronics setup is shown in Figure 5.12. The PMT signals were amplified by  $\times 10$  Phillips 776 amplifiers. The amplifiers are 16 channel units with individual offset adjustments and two outputs. The offsets were set to a negative value of 1-3 mV. It has been experimentally confirmed that inclusion of these amplifiers did not degrade the timing resolution.

The linear signals from the amplifiers were sent to the counting house electronics room where they were split 2/3 and 1/3. The 1/3 signal was sent to ADCs through a delay unit while the 2/3 signal was fed to LeCroy leading edge discriminators. One of the two outputs of the discriminator went to a custom built logic delay unit and then further to scalers and TDCs. The other output of the discrim-

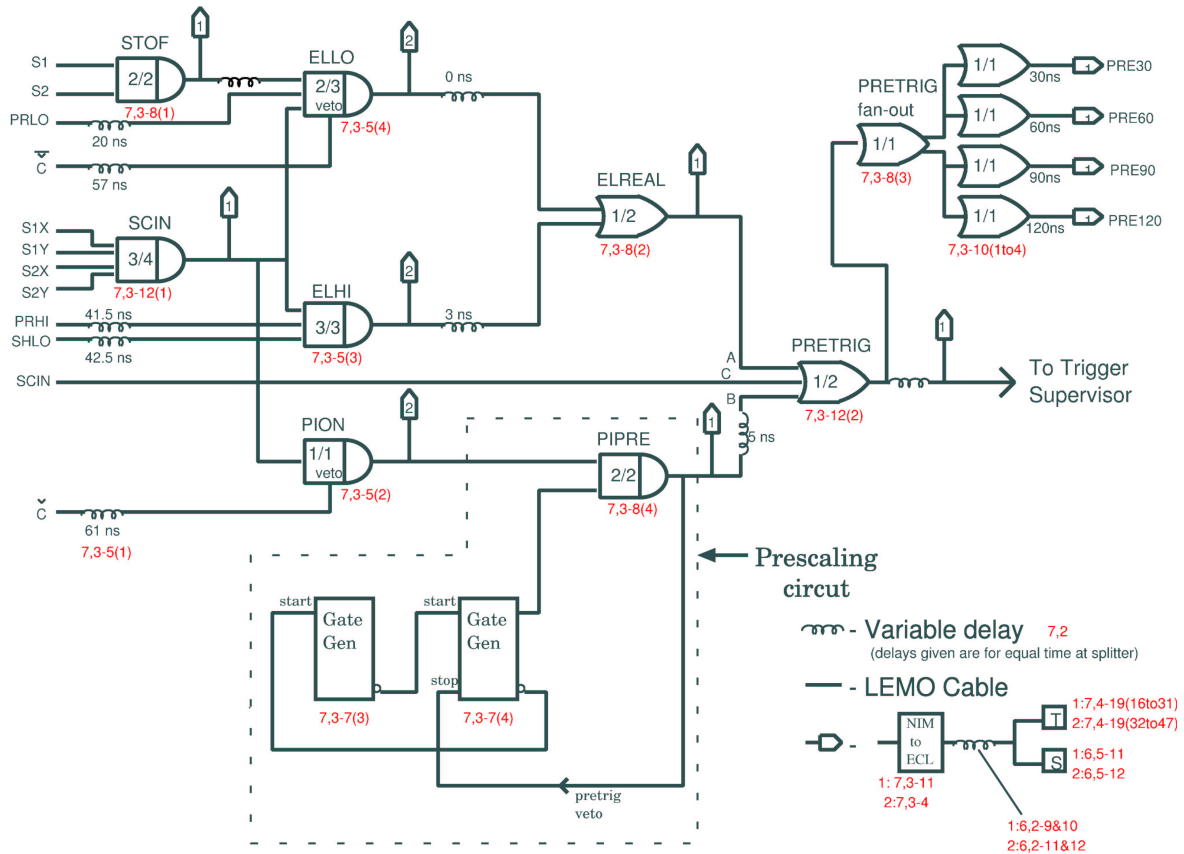


Figure 5.11: HMS trigger electronics. SCIN and STOF are elementary electron triggers formed by hodoscope signals. ELLO, ELHI and ELREAL are advanced electron triggers formed from SCIN, STOF, pion rejection and calorimeter signals. In E93-026 only SCIN electron trigger was used.

inator was sent to a LeCroy 4516 logic unit where coincidence between PMT pairs was formed. The OR output of the LeCroy 4516 module was fired whenever there was a coincidence in one (or more) out of 16 pairs of PMTs. The signal from the OR output supplied as input to a JLab custom built coincidence module to form a coincidence with the HMS PRETRIG (see the next section for data acquisition and

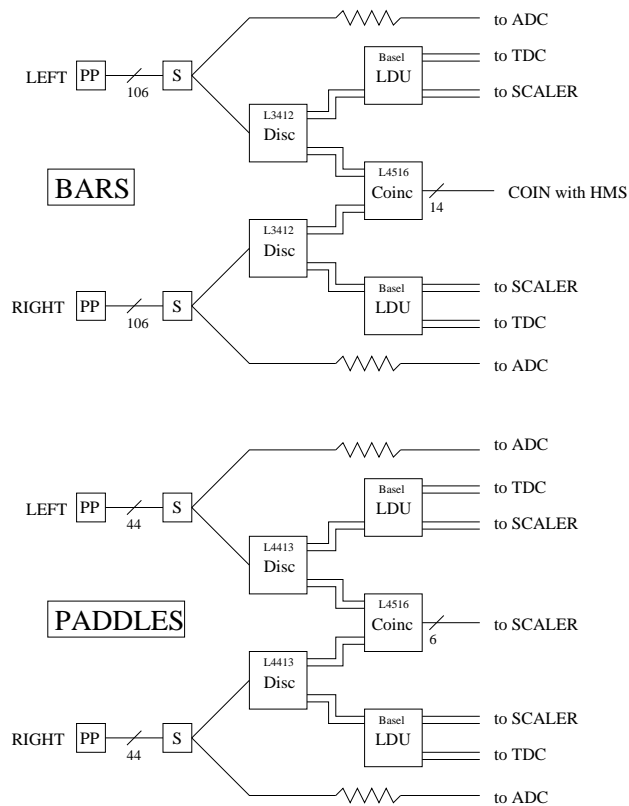


Figure 5.12: Neutron detector electronics. “PP” means “Patch Panel”, “S” stands for “splitter”. Multiple identical elements on the drawing are denoted with a tilted bar with a number of elements below.

trigger details).

The cosmics triggers were formed by signals from the top and bottom detectors of each plane. The signals were OR’d separately for top and bottom detectors. A Level 1 cosmics trigger was formed by an OR between these two signals, while an AND resulted in a Level 2 cosmics trigger.

## Laser electronics

The laser trigger was formed by a coincidence between a photo diode and a photo-tube (see Figure 5.13).

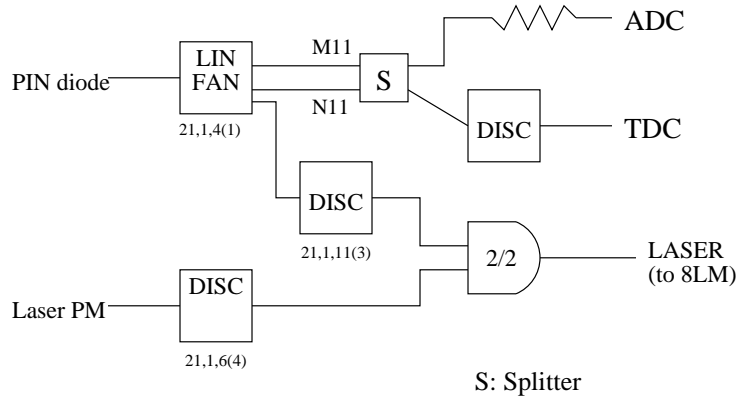


Figure 5.13: Laser trigger

## Scalers

There were three different scaler types used in this experiment: asynchronous scaler, helicity scaler and event scaler.

Asynchronous scalers were mostly used for counting single rates of the detectors. They were read out every two seconds and were not synchronized to the helicity flip frequency (thus the name *asynchronous*). The singles rates from the scalers were displayed online using the scaler server and a Tcl graphic user interface (GUI), which allowed one to detect phototube problems in a timely manner.

There were three helicity gated scalers: h+ for positive helicity, h- for negative helicity and hboth for both helicity states (for consistency check). These scalers

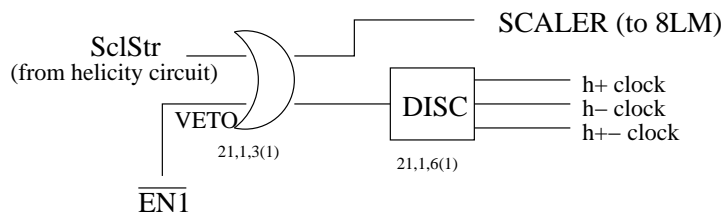


Figure 5.14: Helicity scaler electronics. ScIStr is the scaler clock signal issued by the helicity circuit during the PHT.

were generated during each period of helicity transition (PHT) by a signal from the helicity electronics. Helicity gated scalers kept track of charge and dead time separately for the two different helicity states for a proper normalization of the event counts.

The event by event scaler was read out each event (except for scaler events) and counted only clock and charge.

### 5.5.2 Triggers and events

In the 2001 run of E93-026 the data was taken in an open trigger mode. The neutron detector signals were read out and digitized for each HMS trigger, and all coincidences were made in software. Hardware coincidence electronics only served as a backup in case of failure of the data acquisition system to run in a buffered mode (which was necessary for open-trigger running). Since the buffered mode running was successful, the hardware coincidence triggers were never used during the experiment.

For a typical beam current of 100 nA the HMS pretrigger rate was about 400 Hz

with a computer dead-time of 4.5 %. The electronics dead-time was negligible (see Subsection 7.7.3).

### Trigger logic

Pretriggers<sup>3</sup> and triggers were formed by two Octal Logic Matrix elements (see Figure 5.15) based on signals from experimental subsystems (HMS and neutron detector electronics) and DAQ signals generated by the Trigger Supervisor (TS). The DAQ signals are GO (indicates active DAQ system), EN1 (physics triggers enabled after taking pedestals) and BUSY (DAQ is processing a trigger and is not open to any other triggers).

In addition to the two physics triggers used in this experiment (hms and cos-mics), there was a number of auxiliary triggers generated by DAQ, e.g. pedestal triggers generated in the beginning of each runs to determine ADC pedestals.<sup>4</sup>

A pretrigger was fired by a signal from electronics of the relevant subsystem if the following conditions were fulfilled:

1. DAQ was active (GO signal high)
2. pedestals have already been taken (EN1 signal high)<sup>5</sup>
3. helicity transition is not occurring (PHT signal low).

---

<sup>3</sup>The difference between pretriggers and triggers is due to the busy status of DAQ only. A pretrigger makes a trigger if the BUSY signal is not present

<sup>4</sup>Other trigger types, such as laser, sos, coin (coincidence between SOS and HMS) or e\*B (coincidence between HMS and the neutron detector) were not used in the experiment and will not be discussed here.

<sup>5</sup>For a pedestal pretrigger the case must be exactly the opposite, i.e. EN1 has to be low.

Table 5.5: Outputs of 8LM #1 and #2.

8LM #1 output	Signal	Logic
Q0	HMS-pretrigger	$HMS \& EN1 \& GO \& (!PHT)$
Q1	SOS-pretrigger	$SOS \& EN1 \& GO \& (!PHT)$
Q2	COIN-pretrigger	$HMS \& SOS \& EN1 \& GO \& (!PHT)$
Q3	PED-pretrigger	$PED \& GO \& (!EN1)$
Q4	HMS-trigger	$HMS \& EN1 \& GO \& (!PHT) \& (!BUSY)$
Q5	SOS-trigger	$SOS \& EN1 \& GO \& (!PHT) \& (!BUSY)$
Q6	COIN-trigger	$HMS \& SOS \& EN1 \& GO \& (!PHT) \& (!BUSY)$
Q7	PED-trigger	$PED \& GO \& (!EN1) \& (!BUSY)$

8LM output #2	Signal	Logic
Q0	$e \star B$ -pretrigger	$e \star B \& EN1 \& GO \& (!PHT)$
Q1	LASER-pretrigger	$LASER \& EN1 \& GO \& (!PHT)$
Q2	COSMICS-pretrigger	$COSMICS \& EN1 \& GO \& (!PHT)$
Q3	$e \star B$ -trigger	$e \star B \& EN1 \& GO \& (!PHT) \& (!BUSY)$
Q4	LASER-trigger	$LASER \& EN1 \& GO \& (!PHT) \& (!BUSY)$
Q5	COSMICS-trigger	$COSMICS \& EN1 \& GO \& (!PHT) \& (!BUSY)$
Q6	SCALER-trigger	$SCALER \& EN1 \& GO \& (PHT) \&$
Q7	—	—

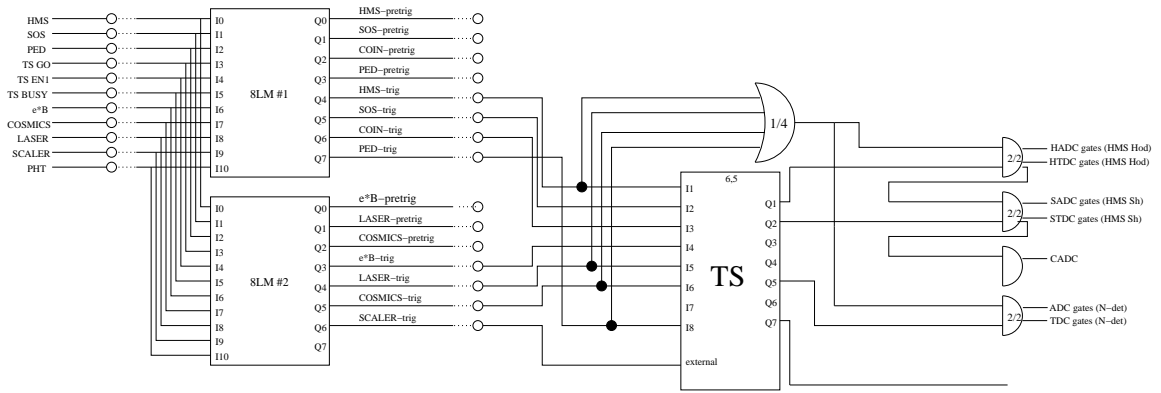


Figure 5.15: Trigger setup.

Forming a trigger required fulfilling the same conditions plus DAQ not being busy processing the previous signal (BUSY signal low).

The outputs of the 8LM modules were fed to the TS. The TS was used to determine the trigger configuration (enabled triggers and prescale factors) depending on the run type (main, cosmics, hms only or scalers). Trigger configurations for this experiment are shown in Table 5.6.

Table 5.6: TS input and configuration. Enabled triggers are indicated with checks.

TS input	Trigger	main	cosmics	hms	scalers
1	HMS	✓	✓	✓	
2	SOS				
3	COIN				
4	$e\star B$	✓			
5	LASER	✓	✓		
6	COSMICS		✓		
7	—				
8	PED	✓	✓	✓	
9-12	—				

## **EPICS**

The important experimental quantities (magnet currents, target polarization etc.) were monitored by the EPICS (for Experimental Physics and Industrial Control Systems) system. The DAQ queried the EPICS database for these values, formed an EPICS event and injected the event into the data stream. This occurred on two time scales depending on expected stability of queried variables: each 2 seconds for “fast” EPICS variables and each 30 seconds for “slow” EPICS variables.

### **Event formation**

The DAQ system was controlled by CODA software [57]. When TS accepted a trigger, it sent a signal to read-out controllers (ROCs) which caused readout of ADCs and TDCs. The ADC and TDC data were collected by ROCs and stored in a buffer, from where they later forwarded to the Event Builder (EB). The EB assembled the event fragments together and synchronized them by checking their numbers. In case of a mismatch an error flag was inserted into the data stream, which allowed the analysis software to skip bad synchronization events (see Section 6.2). Finally, the event was written to a hard drive. A background process copied completed runs to a tape.

# Chapter 6

## Analysis software

This chapter describes software tools used in data analysis. It starts with an overview of the software components and their interaction with each other. The next section contains a description of the data-stream preprocessor (*syncfilter*). Then we give an overview of the event analyzer<sup>1</sup>, focusing mainly on HMS and neutron detector event reconstruction. The chapter is concluded with two sections devoted to inclusive and coincidence simulation packages.

### 6.1 Overview

The interaction of the software analysis tools with each other is shown in Figure 6.1. The CODA data files are analyzed with the event analyzer. In order to remove synchronization errors from the data, the CODA file is piped through the syncfilter. Additionally, syncfilter reports provide dead-time corrected charge for both helicities. The event analyzer writes reconstructed events into a PAW-compatible ntuple

---

<sup>1</sup>Terms event analyzer (or simply analyzer) and analysis engine (or simply engine) refer to the same code.

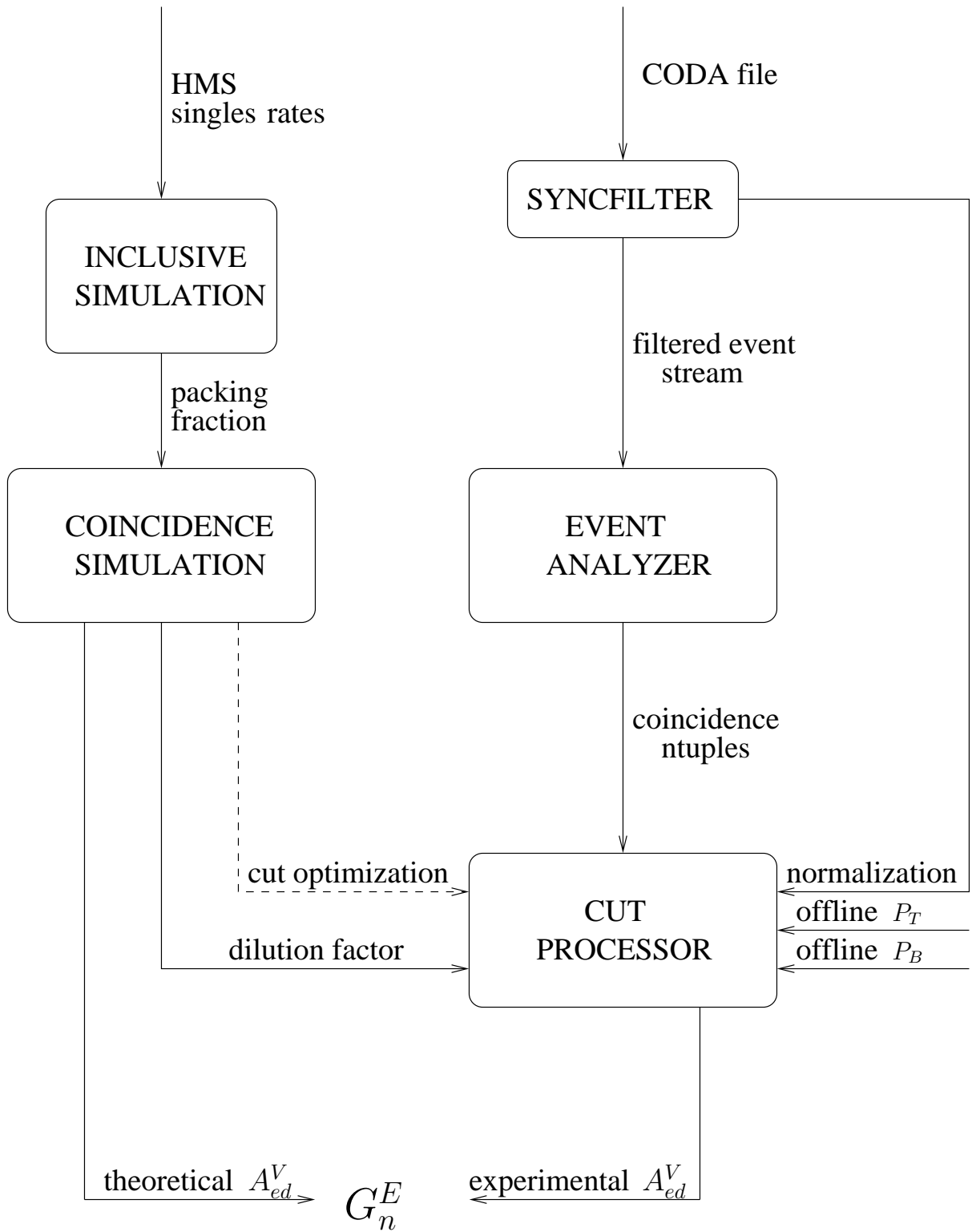


Figure 6.1: Data analysis software.

file. The experimental asymmetries are calculated by the cut processor, whose function is to count quasi-elastic neutron events for both helicities from the ntuples, calculate run-by-run asymmetries and then asymmetry averages (by target material, beam and target polarization sign etc.). Calculating asymmetries requires the knowledge of the dilution factor, which is supplied by the coincidence Monte Carlo. The packing fraction for the dilution factor calculation is obtained using inclusive simulations.

## 6.2 Syncfilter

Historically, a need for a data stream preprocessor came about due to the FastBus synchronization problem (hence the name *syncfilter*). Later, a number of other issues, such as non-zero BCM readings, analysis crashes due to missing end-of-run events, and computer dead-time correction, have come up, and syncfilter proved to be the most convenient tool for solving them. Let us review different aspects of syncfilter usage in more detail.

**Synchronization errors** During E-93026 the DAQ system used several autonomous crates for data processing, each of them having an independent internal event counter. Matching of different counters was checked every time a *synchronization event* was generated (about every two seconds). In case of a mismatch an error event was generated, which indicated that all data during the last synchronization

interval would have to be discarded. The error event followed the questionable piece of data in the data stream. However, the analyzer does not have event memory, and therefore cannot make use of an error warning issued post-factum. This problem was solved using a data stream preprocessor, which accumulated input data in a buffer, and inverted the relative order of the error event and the data to which it referred. In practice, synchronization errors occurred only in a few runs, and even there the fraction of bad sync events did not exceed one percent.

**Missing end-of-run events** In case of a ROC crash during a run, the end-of-run event is normally not inserted into the raw data file, which in its turn made replay engine crash without producing any meaningful results. To prevent the loss of these data (which are in most cases perfectly usable), syncfilter was used to insert fictitious end-of-run events when encountering an unexpected end of the input data.

**Low beam current** The beam current was not always stable. Low beam current often correlated with low beam quality. Additionally, the beam current monitors exhibit significant non-linearity for  $I_{BEAM} < 50$  nA. Therefore, it has been decided to discard the low current ( $I_{BEAM} < 50$  nA) data with the use of the syncfilter.

**Computer dead-time** Once the DAQ receives an event, it becomes unable to process another one for a short period of time (normally, a few nanoseconds). Since scalers accumulate beam charge regardless to whether or not the DAQ was ready for taking data, event rates (and therefore measured asymmetries) require a dead-time

correction. In E93-026 we used syncfilter to take care of this issue by ignoring the beam charge accumulated during the busy status of the DAQ.

A detailed description of the syncfilter can be found in [58].

## 6.3 Hall C replay engine

The event analyzer for E93-026 was based on standard CSOFT package of Hall C. This software package includes a number of C libraries for processing CODA files and Fortran utilities for event reconstruction in Hall C spectrometers, HMS and SOS. Hall C replay engine has a run-time programming mechanism called CEBAF Test Package (CTP) [59] to dynamically (i.e. without making changes to the source code) modify:

- parameters used by engine, such as detector configuration, particle masses etc.
- cuts on both raw and analyzed events
- output histograms (conditioned by cuts)
- format of output scaler files

The source code of the analysis engine can be broken down as follows:

**Initialization section** resets the counters, registers CTP variables, reads the configuration file, reads in detector decoding map, parameters database and TBPM

thresholds from corresponding files and opens the input data stream from a raw CODA file either directly or piped through the syncfilter.

**Non-physics events processing section** extracts information stored in control events, including spectrometer settings, target number, detector high voltages, run start time etc., and checks synchronization status for sync events.

**Physics events analysis section** does most of the actual analysis job. It begins with calculating beam-related quantities (so called “beam reconstruction”) and then depending on the event type does or skips HMS, neutron detector and coincidence reconstructions.

**Shut-down section** saves epics, scaler, statistics and other output files, closes ntuples, writes out pedestal values, calculates new TDC offset from laser pulser events and writes the final summary.

### **6.3.1 HMS event reconstruction**

HMS event reconstruction involved two steps: focal plane reconstruction and target quantities reconstruction. Focal plane reconstruction determines the coordinates and slopes of the particle track in the spectrometer focal plane and passes them to the target reconstruction routine, which calculates target track quantities such

as vertex coordinates, track slopes at the target and the relative deviation of the particle momentum from the central momentum of the spectrometer,  $\delta_{HMS}$ .

### **Focal plane reconstruction**

Focal plane reconstruction decodes detector hits and calculates focal plane track coordinates and slopes. All procedures involved in this step are standard ones and did not undergo any customization during E93-026 (an outline of standard HMS reconstruction as well as further references can be found at [40]). If a valid focal plane track was found, then the algorithm proceeds to the next step:

### **Target quantities reconstruction**

Since HMS optics is very well known, a standard reconstruction (i.e. no target field, no beam rastering) can be done by simply applying a non-linear matrix transformation to the four focal plane quantities (coordinates  $x$ ,  $y$  and slopes  $x'$ ,  $y'$ ) [60]. For our experiment, however, the situation is more complicated because of curvature of charged particle tracks by the target field and a large vertical beam offset due to beam rastering. To correctly account for these, a doubly nested iterative approach was adopted.

Reconstruction with a beam offset but without the target field can be done through the following steps:

1. Do the standard reconstruction assuming no vertical offset ( $X = 0$ ) to get a

first guess of the target quantities.

2. Apply forward transport transformation to the target quantities assuming  $X = 0$ . Repeat the forward transport transformation with the actual vertical beam offset  $X = X_{BEAM}$  and calculate the change in focal planes quantities due to the beam offset.
3. Apply the focal plane corrections calculated in the previous step and repeat the backward reconstruction to get the next iteration values of the target coordinates.
4. Repeat steps 2-4 until difference between two consecutive iterations in  $\delta_{HMS}$  is less than a pre-defined value.

With the use of this procedure it is now possible to correct for the effect of the magnetic field as follows:

1. Apply the reconstruction procedure described above to the measured focal plane quantities to obtain a first guess estimate of the virtual target coordinates<sup>2</sup>.
2. Drift the electron to a field-free region, then track it back<sup>3</sup> into the magnetic field to the intersection point with the incident beam. That gives the first guess of the real target coordinates.

---

<sup>2</sup>Virtual target coordinates are defined as a set of target coordinate that would result in the same focal plane quantities as the measured ones if there were no magnetic field present.

<sup>3</sup>Tracking through the target field was done by solving the differential equations of motion in a magnetic field using Runge-Kutta method.

3. Calculate the correction for the virtual beam offset and apply it.
4. Apply the beam-offset reconstruction procedure to the corrected focal plane quantities to get a better estimate for the virtual target coordinates
5. Drift the electron to the field-free region, then track it back to the intersection point with the incident beam to get a better estimate for the real target coordinates.
6. Repeat steps 3-5 until the reconstructed vertical position in the beam plane is equal to the actual one within a predetermined error.

Normally, the algorithm converged within 5 iterations. The events where convergence is not achieved (which happened in less than 0.1% of cases) were discarded.

### **6.3.2 Neutron detector event reconstruction**

The neutron detector reconstruction can be structured as follows:

1. Single hit analysis
2. Tracking
3. Particle identification.

All code pertaining to the neutron detector side analysis was combined into one subroutine named `n_reconstruction`. The subroutine begins with clearing all old event data by calling `n_reset_event`. Then it finds all hits with acceptable TDC

values and calculates raw TDC differences. After that, the event type is checked and in case of a laser pulser event the control is passed to special subroutines (`n_analyze_pindiode` and `n_analyze_laser_event`). If the event is a physics one, the algorithm proceeds to procedure `n_time_correct`. This procedure applies timing corrections, including event-to event path length, velocity difference and pulse height (walk) corrections. Having thus concluded analyzing single hits, the subroutine then calculates quantities needed by coincidence reconstruction (layer averages, coincidence time, and electron momentum transfer in neutron detector coordinates) and finally does the tracking (`ndet_tracking`) and particle identification (`ndet_pid`) as described below.

## **Tracking**

The neutron detector tracking routine `ndet_tracking` combines single hits into one or several tracks. In order to be assigned to the same track single hits need to have similar meantimes (within  $\pm 10$  ns) and match the kinematic acceptance.

The main part of the routine consists of two nested loops: the outer one loops over all bars in all planes, looking for an unused hit to start a track with. The inner loop checks unused hits in subsequent layers; if a hit falls within the meantime window and the line connecting the tested hit with the last one on the track falls within the kinematic acceptance, the hit is added to the track and labeled as used. After hits have been sorted into tracks, line regression routines are called to fit the tracks to straight line. Finally, the routine calculates track slopes and checks for a

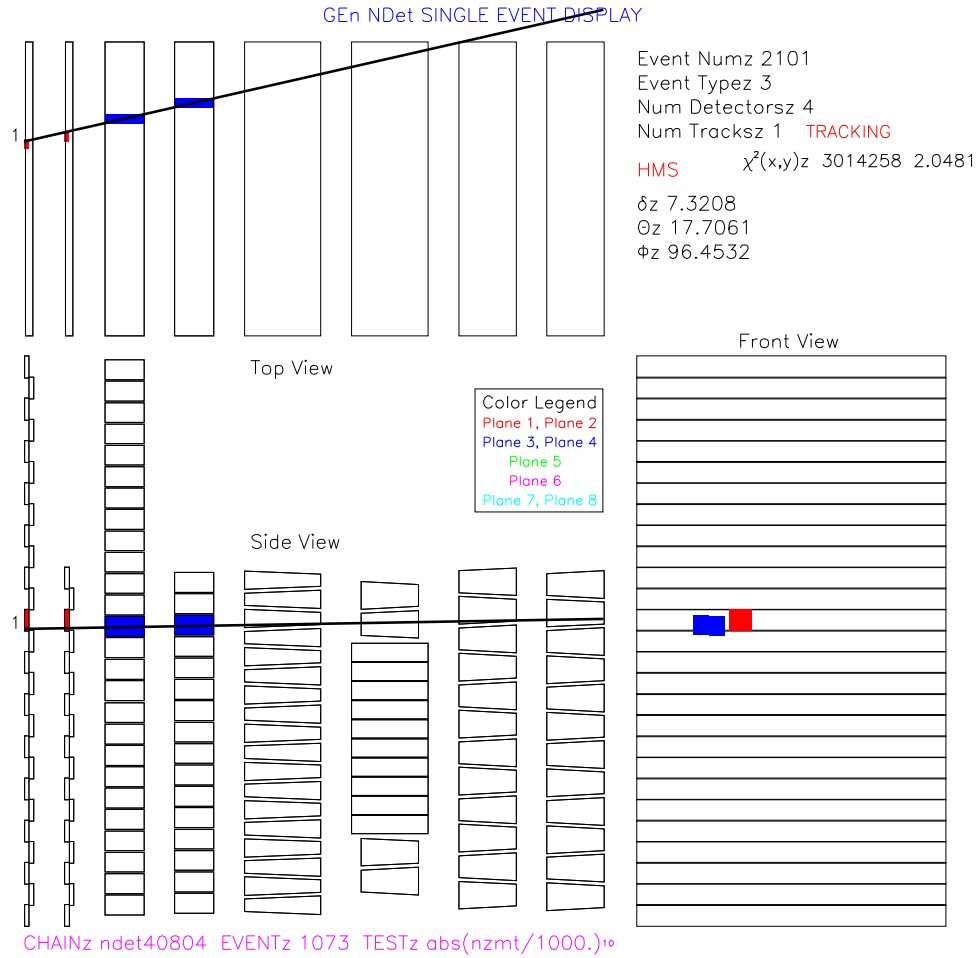


Figure 6.2: A proton event in the neutron detector

fired paddle on the track with energy deposited above minimum. Paddle hits play a key role in the particle identification process outlined in the next paragraph.

### Individual track PID

The neutron detector tracking subroutine `ndet_tracking` starts by testing minimum track energy and track coincidence time requirements. If both tests are passed, the routine determines the individual track PID by looking at paddle hits and at the

Table 6.1: Event PID

PID code	description	frequency(%)
No track or bad track(s)		
0	no track	7.9
-1	single bad track	0.2
-2	one proton and one neutron track, neither used	5.4
-3	multiple tracks, all bad/non-proton	0.0
Good proton		
1	one proton track – also used for individual tracks	11.9
2	only reasonable track is proton	0.02
3	better of 2 proton tracks – based on $\theta_{nq}$ probability	1.9
4	better of 2 proton tracks – other has bad $\chi^2$	0.02
5	better of 2 proton tracks – other has bad time	0
8	best track of several is proton – $\theta_{nq}$ probability	0
Paddle track		
9	paddle track	57.7
Good neutron		
11	one neutron	12.8
12	only reasonable track is neutron	0.1
13	better of 2 neutron tracks – based on $\theta_{nq}$ probability	1.5
14	better of 2 neutron tracks – other has bad $\chi^2$	0.1
15	better of 2 neutron tracks – other has bad time	0

initial hit of the track (the one in the plane closest to the target). The scheme of the PID algorithm is given in in Table 6.2. Most events are identified by absence (neutron) or presence (proton) of a paddle hit, but there are two important exceptions:

- tracks started at the 1st bar plane<sup>4</sup> at counter 17 or above are always labeled as protons;
- tracks started at bar planes 3-6 are always labeled as neutrons.

---

<sup>4</sup>i.e. 3rd detector plane (first two planes are paddles)

Table 6.2: Individual track PID

Track started at		PID if	
plane	counter	paddle hit	no paddle hit
1	17-27	proton	proton
1	1-16	proton	neutron
2	any	proton	neutron
3-7	any	neutron	neutron

### Track selection and PID flags

For two-track events, the better track is found according to the algorithm described below:

- check track PIDs; if same nucleons, proceed, otherwise, discard both tracks;
- check track  $\chi^2$  (if exactly one track fails the  $\chi^2$  check, pick the remaining track; otherwise, proceed with other checks)
- check track time (in the same fashion as above)
- if still have two contenders, pick the track with greater  $\theta_{pq}$  probability.

Multiple (3 or more) track events with heterogeneous nucleons or multi-neutron tracks were discarded. For multi-proton events, the track with the best  $\theta_{pq}$  probability was chosen.

A case when a track consisted of paddle hits only (so-called *paddle track*) was labeled with a special PID code. Although a significant part of paddle tracks are

protons, their contamination by electronics noise makes paddle events essentially unusable.

The PID codes are summarized in the table 6.1.

### 6.3.3 Kinematic calculations

Once the tracking has been done, the engine calculates kinematic quantities. There are two subroutines responsible for this task, `h_physics` (electron arm kinematics) and `c_physics` (coincidence kinematics).

These calculations use two coordinate systems: the spectrometer (or transport) one and the beam one. The  $x$  axis in both coordinate systems is pointing vertically down,  $z$  is given by the beam momentum for the beam system and the spectrometer for the spectrometer system, and  $\vec{y} = \vec{z} \times \vec{x}$ .

#### Electron arm

The momentum of the incident electron in the beam coordinate system is simply given by

$$\vec{k} = (0, 0, E_{vx}), \quad (6.1)$$

where  $E_{vx} = E - E_{loss}$  is the vertex electron energy which differs from the nominal beam energy  $E$  by pre-scattering energy loss  $E_{loss}$ . In the spectrometer coordinate

system the scattered electron momentum is given by

$$\frac{P_{vx}}{\sqrt{1 + (x')^2 + (y')^2}}(x', y', 1), \quad P_{vx} = \sqrt{E_{vx}^2 - m_e^2} \quad (6.2)$$

where  $x'$  and  $y'$  are the electron track slopes,  $P$  is the measured electron momentum,  $m_e$  is the electron mass,  $E_{vx} = E - \Delta E_{loss}$  and  $P_{vx}$  are vertex energy and momentum correspondingly, and  $\Delta E_{loss}$  is the post-scattering energy loss. The momentum components in the beam coordinate system are easily obtained by a rotation to the spectrometer angle  $\theta_{sp}$ :

$$\vec{k}' = \frac{E'}{\sqrt{1 + (x')^2 + (y')^2}}(x', y' \cos \theta_{sp} - \sin \theta_{sp}, y' \sin \theta_{sp} + \cos \theta_{sp}). \quad (6.3)$$

The analysis code uses the components of this vector to calculate the scattering angle  $\theta_e$  and the out-of-plane angle  $\phi_e$ :

$$\theta_e = \arccos \frac{k'_z}{|\vec{k}'|} \quad (6.4)$$

$$\phi_e = \arctan \frac{k'_y}{k'_x}. \quad (6.5)$$

The four-momentum transfer squared  $Q^2$  and the invariant mass  $W$  are readily obtained from the four-momenta  $k_\mu$  and  $k'_\mu$ :

$$Q^2 = -q^\mu q_\mu \quad (6.6)$$

$$W = \sqrt{(q^\mu + T^\mu)(q_\mu + T_\mu)}, \quad (6.7)$$

where  $q_\mu = k_\mu - k'_\mu$  is the four-momentum transfer and  $T_\mu$  is the four-momentum of the struck nucleon in the lab frame,  $T_\mu = (M, 0, 0, 0)$ .

### Nucleon arm

The subroutine `c_physics` calculates  $\theta_{nq}$ , the angle between the momentum transfer  $\vec{q}$  and the track of the nucleon, and  $\theta_{np}^{cm}$ , the angle between the relative n-p momentum with respect to the momentum transfer in the n-p center of mass system.

The first step in the calculation is forming the unit vector in the direction of the momentum transfer,  $\hat{q} = \vec{q}/|\vec{q}|$ , and then transforming it to the neutron detector frame,  $\hat{q} \rightarrow \hat{q}'$

$$\vec{q}' = (q_x, q_y \cos \theta_{nDet} - q_z \sin \theta_{nDet}, q_y \sin \theta_{nDet} + q_z \cos \theta_{nDet}). \quad (6.8)$$

The direction of the nucleon track is characterized by vector  $\Delta\vec{n} = (\Delta x, \Delta y, 1)$ , where  $\Delta x$  and  $\Delta y$  are slopes of the nucleon track determined by the tracking subroutine. Then  $\theta_{nq}$  is simply the angle between  $\Delta\vec{n}$  and  $\vec{q}'$ . For convenient cancellations,  $\vec{q}'$  is replaced with a collinear vector  $\Delta q = \vec{q}'/q'_z$ :

$$\cos \theta_{nq} = \frac{\Delta\vec{n} \cdot \Delta\vec{q}}{|\Delta\vec{n}| \cdot |\Delta\vec{q}|} = \frac{(\Delta\vec{n})^2 + (\Delta\vec{q})^2 - (\Delta\vec{n} - \Delta\vec{q})^2}{2|\Delta\vec{n}| \cdot |\Delta\vec{q}|}. \quad (6.9)$$

A Lorentz boost to the center of mass system gives then  $\theta_{np}^{cm}$  [40]:

$$\theta_{np}^{cm} = \pi - \arctan \left[ \sin \theta_{nq} \left( \frac{\nu + M_D}{E_{tot}^{cm}} \cos \theta_{nq} - \frac{qE_n}{E_{tot}^{cm} P_n} \right)^{-1} \right], \quad (6.10)$$

where  $\nu$  and  $q$  are energy and momentum transfer,  $M_D$  is the mass of the deuteron,  $E_n$  and  $P_n$  are the energy and the nucleon momentum of the knocked out nucleon as determined from the time of flight, and  $E_{tot}^{cm} = \sqrt{(\nu + M_D)^2 - q^2}$  is the total energy in the center of mass system.

## 6.4 Inclusive simulations

Inclusive simulation software was designed for calculating packing fraction of the polarized target (see Section 7.5). The basic components of the software package include the quasi-free scattering cross-section model, radiative corrections and acceptance simulation. The simulation was run separately for each target materials. Contributions from each target material were added with proper weights to represent kinematic spectra of actual composite targets.

### 6.4.1 Cross-section model

Inclusive electron scattering cross-sections were simulated using the QFS code by J. W. Lightbody and J. S. O'Connell [61]. The model assumed incoherent scattering through following reaction mechanisms:

- quasielastic scattering off a bound nucleon
- two-nucleon emission
- $\Delta$ -resonance electroproduction
- two higher resonances ( $W = 1.5$  GeV and  $W = 1.7$  GeV)
- deep inelastic scattering (in the  $x$ -scaling regime)

The  $N(e, e')$  scattering cross section was calculated from the Rosenbluth formula (see Eq.(2.10)). A standard dipole parametrization  $G_D = (1 + Q^2/0.71)^{-2}$  was used for  $G_p^E$ ,  $G_p^M$  and  $G_n^M$ . The charge form-factor of the neutron was approximated by Galster parametrization  $G_{Galster} = \frac{\mu\tau}{1+b\tau}G_D$  with  $b = 5.6$ .

The sum of elementary quasielastic cross sections was multiplied by a Gaussian in electron energy loss, centered at  $Q^2/(2M) - \epsilon_s$ , and with a width proportional to  $qk_F/M$ , where  $\epsilon_s$  is the mean separation energy and  $k_F$  is the Fermi momentum of the target nucleus. This Gaussian smearing accounted for the Fermi motion of nucleons inside the nucleus.

The two-nucleon emission process, expected to be of significance in the dip region between the quasifree and delta production peaks, was calculated as:

$$\sigma(Q^2, \nu, \theta) = \sigma_{Mott}(\theta) \left[ \frac{Q^2}{2q^2} + \tan^2\left(\frac{\theta}{2}\right) \right] R_{2N}(Q^2, \nu), \quad (6.11)$$

where  $\theta$  and  $\nu$  are electron scattering angle and energy loss, correspondingly. The response function  $R_{2N}(Q^2, \nu)$  was parametrized as follows:

$$R_{2N}(Q^2, \nu) = K_{2N}(NZ/A)q^2 G_D(Q^2, \Lambda_{2N}) \left( \frac{\Gamma_{2N}^2 W^2}{(W - W_{cm})^2 + \Gamma_{2N}^2 W^2} \right) \times \left[ 1 - \exp\left(-\frac{(\nu - \nu_{thr})}{\Gamma_{thr}}\right) \right], \quad (6.12)$$

where  $N = A - Z$ ,  $Z$  and  $A$  are the number of neutrons, protons, and all nucleons in the nucleus, correspondingly,  $K_{2N}$  is the two-nucleon knockout strength,  $G_D(Q^2, \Lambda_{2N}) = (1 + Q^2/\Lambda_{2N}^2)^{-2}$  is the dipole form,  $W$  is the invariant mass,  $W_{cm} = (M + M_\Delta)/2$ ,  $\nu_{thr} = Q^2/4M$  is the threshold energy loss,  $\Gamma_{2N}$  and  $\Gamma_{thr}$  are the width and the threshold scale of the Lorentzian, both determined from the data.

The resonance contributions to the total cross sections, both for  $\Delta$  and the higher resonances, also had Lorentzian shape as in Equation (6.13):

$$\sigma_\Delta = K_\Delta A q^2 G_D(Q^2, \Lambda_\Delta) \left( \frac{\Gamma_\Delta^2 W^2}{(W - W_{cm})^2 + \Gamma_\Delta^2 W^2} \right) \times \left[ 1 - \exp\left(-\frac{(\nu - \nu_{thr})}{\Gamma_{thr}}\right) \right], \quad (6.13)$$

with the width

$$\Gamma = \sqrt{\Gamma_R^2 + \Gamma_Q^2 + \Gamma_A^2} \quad (6.14)$$

determined by the three components: natural resonance width  $\Gamma_R$ , Fermi broadening component  $\Gamma_Q$  and nuclear medium effects component  $\Gamma_A$ .

Finally, the deep inelastic scattering cross section was approximated with the following expression:

$$\sigma = \Gamma_v \sigma_\gamma(\nu)(1 + \epsilon R_x) F_x^2(Q^2), \quad (6.15)$$

where  $\Gamma_v$  is the virtual photon flux,

$$\Gamma_v = \frac{\alpha}{2\pi^2} \frac{E' \kappa}{EQ^2} \frac{1}{1 - \epsilon}, \quad \kappa = \nu - \frac{Q^2}{2M}, \quad (6.16)$$

$\epsilon$  is the virtual photon polarization,  $F_x(Q^2)$  is a form factor,  $R_x$  is the ratio of longitudinal to transverse cross sections, and  $\sigma_\gamma(\nu)$  is the real photon cross section. Parametrization of ingredients of the deep inelastic scattering cross section is given below:

$$R_x = 0.56 \times 10^6 (\text{MeV}/c)^2 / (Q^2 + M_N^2), \quad (6.17)$$

$$\sigma_\gamma(\nu) = \left( \sigma_0 + \frac{\sigma_1}{\nu - \nu_\pi} \right) \left[ 1 - \exp\left( -\frac{(\nu - \nu_\pi)^2}{2\Gamma_x^2} \right) \right], \quad (6.18)$$

$$F_x^2(Q^2) = a_1 \exp(-a_2 Q^2) + b_1 \exp(-b_2 Q^2) + c_1 \exp(-c_2(Q - c_3)^2), \quad (6.19)$$

where the parameters  $a_i$ ,  $b_i$  and  $c_i$  are defined in the Table 6.3.

Table 6.3: Deep inelastic scattering form factor parameters

$a_1$	$a_2$	$b_1$	$b_2$	$c_1$	$c_2$	$c_3$
0.55	$2 \cdot 10^{-5}$	0.45	$0.45 \cdot 10^{-6}$	0	$0.1 \cdot 10^{-12}$	$4 \cdot 10^{-6}$

$A$	$k_f$ (MeV)	$\epsilon_s$ (MeV)
4	180	20
9	200	20
12	221	20
15	240	20
27	250	25
59	260	35
64	260	35

Table 6.4: Fermi momenta and separation energies of nuclei used in simulation.

### 6.4.2 QFS parameters

The Fermi momentum and the separation energy of the nucleus were looked up in a special table. The lookup code and the table itself (see Table 6.4) were added to QFS by C. Harris [41]. He also updated some internal parameters of QFS regulating widths and strengths of various resonance contributions. A summary of these changes is given in Table 6.5.

### 6.4.3 Deuterium cross sections

The nucleus of deuterium, the deuteron, consists of one neutron and one proton. The QFS model of quasielastic scattering cross section is based on the Fermi gas model, i.e. is largely statistical. Therefore, it is not surprising that this model breaks down for a system consisting of just two constituents.

In order to overcome this difficulty, a special subroutine for electron-deuteron scattering was designed by C. Harris. In this subroutine, the total cross-section was calculated as a sum of a quasielastic part based on  $y$ -scaling model and the deep

Table 6.5: Updated internal parameters of QFS

physics name	name in QFS	original value	modified value	description
$\Gamma_x$	GAMO	650 MeV	610 MeV	width parameter for the real photon cross-section
$\Lambda_{2N}$	AR	570 MeV	550 MeV	dipole form parameter for the two-nucleon knockout
$\Lambda_\Delta$	AD	linear in A	774 MeV	dipole form parameter for the $\Delta$ electroproduction for $1 < A < 4$
$\Gamma_{thr}^\pi$	GAMPI	5 MeV	50 MeV	threshold scale for $\Delta$ electroproduction
$\gamma_R$	GAMR	120 MeV	100 MeV	scale factor for Fermi broadening contribution to $\Delta$ -resonance width

inelastic part. The latter was obtained from a fit to the resonance region data.

The quasielastic contribution to the cross section was calculated using the Krautschneider momentum distribution [62]:

$$n(k) = A \left[ C + \left( \frac{1}{k^2 + \kappa_1} - \frac{1}{k^2 + \kappa_2} \right)^2 \right], \quad (6.20)$$

where  $A$ ,  $\kappa_1$  and  $\kappa_2$  are empirical constants and  $C$  is the term responsible for rescattering. In our simulation the rescattered term was assumed to be zero.

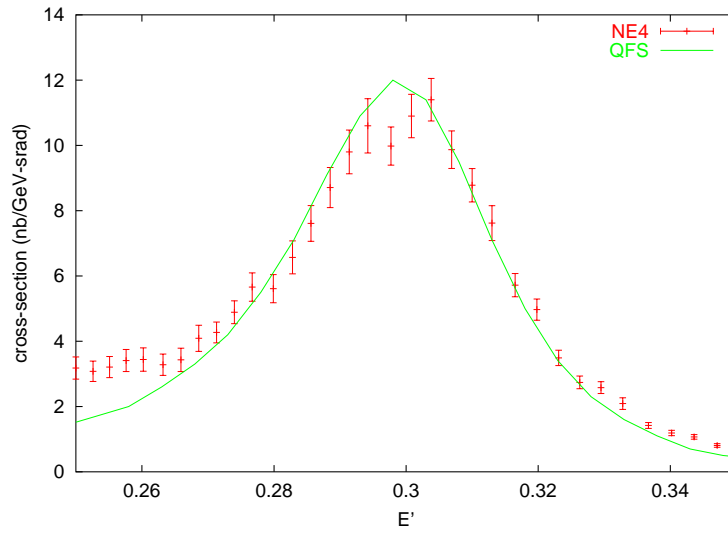
The results of the simulations for deuterium compared to experimental data can be found in Fig. 6.3. The agreement is better than 10% except far from the quasielastic peak, which is adequate for the needs of the experiment.

#### 6.4.4 Radiative effects

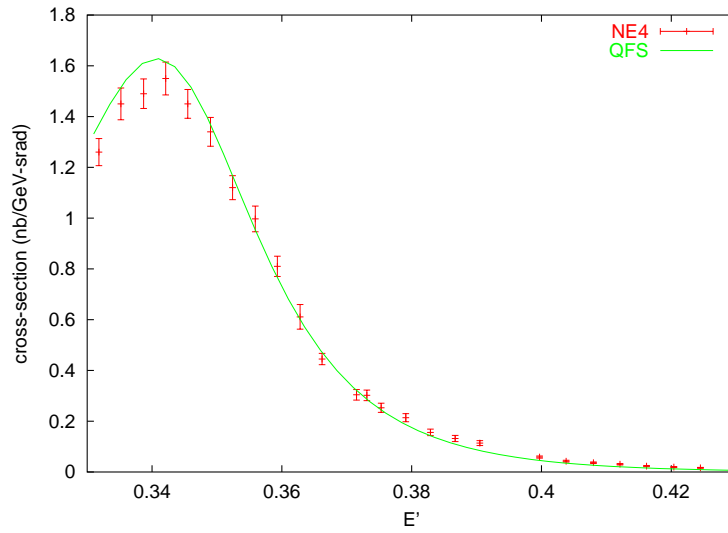
The code for calculating both internal and external radiative corrections was provided by J. Arrington [56]. Unradiated cross-sections were taken as input from QFS. The calculations were based on a peaking approximation formula derived by Stein [64] for the particular case of quasi-elastic scattering from a more general formula by Mo and Tsai [65]:

$$\sigma = \sigma_{soft} + \sigma_{pre} + \sigma_{post},$$

Figure 6.3: QFS versus NE4 data for transverse scattering [63].



(a) Beam energy  $E = 841$  MeV



(b) Beam energy  $E = 1281$  MeV

$$\begin{aligned}
\sigma_{soft} &= \left(\frac{R\Delta E}{E'}\right)^{b(t_b+t_a)} \left(\frac{\Delta E}{E'}\right)^{b(t_b+t_a)} \left[1 - \frac{\xi/\Delta E}{1 - b(t_a + t_b + 2t_r)}\right] \bar{\sigma}(E, E') \\
\sigma_{pre} &= \int_{E_{min}(E')}^{E-R\Delta E} \bar{\sigma}(\epsilon, E') \left(\frac{E-\epsilon}{E'R}\right)^{b(t_a+t_r)} \left(\frac{E-\epsilon}{E}\right)^{b(t_b+t_r)} \\
&\quad \left[\frac{b(t_b+t_a)}{E-\epsilon} \phi\left(\frac{E-\epsilon}{E}\right) + \frac{\xi}{2(E-\epsilon)^2}\right] d\epsilon \\
\sigma_{post} &= \int_{E'+\Delta E}^{E'_{max}} \bar{\sigma}(E, \epsilon') \left(\frac{\epsilon'-E'}{\epsilon'}\right)^{b(t_a+t_r)} \left[\frac{(\epsilon'-E')R}{E}\right]^{b(t_b+t_r)} \\
&\quad \left[\frac{b(t_b+t_a)}{\epsilon'-E'} \phi\left(\frac{\epsilon'-E'}{\epsilon'}\right) + \frac{\xi}{2(\epsilon'-E')^2}\right] d\epsilon'. \tag{6.21}
\end{aligned}$$

Here  $\sigma_{soft}$ ,  $\sigma_{pre}$  and  $\sigma_{post}$  are soft photon, hard photon pre- and post-radiation contributions to the total radiated cross section correspondingly,

$$R = \frac{M_T + 2E \sin^2 \frac{\theta}{2}}{M_T - 2E' \sin^2 \frac{\theta}{2}}$$

is a kinematic factor,  $M_T$  is the target nucleus mass,  $t_b$  and  $t_a$  are the target thicknesses before and after the interaction point,

$$t_r = \frac{\alpha}{\pi} \left[ \log \left( \frac{Q^2}{m_e^2} \right) - 1 \right]$$

is the equivalent radiator thickness accounting for internal bremsstrahlung. Other ingredients of Eq. 6.21 are:

$$b = \frac{4}{3} \left[ 1 + \frac{1}{9} \frac{Z+1}{Z+\eta} \log^{-1}(183Z^{-1/3}) \right],$$

$$\eta = \log(1440Z^{-2/3}) / \log(183Z^{-1/3}),$$

$$\bar{\sigma}(E, E') = \tilde{F}(Q^2) \sigma(E, E'),$$

$$\begin{aligned} \tilde{F}(Q^2) = 1 + 0.5772 \times b(t_a + t_b) + \frac{2\alpha}{\pi} \left( -\frac{14}{9} + \frac{13}{12} \log \frac{Q^2}{m^2} \right) - \\ - \frac{\alpha}{2\pi} \log^2 \frac{E}{E'} + \frac{\alpha}{\pi} \left[ \frac{1}{6} \pi^2 - \Phi(\cos^2 \theta/2) \right], \end{aligned}$$

$$\xi = \frac{\pi m}{2\alpha} \frac{t_a + t_b}{(Z + \eta) \log(183/Z^{1/3})},$$

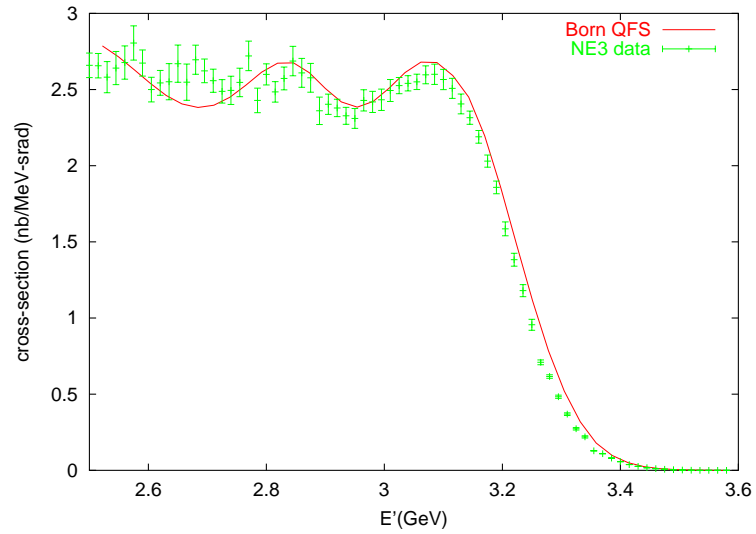
and finally,  $\Delta E$  is the energy cutoff (determined by detector resolution or other experimental considerations) and

$$\Phi(x) = \int_0^x \frac{-\log|1-y|}{y} dy$$

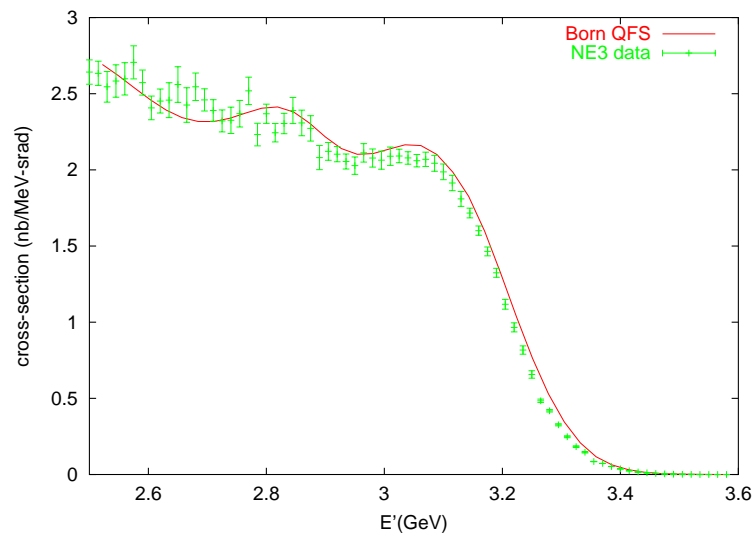
is the Spence function.

The numerical integration was performed using the Romberg technique. The results were checked by comparing to the cross-section data from the SLAC experiment NE3 (see Fig. 6.4). The agreement is excellent for both radiatively corrected and uncorrected data.

Figure 6.4: Comparison between SLAC NE3 [66] data and simulations. Carbon target. Thickness (including equivalent radiator)  $t = 3.26\%$  of the radiation length. Beam energy is 3595 MeV, the scattering angle is  $16^\circ$ .



(a) Born cross-sections



(b) Radiated cross-sections

## 6.4.5 Acceptance effects

The HMS efficiency is momentum dependent. Therefore, when comparing results of simulations to experimental data one needs to account for acceptance effects.

For E93-026 the HMS momentum acceptance was calculated from data taken with the same beam energy  $E = 2.06$  GeV and spectrometer angle  $\theta_{HMS} = 18.5^\circ$ , but two different central momenta,  $P_{HMS}^1 = 2.060$  GeV and  $P_{HMS}^2 = 1.963$  GeV. In the  $E'$  region where the momentum acceptance is flat for both data sets the difference in shape of their  $E'$  spectra is entirely due to acceptance effects (since the kinematics are the same). This allows one to deconvolute the cross-section and the acceptance function using the procedure described below [67].<sup>5</sup>

1. add together<sup>6</sup>  $E'$  spectra of the two data sets,  $C_1(E')$  and  $C_2(E')$ , as the first guess for the cross-section,

$$\sigma_0(E') = \frac{w_1 C_1(E') + w_2 C_2(E')}{w_1 + w_2}$$

2. divide out the cross-section from the  $E'$  spectra, change variables from  $E'$  to  $\delta$ , and add the results, resulting in an estimate for the acceptance function  $\eta^i$ :

$$\eta_1^i = \frac{C_1(E')}{\sigma_i(E')} \quad \eta_2^i = \frac{C_2(E')}{\sigma_i(E')} \quad \eta^i(\delta) = \frac{w_1 \eta_1 [P_{HMS}^1(1 + \delta)] + w_2 \eta_2 [P_{HMS}^2(1 + \delta)]}{w_1 + w_2}$$

---

<sup>5</sup>For a correct understanding of the procedure it is important to realize that the momentum acceptance is a function of the *relative* momentum  $\delta = \frac{\Delta P}{P} = \frac{E' - P_{HMS}}{P_{HMS}}$ , whereas cross-sections are functions of  $E'$ . Therefore, if we express the acceptance function in terms of  $E'$ , its horizontal scale will depend on the central momentum of the spectrometer  $P_{HMS}$ .

<sup>6</sup>If statistics are limited, proper statistical weights  $w_{1,2}$  are necessary

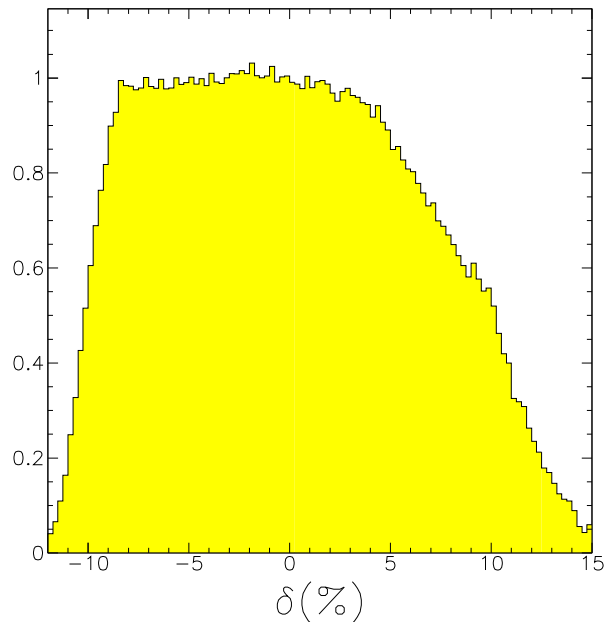


Figure 6.5: HMS momentum acceptance.

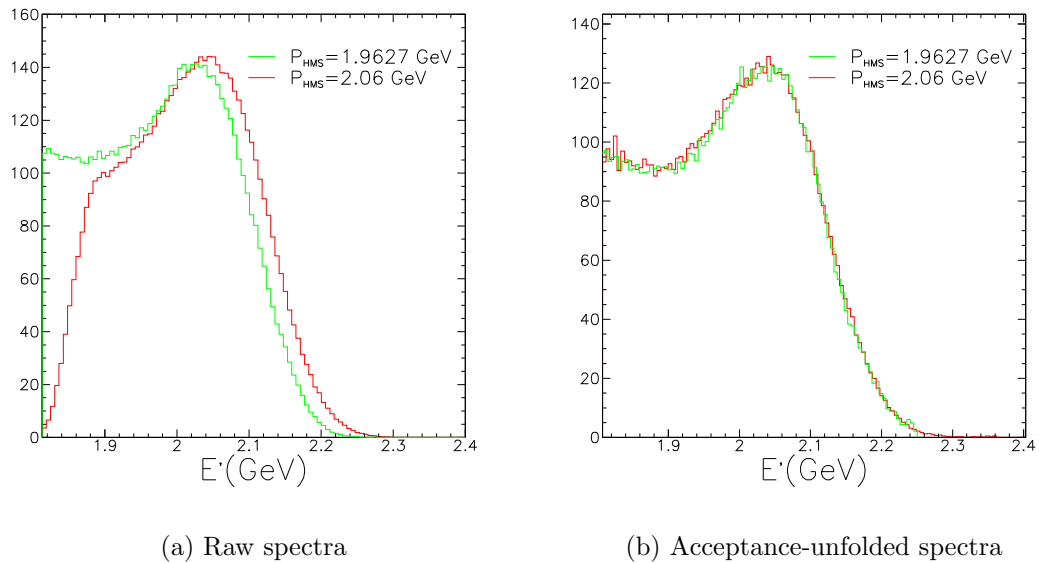


Figure 6.6: HMS acceptance effects:  $E'$  spectra for carbon runs 40466 and 40655 ( $P_{HMS} = 2.06$  GeV and  $P_{HMS} = 1.9627$  GeV) before (a) and after (b) unfolding acceptance effects.

3. divide out the acceptance function obtained in the previous step from the last iteration of the cross-section and add the results together, resulting in an improved result for the cross-section:

$$\sigma_1^i = \frac{C_1(E')}{\eta^i [P_{HMS}^1 (1 + \delta)]} \quad \sigma_1^i = \frac{C_1(E')}{\eta^i [P_{HMS}^1 (1 + \delta)]} \quad \sigma^i = \frac{w_1 \sigma_1^i + w_2 \sigma_1^i}{w_1 + w_2}$$

4. repeat steps 2-3 until cross-sections extracted from the two data sets agree within a pre-defined range.

The acceptance function as obtained in the above procedure is shown in Figure 6.5. The asymmetry in the shape of the acceptance function is due to the target field and finite extension of the target along the beam direction.

Figure 6.6 shows the results of the unfolding procedure for two runs taken with different HMS central momenta,  $P_{HMS} = 2.06$  GeV and  $P_{HMS} = 1.9627$ . Good agreement between the unfolded spectra for the two runs shows that unfolding procedure has been done correctly.

### 6.4.6 Composite target models

In experiment E93-026 in addition to normal production data taken with the polarized  $^{15}\text{ND}_3$  target, some data were also taken with carbon and empty targets. Empty and carbon data can be taken with target nose filled with helium (“wet” runs) or empty (“dry” runs), which gives four combination of fixed-thickness tar-

Table 6.6: Target material thicknesses

	wet carbon	dry carbon	wet empty	dry empty	$^{15}\text{ND}_3^*$	$\eta/t^{**}$
Al	1.5 mm	1.5 mm	1.5 mm	1.5 mm	1.5 mm	10.0
C	6.9 mm	6.9 mm	–	–	–	18.83
He	31 mm	–	40 mm	–	25 mm	3.63
N	–	–	–	–	15 mm	5.07
D	–	–	–	–	15 mm	15.0
rad. length	6.1%	5.2%	2.6%	1.7%	5.8%	–

\* Assuming 50% packing fraction

\*\* Luminosity per unit length ( $nA\frac{q}{\text{cm}^3}$ )

gets<sup>7</sup>. Each target has a different radiation length and therefore the simulation for the same target material used in different targets has to be done separately. The cross-sections for each target material were weighted with luminosities and then added together. The luminosities were calculated based on the table of material thicknesses in electron’s path compiled by C. Harris [41].

### 6.4.7 Comparison of simulation results to experimental data

The results of simulations are shown in comparison with our experimental data in Figure 6.7. The comparison is given for three types of fixed-thickness targets: dry carbon target, carbon target with helium in the nose, and helium target. The results of the simulation agree with our experimental data to 10%. This level of agreement is sufficient for the goals of the experiment.

---

<sup>7</sup>The packing fraction, i.e. effective thickness for  $^{15}\text{ND}_3$  material, was not known *a priori*. See Section 7.5 for details.

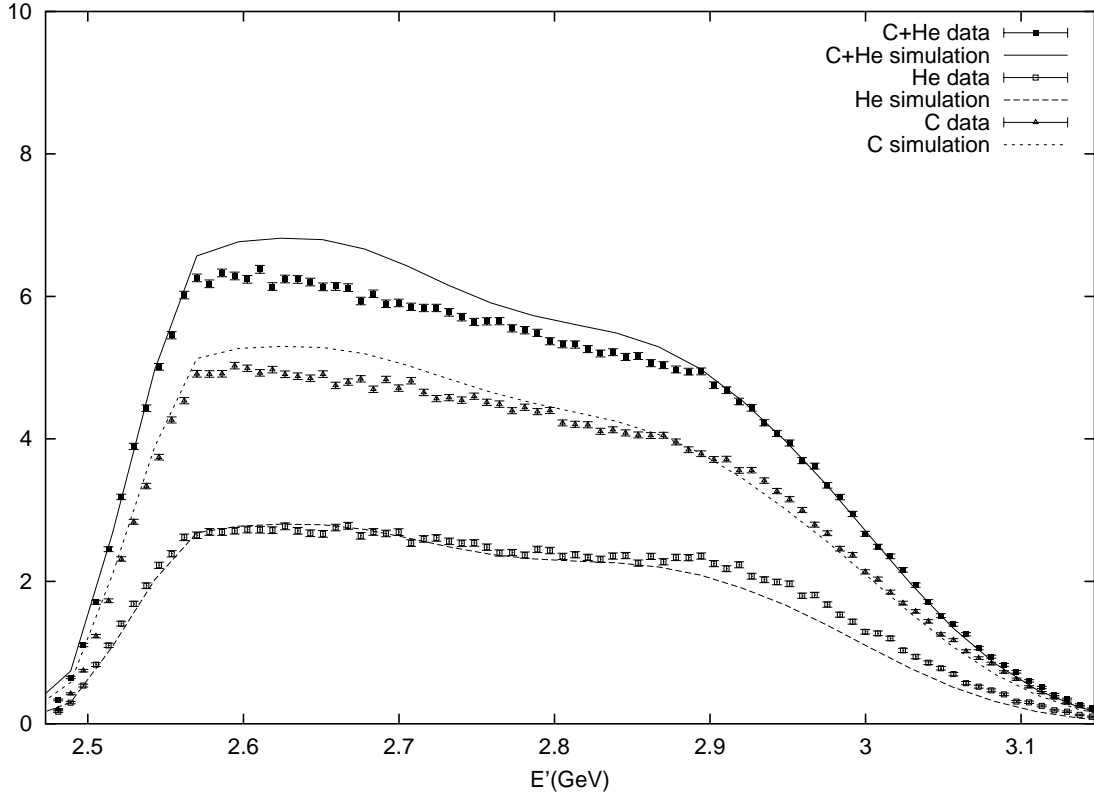


Figure 6.7: Comparison between single-arm data and simulation results.

## 6.5 Coincidence Monte Carlo simulations

Coincidence Monte Carlo simulations played an important role in the data analysis of experiment E93-026. It was used for such major tasks as cut optimization (see Section 7.2), dilution factor calculation (see Section 7.6), radiative corrections on  $A_{ed}^V$  (see Section 7.7.1), and a number of minor tasks. The simulation software was based on program MCEEP by Paul Ulmer. The original code was augmented to adequately treat the effects of the target magnetic field. In addition, the code was extended with interpolations of Arenhövel's calculations of cross-sections and asymmetries.

### **6.5.1 Basics of MCEEP**

The program allows a user to choose one of the three options: elastic scattering, bound final state or unrestricted continuum. For the bound state case the ejectile momentum is calculated from the bound state missing mass specified in the input file, whereas for the continuum case it is randomly sampled and the missing mass is calculated on an event-by-event basis.

#### **Sampled quantities**

The program samples the experimental acceptance uniformly, using calculated cross-sections as weighting factors when simulating realistic physical spectra. In a most general case (continuum scattering) an event is generated by “throwing” seven random quantities: the in-plane and out-of plane angles and momenta for the electron and the hadron, and the energy of the bremsstrahlung photon, radiated either before or after the main interaction depending on the “coin toss”.

For the bound final state, the hadron momentum is calculated from other quantities. For elastic scattering, only electron angles are sampled, and all other quantities are calculated.

#### **HMS spectrometer model**

Simulation of event detection in the HMS consisted of two major parts: forward tracking of the incident particle through the target magnetic field and HMS magnets

and reconstruction of the successful event. To account for the effect of the beam rastering, the vertex coordinates were randomly sampled within the raster spot.

The standard (i.e. without the target field and beam raster corrections) part of the algorithm consisted of the following basic steps:

- 1) projecting a particle to the magnet aperture, assuming motion along a straight line;

- 2) checking the coordinates of the particle versus the aperture of the magnet; if they fall outside the actual dimensions of the magnet aperture then the particle is labeled as stopped, and the algorithm proceeds to the next iteration;

- 3) tracking the particle forward in the magnetic field of the spectrometer magnet using COSY Infinity coefficients.

These steps are repeated for each of the 4 HMS magnets. Finally, if the particle does not stop in one of the magnets, the same approach is used to find which detectors (assumed to be 100% efficient) are fired in the HMS detector hut, and the 4 focal plane quantities are determined.

The reconstruction algorithm essentially repeats that of the data analysis code (see Subsection 6.3.1).

## **Cross sections**

The cross sections are calculated assuming plane wave impulse approximation (PWIA), i.e. the virtual photon is absorbed by one off-shell nucleon which (as well as the

incident electron) can be described by a plane wave. Under these conditions the  $(e, e'N)$  cross section can be factorized as follows [2]:

$$\frac{d\sigma}{d\epsilon_f d\Omega_e d\epsilon_N d\Omega_N} = K \sigma_{eN} S(E_m, \vec{p}_m), \quad (6.22)$$

where  $K$  is a kinematic factor,  $\sigma_{eN}$  is the elementary off-shell electron-nucleon scattering cross-section and  $S(E_m, \vec{p}_m)$  is the spectral function which represents the probability of finding a nucleon with initial momentum  $\vec{p}_m$  and binding energy  $E_m$  within the nucleus. The elementary cross-section  $\sigma_{eN}$  is calculated using the ‘‘cc1’’ prescription of de Forest [68]:

$$\sigma_{eN} = \sigma_{Mott} \left[ \frac{Q^4}{q^4} W_C + \left( \tan^2 \theta / 2 - \frac{Q^2}{q^2} \right) W_T - \frac{Q^2}{q^2} \left( \tan^2 \theta / 2 - \frac{Q^2}{q^2} \right)^{1/2} W_I \cos \phi + \left( \tan^2 \theta / 2 - \frac{Q^2}{q^2 \cos^2 \phi} \right) W_S \right] \quad (6.23)$$

$$W_C = \frac{1}{4\bar{E}E'} \left[ (\bar{E} + E')^2 \left( F_1^2 + \frac{\bar{q}_\mu^2}{4M^2} \kappa^2 F_2^2 \right) - q^2 (F_1 + \kappa F_2)^2 \right] \quad (6.24)$$

$$W_T = \frac{\bar{q}_\mu^2}{2\bar{E}E'} (F_1 + \kappa F_2)^2 \quad (6.25)$$

$$W_S = \frac{p'^2 \sin^2 \gamma}{\bar{E}E'} \left( F_1^2 + \frac{\bar{q}_\mu^2}{4M^2} \kappa^2 F_2^2 \right) \quad (6.26)$$

$$W_I = -\frac{p'^2 \sin^2 \gamma}{\bar{E}E'} (\bar{E} - E') \left( F_1^2 + \frac{\bar{q}_\mu^2}{4M^2} \kappa^2 F_2^2 \right), \quad (6.27)$$

where  $\bar{E}$  and  $E'$  are the initial (off-shell) and final energies of the struck nucleon,  $p'$  is the momentum of the struck nucleon,  $\gamma$  is the angle between  $\vec{p}'$  and  $\vec{q}$ ,  $\bar{q}_\mu$  is the four-momentum transfer corrected for off-shell effects, and  $F_1$  and  $F_2$  are Dirac and Pauli form factors.

## Spectral functions

The MCEEP has many built-in spectral functions. Additionally, the modular structure of MCEEP allows various spectral functions representing different models of the nuclei to be easily incorporated into the program through external files.

The simulations for  ${}^4\text{He}$  used a parametrization for t+p breakup channel using Urbana potential [69] (MCEEP option 32). The nitrogen spectral function was approximated by that of  ${}^{16}\text{O}$  for  $1p^{1/2}$ ,  $1p^{3/2}$  and  $1s^{1/2}$  shells (MCEEP options 40, 41 and 42). The spectral function for aluminum was a custom parametrization based on quasielastic data. Finally, copper and nickel were approximated by the carbon spectral function provided by I. Sick.

## Radiative effects

The MCEEP has options for simulating internal and external radiation and ionization energy loss. Radiative effects are only taken into account for electrons <sup>8</sup> by sampling bremsstrahlung photon energy. The peaking approximation is used, i.e. the photon is emitted either along the incident electron momentum or along the

---

<sup>8</sup>Those of hadrons are negligible due to their high mass.

scattered electron momentum. The details of the implementation of the radiative effects can be found in [70].

## 6.5.2 Customization of MCEEP

### Normalization factors

In order to account for physical mechanisms beyond PWIA, the PWIA cross sections were corrected by normalization factors given by a product of nuclear transparency and the nucleon correlation factor (see Table 6.7). Details on normalization factors can be found in [40].

Table 6.7: Nuclear normalization factors

$^2H$	$^4He$	$^{15}N$	$Al$	$Cu$	$Ni$
1.0	0.85	0.55	0.50	0.50	0.50

**Target magnetic field.** The original code of MCEEP was modified in order to account for the curvature of the charged particle tracks by the target magnetic field. The electron arm reconstruction branch of the Monte Carlo used the same Fortran code as the HMS reconstruction in event analyzer. Transporting protons through the magnetic field is in all respects analogous. Obviously, neutrons, being uncharged particles, do not need any special treatment.

**Neutron detector.** The neutron detector was modeled in MCEEP as a set of detector layers, each layer characterized by its own efficiency. These efficiencies

were calculated following the procedure by Madey *et al.* [71]. The probability of firing the  $n$ -th plane of the neutron detector was calculated based on individual plane efficiencies (see Table 6.8).

Table 6.8: Modeled neutron detection efficiencies by detector plane

1	2	3	4	5	6
0.095	0.095	0.154	0.143	0.116	0.116

The finite timing resolution for the neutron detector was simulated by Gaussian smearing of the hit position.

**Arenhövel’s calculations.** Even though MCEEP is capable of calculating polarization observables, for a precision measurement of  $G_E^n$  one needs to use full calculations including the effects of the meson exchange currents, isobar configurations and other relevant physical processes. Additionally, it is desirable to have accurate calculations for the deuteron scattering cross section as well to minimize the uncertainty in the dilution factors. Such calculations were provided by H. Arenhövel on a kinematical grid <sup>9</sup> shown in Table 6.9. The values of cross sections and asymmetries between the grid points were obtained by spline interpolation.

The  $D(e, e'N)$  scattering cross-section was radiated by multiplying by a radiative correction factor calculated from other materials. The  $A_{ed}^V$  was calculated for each event and written out to the output ntuple, thus simplifying the procedure of experimental acceptance averaging.

---

<sup>9</sup>Note that the grid in  $\theta_{np}^{cm}$  has two step sizes. The step size is  $2.5^\circ$  in the quasi-elastic region ( $0^\circ - 30^\circ$  and  $150^\circ - 180^\circ$ ) and  $5^\circ$  elsewhere.

Table 6.9: Kinematical grid for  $D(e, e'n)$  cross section

variable	range	step size
$E'$ (MeV)	2660 – 3140	15
$\theta_e$	$16^\circ - 20^\circ$	$0.4^\circ$
$\theta_{np}^{cm}$	$0^\circ - 360^\circ$	$2.5^\circ - 5^\circ$

**Pion production contamination** In order to study the contamination of the measured asymmetry by pion production events ( $\gamma^* + p \rightarrow n + \pi^+$  and  $\gamma^* + n \rightarrow n + \pi^0$ ) a simulation program EPIPROD was embedded into MCEEP through an interface sub-routine `qf_pion_production`

The program EPIPROD was originally designed by T.M. Payerle based on an earlier program by R.W. Lourie and then was rewritten and extended by J.J. Kelly. It can calculate various quantities for the electroproduction of pseudoscalar mesons for both recoil polarization and polarized target reactions. The cross sections and other observables are calculated from helicity amplitudes, which in their turn can be calculated using one of the following options:

1. a semi-realistic isobar plus Born model
2. SAID model
3. interpolation of external multipole amplitudes.

The pion events were sampled according to the PWIA cross-sections. The momentum distributions of the struck nuclei was the same as for the quasifree case. The size of the pion-production contamination of the quasifree yield was found to

be small (less than 0.5%).

### 6.5.3 Output and results

MCEEP can output its results both in histogram files and ntuples, which can be converted into a PAW-compatible [72] format. The contents of the output ntuple are described in the Table 6.10

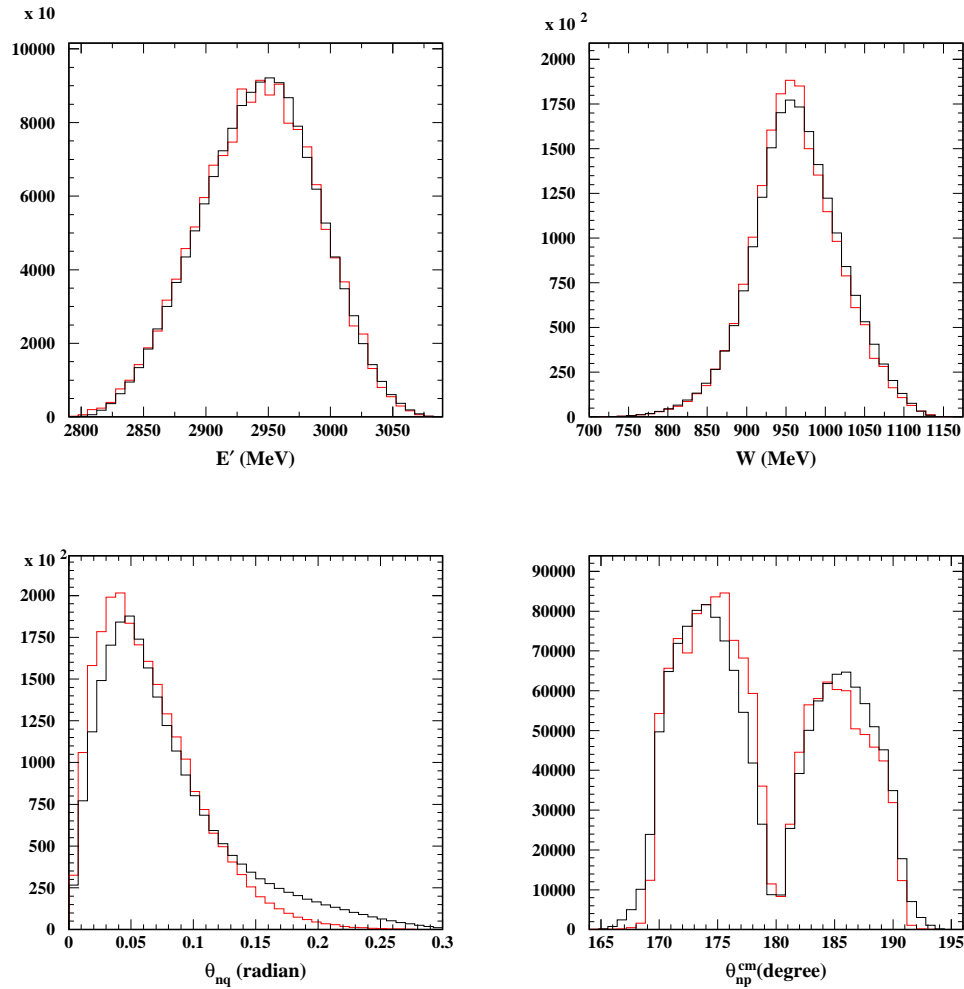
Table 6.10: MCEEP's output ntuple

variable name	description
PF_E_I	scattered electron energy $E'$
PF_P_I	in-plane angle of the knocked out hadron
TSCAT	scattering angle
N_coin	neutron detector flag (neutron detector fired if 1, not fired otherwise)
H_coin	HMS flag
thetanpcm	angle between the nucleons in the center-of-mass frame, $\theta_{np}^{cm}$
thetapqs	angle between the nucleon momentum and the momentum transfer, $\theta_{pq}$
AedV_f	observed asymmetry $A_{ed}^V$
aedv_vtx	vertex $A_{ed}^V$
radflag	radiation flag: 0 – no radiation, 1 – pre-radiation, 2 – post-radiation

A review of Monte Carlo spectra in 4 kinematic variables in comparison with data is given on the Fig. 6.8. The agreement for  $W$  and  $E'$  is excellent. For the  $\theta_{nq}$  spectrum there is a disagreement in the tail region. This is exactly what one should expect based on MCEEP's PWIA calculations, since large  $\theta_{nq}$  corresponds to large

transverse missing momentum, i.e. strong final state interactions and many-body current effects. The simulated and measured spectra for  $\theta_{np}^{cm}$  agree reasonably well.

Figure 6.8: Coincidence Monte Carlo (red) compared to data (black). The events are subject to standard neutron cuts (see Section 7.2).



# Chapter 7

## Data analysis

This chapter deals with the details of the experimental data analysis. The chapter starts with a description of the data replay process. Then we discuss cuts and inputs (target and beam polarizations) used in asymmetry calculation. Then we proceed to packing fraction and dilution factor calculations. The last two sections of the chapter discuss various corrections applied to the calculated asymmetry and the  $G_E^n$  extraction procedure.

### 7.1 Data replay

Data replay reconstructs particle tracks and event kinematics from TDC and ADC signals stored in the CODA format. This task is handled by the event analyzer described in the previous chapter. Since the entire experimental data set consists of hundreds of runs, the replay was done in parallel on an autonomous computer system called Batch Farm. The submission and control of analysis jobs was conducted by a Tcl/Tk script package “BatchMan” (for “Batch Manager”).

The initial stage of data replay involves two steps: selection of runs to be analyzed and preparation of input for the event analyzer (detector calibrations).

### 7.1.1 Runs selection

Along with data taken under normal running conditions with the polarized target, other data were taken in the experiment for different purposes (tests of experimental hardware, calibration data, beam polarization measurements etc.). Also, some of the production data were damaged because of various problems experienced during the data taking. These runs must be excluded from the analysis process. A more detailed list of excluded runs is given below:

- non- $^{15}\text{ND}_3$  targets (carbon, empty, hole)
- Møller runs
- checkup runs
- DAQ crash during the run
- serious hardware problems (magnet quenches, persistent HV trips etc.)
- unstable helium level in the target nose
- sudden loss of target polarization
- wrong position of the HMS collimator.

## 7.1.2 Detector calibrations

Raw data files contain information about particle tracks in the form of ADC and TDC signals of detector hits. In order to reconstruct the tracks and calculate physical quantities of interest, one needs to match the timing of individual detectors, supply conversion constants between ADCs and energy deposited in a detector etc., i.e. to perform detector calibrations.

### HMS calibrations

HMS calibrations consist of timing calibrations of hodoscopes, generating time-to-distance maps for the drift chambers, and determining gains of each block of the lead glass calorimeter. Since the HMS is a standard piece of equipment of TJNAF Hall C, these calibrations are a well-established procedure, the details of which can be found elsewhere [56].

### Neutron detector timing calibrations

Signals from PMT of detector scintillators arrive at the counting room with a delay of a few tens or even hundreds of nanoseconds. Due to unequal cable lengths, intrinsic transit times and high voltages, these delays generally differ between right and left PMTs. For a precise calculation of hit positions and meantime associated with a track it is necessary to apply time offset corrections to the meantime and TDC difference of a hit. These offsets are calculated by fitting the corresponding spectra of individual detectors. The offset is then given by the peak position. After

the calibration is completed, offset parameters are written to text files which are later read in by the analyzer. The quality of the calibration can be checked by plotting TDC difference and meantime spectra for individual detectors and making sure that they are centered around zero.

### **Neutron detector energy calibration**

Energy calibrations of the neutron detector were performed using cosmic data. Cosmic rays are dominated by high energy muons, for which the energy deposited in a given amount of material is well known [40] (e.g 22 MeV for 10 cm scintillators). Thus the position of the cosmic peak provides the desired conversion constant between the ADC channels and energy.

### **7.1.3 Replay procedure**

The replay of large amounts of data was performed using the Jefferson Lab computing facility (Batch Farm). The Batch Farm consists of 175 Linux CPUs. A user can submit a job to the Batch Farm by means of a *command file* which contains basic information about the command to be executed, input files and relevant parameters.

An interface between the Batch Farm and a user was provided by a Tcl/Tk package “BatchMan” , custom designed for experiment E93-026. It allows a user to observe the status of submitted jobs, kill undesired jobs, restart failed jobs and submit new jobs.

When a list of runs is submitted for analysis, BatchMan creates a command

file for each run and submits it to the Batch Farm. The command file contains a reference to the `batch_job` script which copies analysis setup and the first segment of the raw data <sup>1</sup> to the local Batch Farm computer and launches the analysis job. While a data segment is being analyzed, the next one is copied to the local disk drive in a background process. Upon completion of the analysis job the `batch_job` script copies the results to BatchMan output directories.

## 7.2 Cut optimization

For the purpose of  $G_E^n$  extraction we only need quasielastic  $\vec{d}(\vec{e}, e'n)$  events. Coincidence ntuples produced by the event analyzer contain all events that fired an HMS trigger and were successfully processed by DAQ (including inelastic, accidental background and proton events). Therefore, one needs to select desired events by applying cuts. One cut is obvious: if we are interested in neutron events, we need to look at events with the neutron PID (PID codes 11, 12, 13, 14 and 15). The other cuts are determined by figure-of-merit considerations and the quality of Monte-Carlo model in a given kinematic region.

The figure-of-merit is affected by kinematic cuts through the dilution factor: cuts emphasizing the quasielastic region improve the dilution factor and thus reduce the error magnification factor. At the same time, these cuts inevitably reduce the number of good events, too, and thus increase the statistical error itself. The op-

---

<sup>1</sup>Due to size limitations on the tape servers raw data files are split into 2 Gb segments. The number of segment files per run varied from 1 to 4 for E93-026.

timum can be determined with the use of Monte Carlo simulations. The results of simulations are shown in Figure 7.1. The figure shows figure of merit as a function of kinematic variables for several distinct sets of cuts. The figure of merit can be defined as the experimental time required for achieving given accuracy, and for fixed  $P_B$  and  $P_T$  it is proportional to  $f\sqrt{R}$ , where  $f$  is the dilution factor and  $R$  is the event rate.

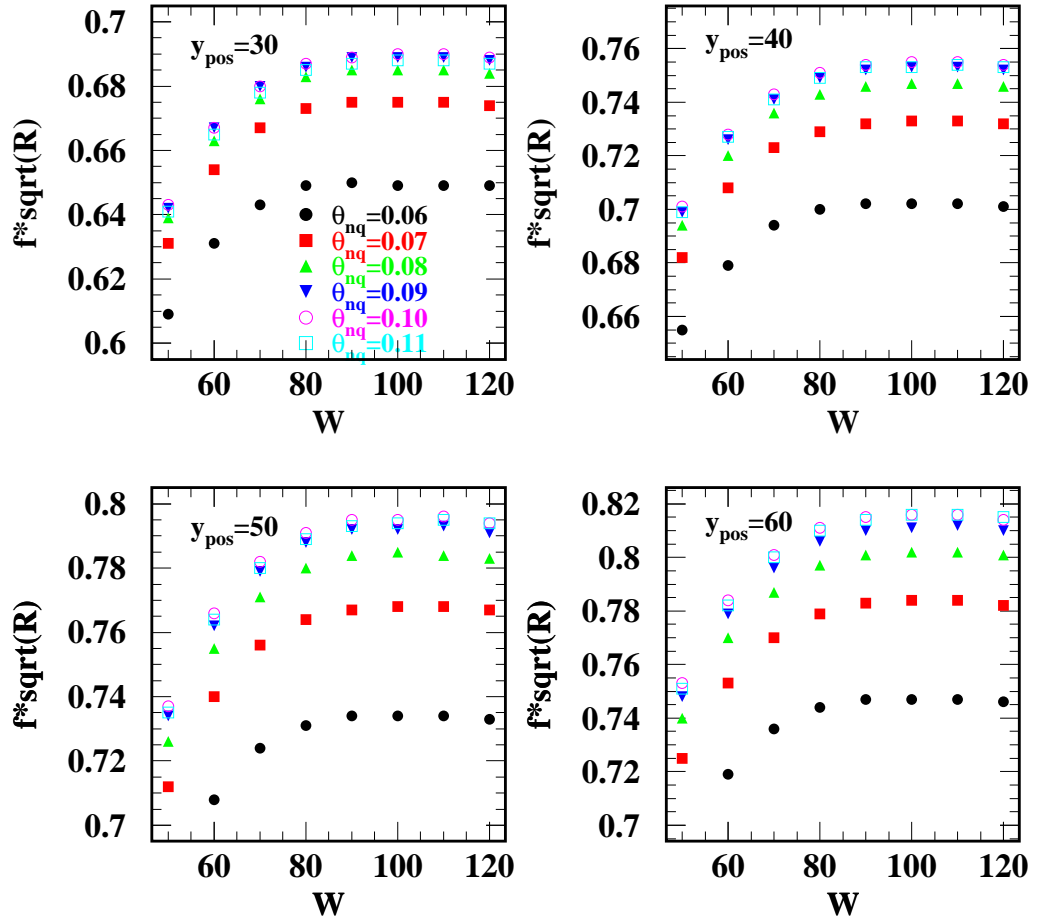


Figure 7.1: Figure of merit for different kinematic cuts. Note that  $W$  (MeV) here is not the invariant mass, but rather  $W_0$ , the width of the cut on the invariant mass:  $|W - 939| < W_0$ .

Table 7.1:  $\vec{d}(\vec{e}, e'n)$  cuts. Here  $y_{pos}$  is the horizontal position of the neutron track at the reference plane (plane 3 of the neutron detector),  $E_{track}$  is the energy deposited in the neutron detector,  $\Delta t$  is coincidence time,  $Z_{BEAM}$  is the coordinate of the vertex along the beam direction (zero corresponds to the center of the target cell) and  $M_N = 939$  MeV is the nucleon mass.

cut	suppressed events
$N_{photoelectrons} > 2$	pions in the HMS
$ W - M_N  < 70$ MeV	inelastics ( $\Delta$ electroproduction)
$E' > 2829$ MeV	same as above
$ y_{pos}  < 40$ cm	heavy nuclei (broad Fermi distribution)
$\theta_{pq} < 0.08$ rad	high missing momentum
$-3 < \Delta t < 5$ ns	accidentals
$E_{track} > 12$ MeV	low-energy noise in the neutron detector
$ Z_{BEAM}  < 3.2$ cm	events reconstructed outside the target cell
$\theta_e > 0.26$ rad	events reconstructed outside spectrometer acceptance

As one can see, the figure-of-merit (FOM) generally favors wide-open cuts rather than tight ones: it increases monotonically with the width of the  $W$  cut, the widest  $y_{pos}$  cuts also give highest FOM, and finally, the three wide  $\theta_{nq}$  cuts all lie higher than the tight  $\theta_{nq}$  cuts. However, in all cases the dependence is fairly flat which allows us a certain freedom of choice. This freedom was used to pick cuts emphasizing the kinematic region where Monte Carlo works best. Some events do not have an adequate model in Monte Carlo (e.g. pions in HMS, background etc.). The cuts for reduction of these events were developed using qualitative reasoning and a trial-and-error approach. A complete set of cuts used in the analysis is given in Table 7.1.

## 7.3 Target polarization

The target DAQ permits online monitoring of the target polarization. The prompt availability of the results comes at the expense of the accuracy of the measurement. The quality of online target polarizations is sufficient for data-taking purposes, but the actual physical calculations are more demanding.

Therefore, upon the completion of the experiment a full offline analysis of NMR signals was performed, including reevaluation of baselines, refitting the NMR signals and reanalysis of TE measurements.

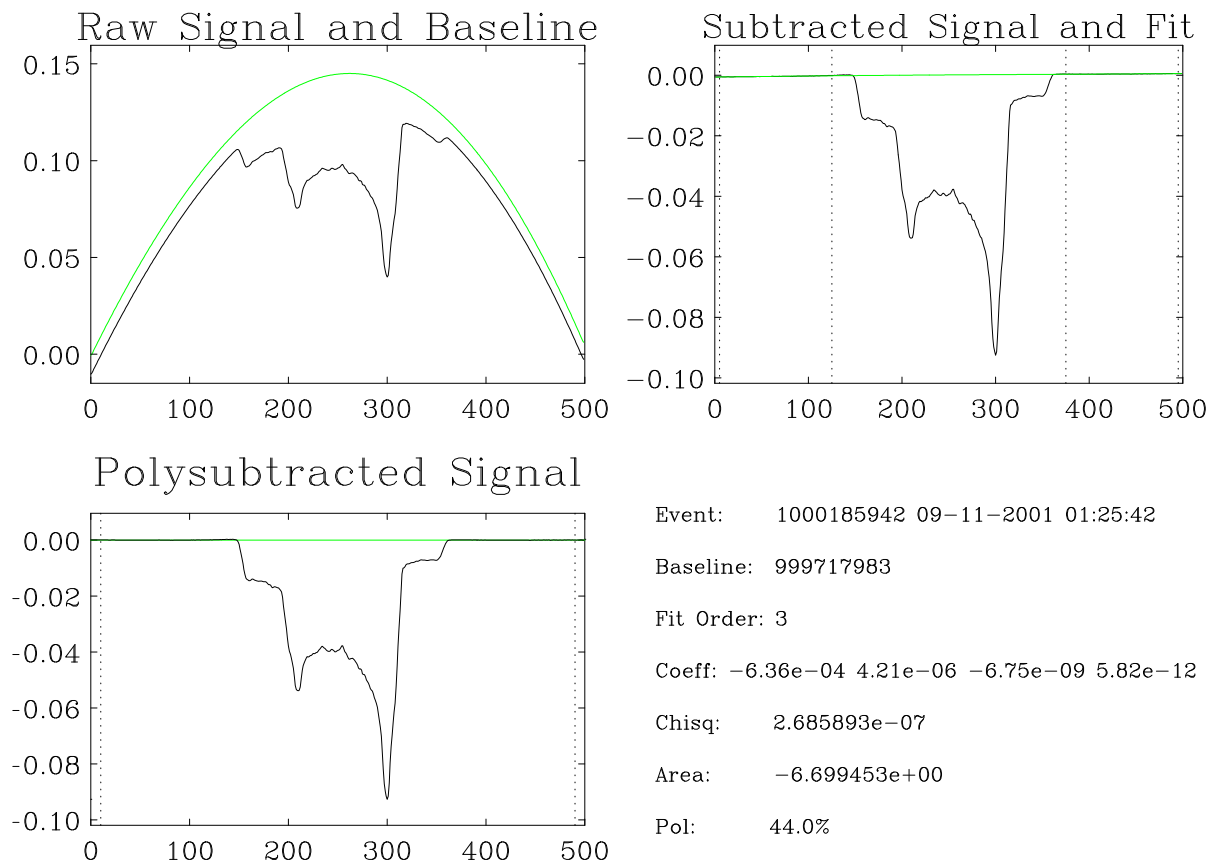
### 7.3.1 Baseline subtraction

A baseline is the response of the NMR circuit in the absence of target polarization. Baseline measurements (normally taken after each anneal) were performed by changing the target magnetic field such that the NMR signal of the deuteron was pushed outside the frequency sweep range. Baselines and NMR signals were stored separately in Labview binary files so that in case of a noisy or corrupt baseline a different one could be associated with a given set of NMR signals.

The presence of the polarization signal introduces a slight distortion of the NMR circuit response. Additionally, temperature fluctuations and beam disturbance can also affect the shape of the NMR signal. Therefore, baseline subtraction is followed by a fit of the quadratic polynomial to the “wings” of the subtracted

signal with subsequent subtraction<sup>2</sup>. The analyzed NMR signal on different stages of the offline analysis is shown in Figure 7.2. Note that the second and the third plots are almost identical, which is due to the fact that the wings are normally very small and the constant pedestal subtraction suffices in most cases.

Figure 7.2: NMR signal on different stages of the offline analysis.



# Normalized TE Constants

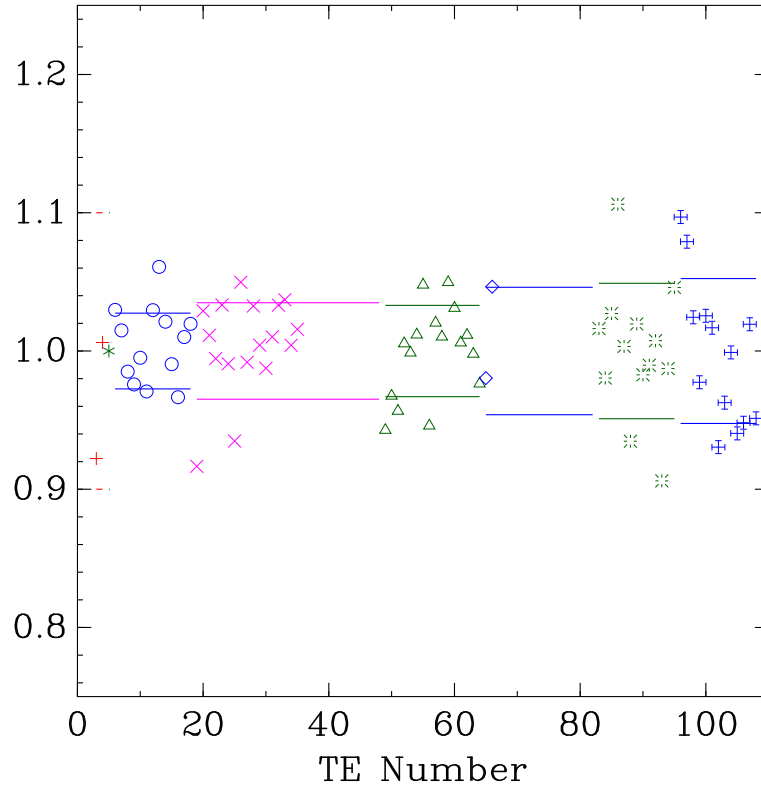


Figure 7.3: TE calibration constants for various groups. The  $\pm\sigma$  for the groups are shown with horizontal solid lines. The symbols are: plus – stick 1 top, asterisk – stick 1 bottom, circle – stick 2 top, x – stick 2 bottom, triangle – stick 3 top, diamond – stick 3 bottom, puff – stick 4 top, cross-hair – stick 4 bottom.

## 7.3.2 TE constants

If a material is allowed to thermalize, the spin temperature becomes equal to the actual (“lattice”) temperature. Under these conditions the target polarization is completely determined by the magnetic field, temperature and the magnetic moment of the deuteron and can be calculated analytically (See Eq. A.2). The area under

---

<sup>2</sup>In practice, this is done in two steps: first a constant pedestal is subtracted from the signal and then one fits the residual wings with a quadratic polynomial. This approach permits to improve the quality of the fit.

Table 7.2: Target polarization uncertainties.

stick 3 top	3.30%
stick 3 bottom	4.61%
stick 4 top	4.90%
stick 4 bottom	5.24%

the NMR signal measured in thermal equilibrium (a *TE constant*) thus provides the calibration constant for the NMR measurement.

Since the target polarization in thermal equilibrium is hundreds of times smaller than the typical polarization during production running, performing TE calibrations is a challenging task. All 110 TE measurements taken during E-93026 were carefully examined. Excluding unacceptable measurements (noisy signals, non-thermalized material, etc.) resulted in the total of 2095 good signals with from 12 to 36 signals in one TE measurement. Good signals were averaged for each material. These group averages were used in the actual target polarization calculations.

The uncertainty on target polarization was estimated by scatter of TE constants (see Table 7.2). The TE constants normalized to group averages are shown in Figure 7.3.

## 7.4 Beam polarization

The beam polarization was measured in a series of Møller runs. Individual measurements were combined into groups defined by changes in the half-wave plate positions. It has been assumed that the variation of the beam polarization values with time

was linear, and thus the values of beam polarization for runs between Møller measurements were obtained by linear fits. The details of individual measurements are given in Appendix A.2

### 7.4.1 Hall A current leakage

The Jefferson Lab accelerator provides the electron beam with (generally) different energies and/or polarizations to three experimental Halls. This is achieved either by using one laser for all three Halls or using one laser per each Hall. For the  $Q^2 = 1.0$  (GeV/c)<sup>2</sup> data, the latter was the case.

When running on three different lasers, it is possible for the current of other halls to leak into Hall C slits. Since Hall B was run in a high-polarization, low-current mode, the leakage from that Hall was of no concern. The case was the opposite with the Hall A (high current, low polarization), resulting in a sizable admixture of low-polarized Hall A beam in the Hall C beam.

The leakage was measured in a procedure that involved measuring the beam current with:

- A. C slit open, C laser off, A laser on
- B. C slit closed
- C. C slit open, both A and C lasers on.

The HMS scaler was used as a luminosity monitor. The leakage is given by

$$I_{leakage} = \frac{A - B}{C - B},$$

where A, B, C is the HMS scaler rate for each of the three steps.

The Hall A current leakage was normally measured every shift (i.e. every 8 hours). After a short bad period (with leakages up to 9%) the leakage was kept within 2%. Since the Hall A polarization is of the same sign and about half size of that of the Hall C, the resulting correction is less than 1%. Taking into consideration other dominant errors and the statistical accuracy of the experiment, it has been decided to neglect this correction. Instead, a 1% uncertainty was added to the beam polarization error.

## 7.4.2 Results

The results of the Møller measurements and their parameterizations using straight line fits is given in Figure 7.4. The global average of the beam polarization was found to be  $71.8 \pm 2.4\%$

A breakdown of the total beam polarization error by source is given in Table 7.3. The error is dominated by scatter in beam polarization values.

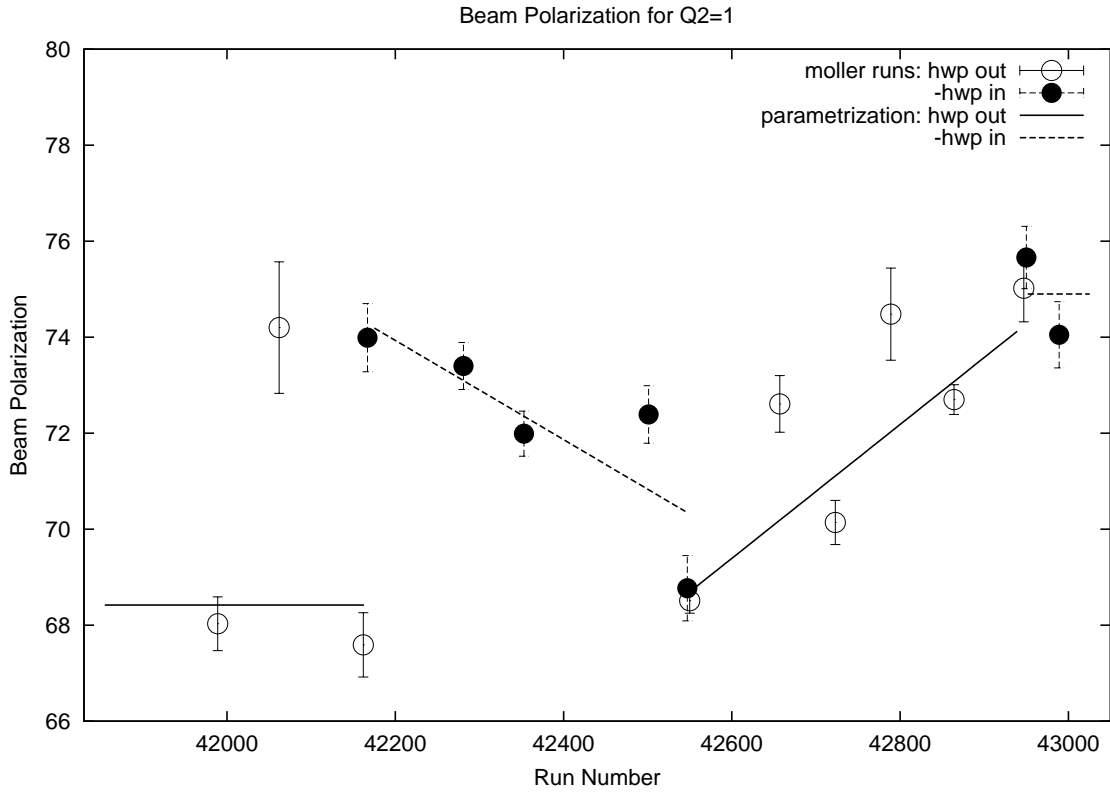


Figure 7.4: Results of Møller measurements and their parameterizations.

Table 7.3: Beam polarization error.

Source	Relative error(%)
Møller statistics	1.20
Monte Carlo statistics	0.70
Systematics	0.47
Hall A current leakage	1.00
Scatter of measurements	2.82
Total	3.33

## 7.5 Packing fraction

The packing fraction of the polarized target is the ratio of the volumes (or thicknesses, if the distribution of materials over the target face is uniform) of polarized material and cryogenic helium inside the target cup as seen by the beam. This quantity determines dilution of the measured asymmetry by unpolarized helium inside the target, which together with contributions from other material determines the overall dilution factor  $f$ .

### 7.5.1 Method of determination

Unlike other target materials, the thickness of internal helium cannot be measured directly, since the frozen ammonia has the form of small beads and does not fill up the volume of the target cell uniformly. Further, the packing fraction of a target changes during the data acquisition due to material leakage, target anneals, changes in the beam-target alignment etc. Therefore, one obtains the packing fraction using the observed event rates. One can simulate inclusive event rates for targets with different packing fractions with the inclusive simulation program described in the previous chapter, and then extract the actual packing fraction by comparing the results of the simulations with the measured rates.

The inclusive event rate from a target material is essentially the product of the cross section and luminosity integrated over the experimental acceptance. The total rate is the sum of rates from all target layers. Since for each layer the rate is

approximately proportional to the thickness of the layer <sup>3</sup>, the relation between the total inclusive rate and the packing fraction is approximately linear:

$$p.f. = \text{offset} + \text{rate} \times \text{slope}. \quad (7.1)$$

Hence, one needs to perform simulations for two values of packing fraction in order to determine the offset and slope of Equation 7.1. It is convenient to choose the two reference values of the packing fraction to be 40% and 60%. Additionally, to avoid a systematic uncertainty related to absolute normalization we normalize  $ND_3$  rate by carbon rate. The packing fraction is obtained by linear interpolation:

$$p.f. = \frac{(r - r_{40})40 + (r_{60} - r)60}{r_{60} - r_{40}}\%, \quad (7.2)$$

where  $r$  is the ratio of the  $^{15}ND_3$  rate to carbon rate as measured in data, and  $r_{40}$  and  $r_{60}$  are model ratios assuming packing fraction of 40% and 60%, correspondingly.

## 7.5.2 Event selection

The data were cut on the number of Čerenkov photoelectrons (`hcer_npe > 2`) for pion rejection. Both Monte Carlo and data were also cut on the scattered electron energy ( $2880 < E' < 3100$  MeV) to emphasize the quasielastic kinematics. The stick 3 data were additionally cut on the horizontal raster position (`beamx > 0`) to

---

<sup>3</sup>There are nonlinear effects due to thickness-dependent radiative energy losses. However, they are of the order of 1% and can be neglected here.

eliminate the contribution from the side wall (see Section 7.6.3 for details).

### 7.5.3 Procedure and results

The calculation of the packing fraction was performed separately for two different target inserts with different material loads (“stick 3” and “stick 4”). For each insert, the entire set of  $^{15}\text{ND}_3$  and carbon data was replayed in the single-arm mode of the analyzer (with the neutron detector side ignored). Then a cut processor counted events that survived the imposed cuts <sup>4</sup>. The inclusive event rate was normalized by dead-time corrected charge (provided by `syncfilter` output), HMS trigger efficiency, and the tracking efficiency. Finally, the  $^{15}\text{ND}_3$ /carbon rate ratio was formed.

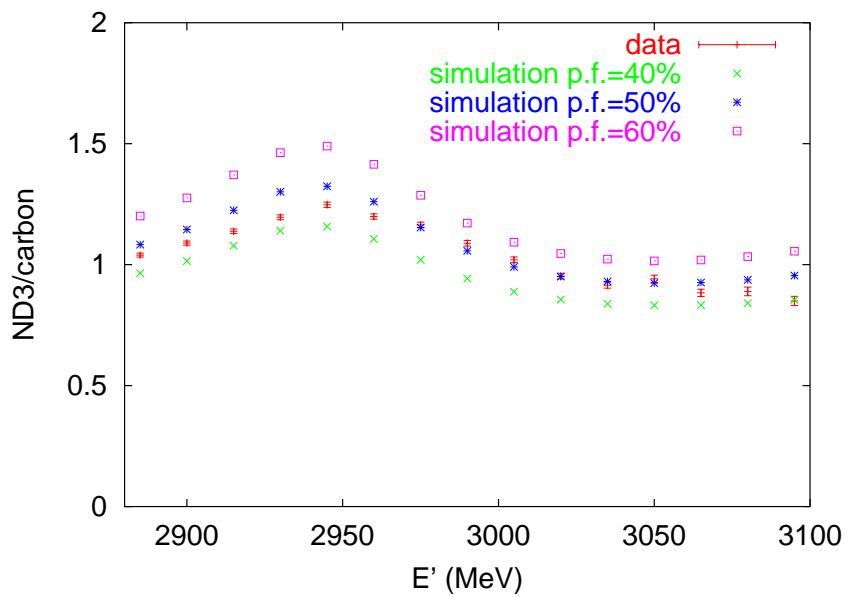
The data ratio was compared to simulated <sup>5</sup> ratios with packing fraction of 40% and 60%. The ratios are shown in Figure 7.5(a). As one can see, the shapes of the  $E'$ -dependences for different packing fractions are practically identical, which confirms that nonlinear effects due to radiation are small.

The packing fraction was extracted from these ratios using Equation 7.2. The scatter of the packing fraction values over  $E'$  characterizes systematic and statistical accuracy of the measurement. The statistically weighted average over all  $E'$  bins was taken as the final result for the packing fraction. The systematic error contained two contributions (added in quadrature): scatter in  $E'$  bins (3.2% for both sticks)

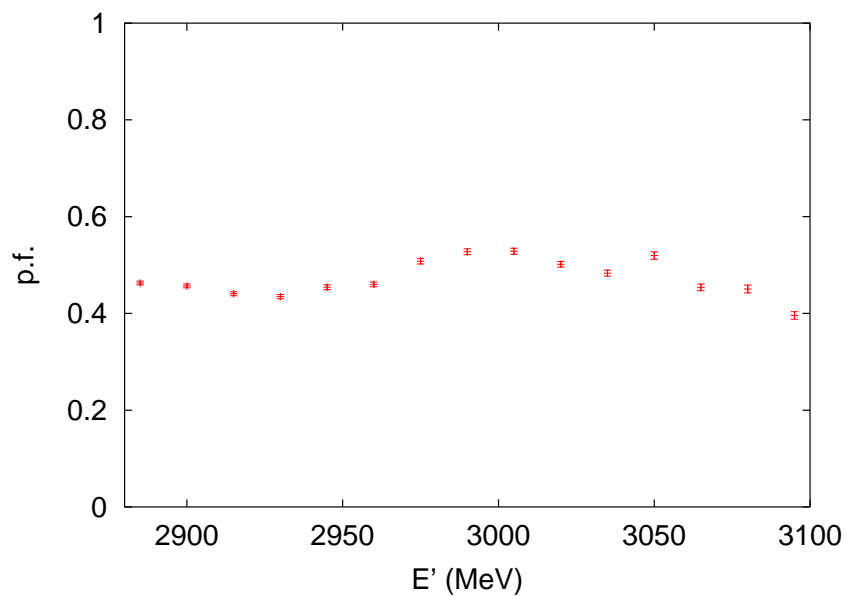
---

<sup>4</sup>The events were counted in 32 uniform  $E'$  bins, covering range from 2660 MeV to 3140 MeV, to study the systematic errors.

<sup>5</sup>see Section 6.4 for a description of the simulation package



(a)



(b)

Figure 7.5: Packing fraction for stick 4: (a) ratio of carbon rate to that for the  $^{15}\text{ND}_3$  target, (b) packing fraction.

and scatter in inclusive rates over time (0.85% for stick 3 and 2.6% for stick 4). The final results are:  $51.2 \pm 3.3\%$  for stick 3 and  $46.7 \pm 4.1\%$  for stick 4.

## 7.6 Dilution factor

Since the target material is not pure deuterium, in addition to deuteron events one has contributions from unpolarized scattering on ammonia's nitrogen, liquid helium in the target cell, NMR coils, target windows etc. As a result, the asymmetry is "washed out" or "diluted". The asymmetry for scattering from all materials ( $\epsilon_{all}$ ) is:

$$\epsilon_{all} = \frac{N_{all}^+ - N_{all}^-}{N_{all}^- + N_{all}^+}, \quad (7.3)$$

The total rate  $N_{all}$  is the sum of rates of polarized and unpolarized contributions,  $N_p$  and  $N_u$ . If we take into account that the unpolarized rates does not depend on the electron helicity, the expression (7.3) can be transformed to:

$$\begin{aligned} \epsilon_{all} &= \frac{N_p^+ + N_u^+ - N_p^- - N_u^-}{N_p^+ + N_u^- + N_p^- + N_u^+} = \frac{N_p^+ - N_p^-}{N_p^+ + N_p^- + N_u^+ + N_u^-} \\ &= \frac{N_p^+ - N_p^-}{N_p^+ + N_p^-} \cdot \frac{N_p^+ + N_p^-}{N_p^+ + N_p^- + N_u^+ + N_u^-} = \epsilon \frac{N_p}{N_{all}} = \epsilon f, \end{aligned} \quad (7.4)$$

where  $\epsilon$  is the asymmetry of scattering from the pure material and the dilution factor  $f$  is the ratio of the polarized yield to the total yield.

For the purposes of our experiment it is convenient to express polarized and unpolarized yields of the Equation 7.4 via rates of specific target materials. The only polarized material in the target is the deuterium<sup>6</sup> and thus  $N_p = N_d$ . The unpolarized yield can be broken into contributions from the ammonia nitrogen  $N_N$ , helium inside the target cell  $N_{He}^{int}$ , helium outside the target cell  $N_{He}^{ext}$  and target walls  $N_W$ . Since the relative ratio of ammonia and internal helium yields is determined by the packing fraction, we can rewrite (7.4) as:

$$f = \frac{N_d p.f.}{N_{He}^{ext} + N_d p.f. + N_N p.f. + N_{He}^{int}(1 - p.f.)}, \quad (7.5)$$

where the yields for materials inside the target cell are calculated assuming that they fill up its entire volume.

Since yields are determined by kinematic-dependent scattering cross sections, the dilution factor is also a function of kinematic variables. The coincidence event rate measured in the experiment cannot be separated into contributions from specific materials. Therefore, for a proper determination of the experimental dilution factor one needs to run Monte Carlo simulations.

The simulations were performed using the customized version of MCEEP (see Section 6.5). The simulation was run separately for sticks 3 and 4 because of their different material thicknesses (due to different packing fractions and different orientation with respect to the beam).

---

<sup>6</sup>In reality, the nitrogen also carries some polarization, but it does not contribute to the neutron asymmetry. See page 49.

### 7.6.1 Pion contamination

In electron-nucleon scattering the virtual photon may excite the nucleon to a resonant state which then decays into a nucleon with an emission of a pion. Such reaction mechanism is known as pion electroproduction. For a coincidence electron-neutron measurement only two such reactions are of interest:  $\gamma^* + p \rightarrow n + \pi^+$  and  $\gamma^* + n \rightarrow n + \pi^0$ .

Most of events coming from these reaction are suppressed by kinematic cuts, in particular by the cut on the invariant mass,  $|W - M_N| < 70$  MeV, where  $M_N = 939$  MeV is the nucleon mass. However, some of pion events because of Fermi broadening may have kinematics similar to that of the quasielastic scattering and thus contaminate the measured asymmetry. It has been experimentally verified that these events do not carry any statistically significant asymmetry. Therefore, their contribution (found to be 0.44%) can be included into the dilution factor calculation.

### 7.6.2 Misorientation of the 4K shield

In the beginning of the data analysis it has been found that the distribution of the events along the beam direction has strange shoulders outside the target cup (see Figure 7.6) at  $|Z_{BEAM}| > 3$  cm . It has been established that these shoulders were due to a misorientation of the 4K shield (which surrounds the tailpiece with the target insert) such that for some raster positions the beam was coming not through the thin window in the shield, but rather through the shield itself, thus transversing

an order of magnitude larger amount of material than expected (see Figure 7.7). A Geant 4 simulation (see below for details) showed that the effective thickness of the 4K shield was 1.822 mm for stick 3 and 1.874 mm for stick 4. The majority of these events were eliminated by the standard analysis cut  $|Z_{BEAM} < 3.2 \text{ cm}|$ . The residual contribution from the 4K shield events was estimated by fitting a sum of three asymmetric Gaussians to the  $Z_{BEAM}$  spectrum (see Figure 7.6) and was found to be  $0.23\% \pm 0.05\%$ . This correction was applied to the dilution factor.

### 7.6.3 Stick 3 rotation

When stick 3 was extracted, we found that the radiation damage pattern on the material was consistent with an anomalous counter-clockwise rotation of the insert about the vertical axis. Obviously, such a rotation affects the thicknesses of the material transversed by the beam and therefore the dilution factor. In order to account for this effect, a C++ program was written based on Geant 4 libraries [52]. The program calculates average thickness of each target material in the beam's path and incorporates horizontal and vertical displacement and a rotation about the vertical axis of the target insert.

The angle of the stick rotation was determined by the 4 mm horizontal displacement of the hole target to be  $15.8^\circ$ . However, since the raster calibrations are only accurate to about 1 mm, there is a  $3.8^\circ$  uncertainty in the rotation angle.

The mutual arrangement of the beam and the rotated stick is shown in Fig-

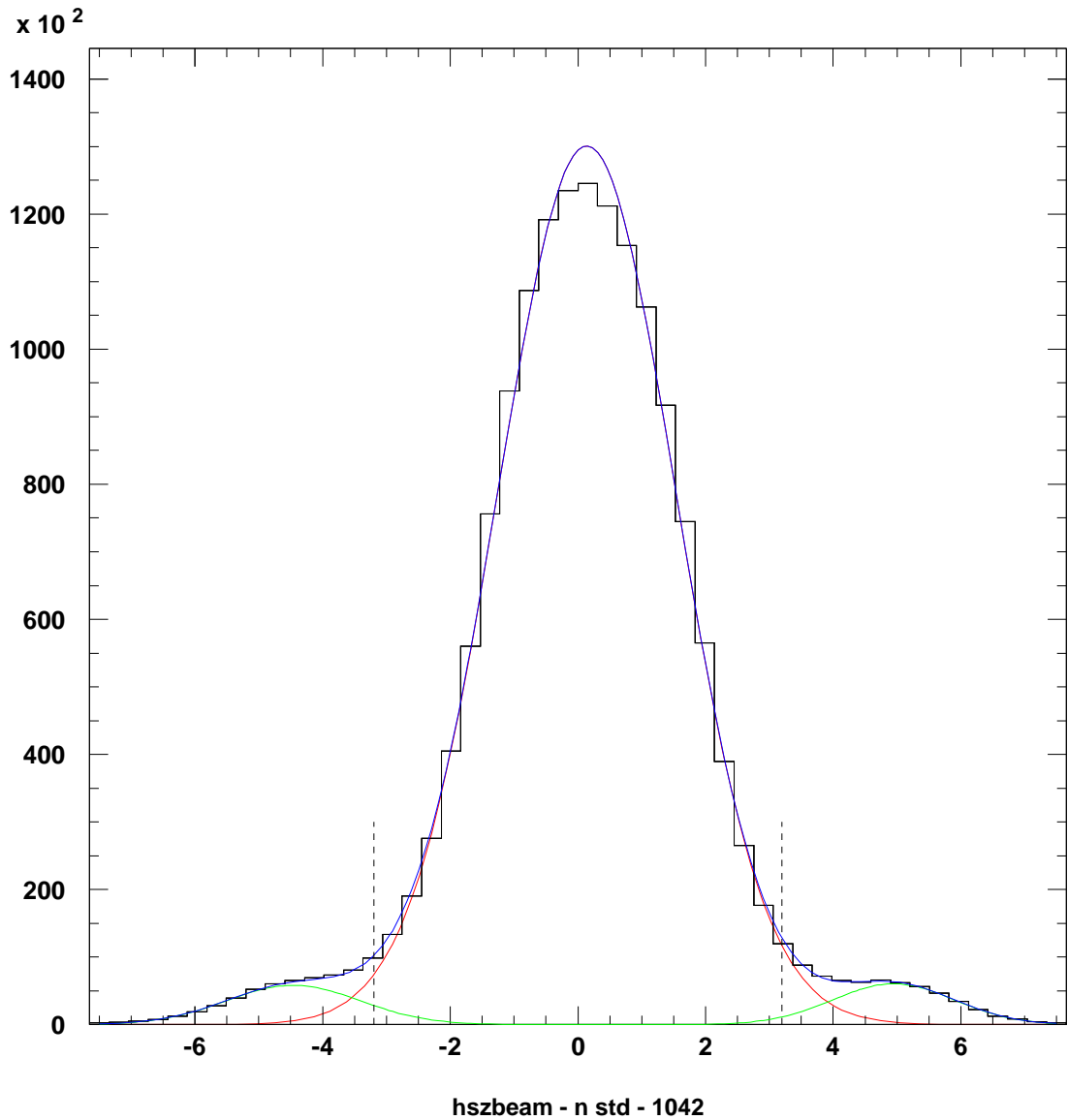


Figure 7.6: The  $Z_{BEAM}$  distribution (black) decomposed into contributions from the target cup contents (red) and upstream and downstream 4K shield windows (green). The boundaries of the standard analysis cut is shown with dash-dotted lines. See text for details.

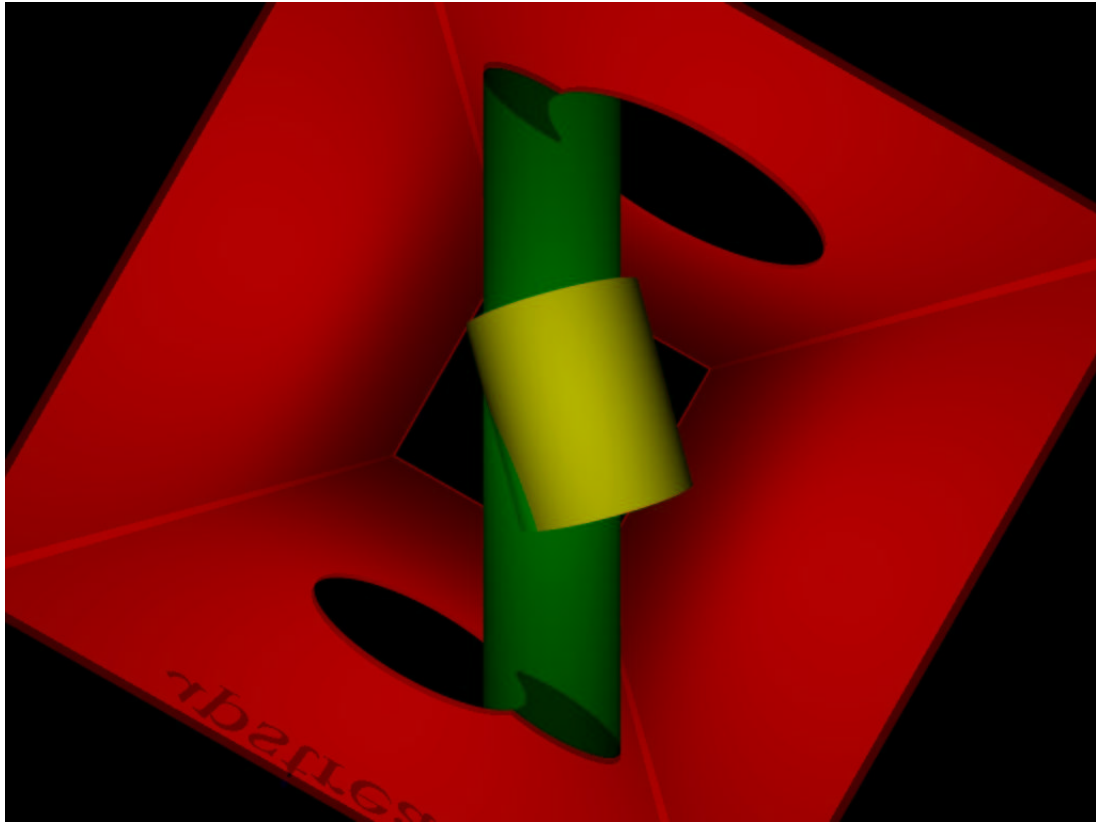


Figure 7.7: A top view of the cup (yellow) inside the 4K shield (red). The rastered beam is shown in green. The beam is entering the target on the top.

ures 7.7 and 7.8. As one can see, apart from a change in the effective thicknesses for target materials inside the cup, the stick rotation gives rise to a contribution from the cup side walls.

The simulations were run with rotation angles of  $11.94^\circ$ ,  $15.82^\circ$  and  $19.70^\circ$ . The target thicknesses obtained are summarized in Table 7.4.

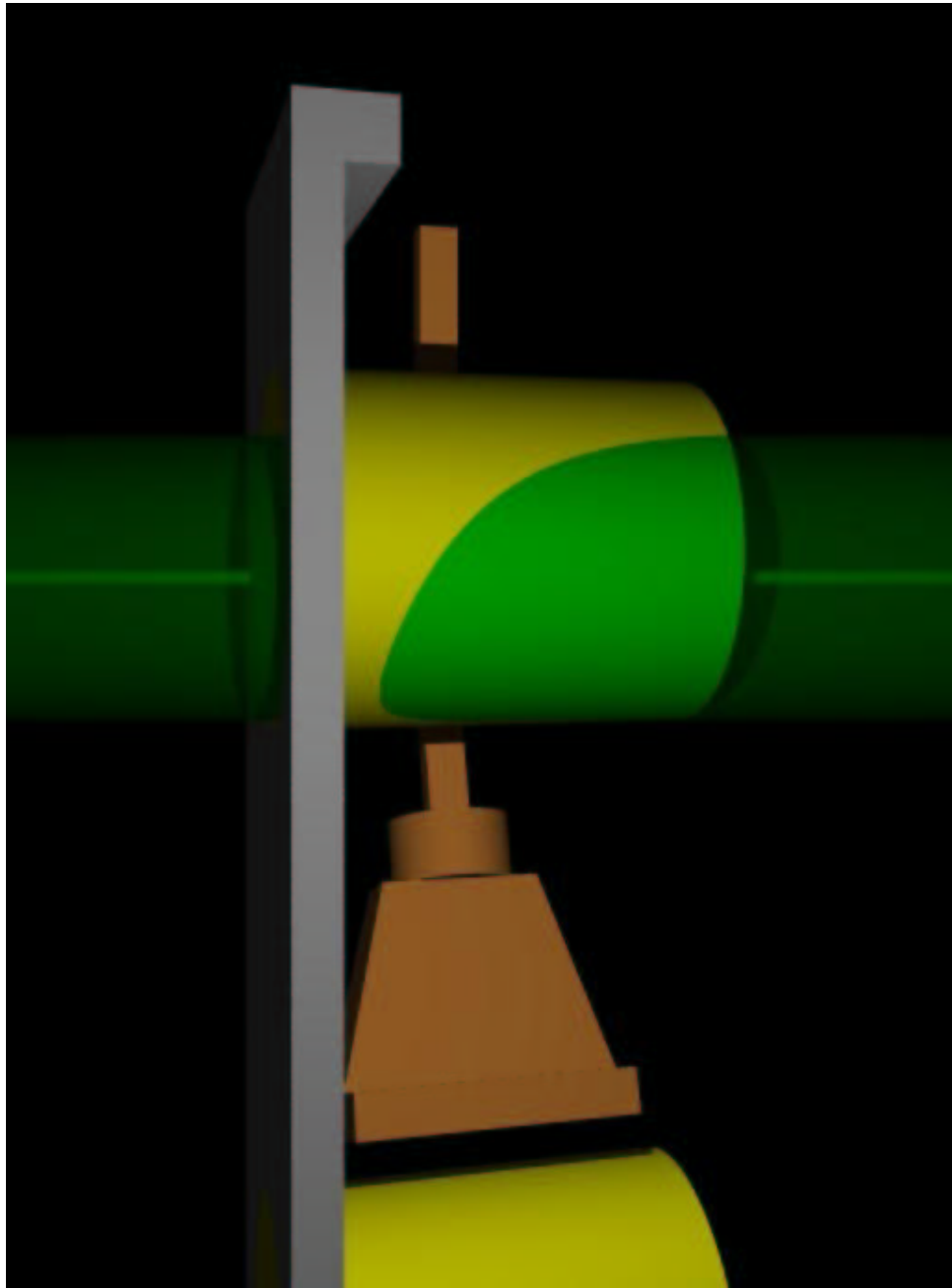


Figure 7.8: Target insert rotation.

Table 7.4: Effective thicknesses (mm) for various target materials.

Material	Stick and rotation			
	s3(0°)	s4(11.94°)	s4(15.82°)	s4(19.70°)
4K Shield	1.822	1.874	1.874	1.874
Drift Space	49.927	52.860	52.860	52.860
Tail Window	0.208	0.213	0.213	0.213
LHe	11.535	10.931	11.010	11.035
Cup Window	0.051	0.048	0.047	0.046
Cup Wall	0	0.573	0.637	0.687
Cup Contents	29.201	28.384	28.243	28.159

## 7.6.4 Results

Material thicknesses in Table 7.4 together with packing fractions (51.2% for stick 3 and 46.7% for stick 4) provide the necessary input for the MCEEP simulations. Simulation results for the nominal rotation (15.8°) of stick 3 are summarized in Table 7.5.

Table 7.5: Simulated (e,e'n) rates from various target materials for dilution factor calculation (stick 3).

Target	Thickness (cm)	Normalization factor*	Radiation length (%)	Luminosity ( $\mu A \cdot g/cm^2$ )	Rate (per 100 nC)
2H	1.581	1.0	0.38	0.04775	0.739
He	2.419	0.85	0.37	0.02058	0.215
15N	1.581	0.55	2.93	0.11937	0.183
Al	0.014	0.50	0.157	0.00754	0.009
Cu	0.01	0.50	0.70	0.00896	0.017
Ni	0.0043	0.50	0.30	0.00383	0.007
inelastics	–	–	–	–	0.005
total	–	–	5.96**	–	1.175

\* See Section 6.5.2 for definition.

\*\* Includes materials not seen by HMS (and therefore not included into the table).

Using Table 7.4 it is straightforward to obtain rates for stick 4 and for alternate

rotations of stick 3. The dilution factor of the stick 3 is 62.7% for the nominal angle and 62.8% for 11.94°, i.e. the uncertainty in the rotation angle is about 0.1% relative. For stick 4 the result is 62.6%. The uncertainty in the dilution factor was estimated by comparing the measured rates with Monte Carlo predictions and was found to be 2.6% relative. With this, for the statistically weighted dilution factor for the entire data set one has  $62.6 \pm 1.6\%$ .

## 7.7 Corrections

Before the experimental asymmetry can be used for extraction of the  $G_E^n$ , it needs to be corrected for dilution and/or contamination from unwanted background (accidental coincidences, multi-step reactions, misidentified protons), loss of events in electronics (electronics deadtime) and bias of reaction kinematics due to electron energy loss by radiation.

### 7.7.1 Radiative corrections

In the analysis of the experimental data we deal with *measured* values of the reaction kinematics. These, however, in general may differ from the actual, or *vertex* kinematic quantities. The main mechanism responsible for this difference is radiative energy loss by both incident and scattered electron.

Since the bremsstrahlung photons are not observed, one needs again to resort to simulations to estimate the effect of these energy losses and correct for

it. The MCEEP imitates the effects of internal and external radiation by sampling bremsstrahlung photons according to the bremsstrahlung spectrum. The photons are emitted along the direction of either the incident or the outgoing electron (peaking approximation). Radiative effects can be turned off by disabling the corresponding option in the input file. The value of the acceptance averaged Monte Carlo asymmetry with the radiation off is then compared with the nominal value (radiation on) and the ratio between these two gives the desired radiative correction.

This procedure was done separately for internal and external radiative effects and yielded a  $0.55 \pm 0.50\%$  correction for the internal radiation. The correction due to the external radiation was found small due to the statistical Monte Carlo uncertainty of 0.50%

### **7.7.2 Paddle inefficiency**

The particle identification algorithm was based on the hit in one of the paddle planes. The probability for a proton to produce a hit in a paddle plane (i.e. paddle efficiency) is very high, but still below 100%. A proton that did not fire a paddle was likely to be identified as a neutron. As the protons have the asymmetry of the opposite sign (compared to that of the neutrons) and have a larger quasielastic scattering cross section, even a small paddle inefficiency can result in a sizeable contamination of the neutron asymmetry.

The contribution of misidentified protons to the total measured neutron asym-

metry  $A$  can be found as:

$$\begin{aligned}
 A &= \frac{N_n^+ - N_n^- + N_p^+ - N_p^-}{N_n + N_p} = \\
 &= \frac{N_n A_n + N_p A_p}{N_n + N_p} \approx A_n + \frac{N_p}{N_n} A_p,
 \end{aligned}
 \tag{7.6}$$

where  $N_{n(p)}^{+(-)}$  is neutron (proton) yield for positive (negative) beam helicity,  $A_{n(p)}$  is the “clean” (uncontaminated) asymmetry of neutrons (protons), and we used the fact that  $N_p \ll N_n$ .

Expressing the combined inefficiency of paddle planes  $\epsilon$  through individual plane efficiencies  $\epsilon_{1,2}$  we obtain the following formula for the asymmetry contamination  $\Delta A$ :

$$\Delta A = (1 - \epsilon_1)(1 - \epsilon_2) \frac{N_p}{N_n} A_p.
 \tag{7.7}$$

The paddle plane efficiencies were calculated using 2-out-of-3 (one paddle + one bar) events in the first three detector planes and were found to be 96.0% and 98.3% for planes 1 and 2, correspondingly. The  $N_p/N_n$  ratio was extracted from our experimental data. It was found that initial proton-to-neutron ratio of 6:1 was reduced by the  $\theta_{nq} < 0.08$  cut to 1:2. Finally, the proton asymmetry  $A_p$  was also taken from our experimental data to be  $-15.2\%$ . Plugging these numbers into the Equation 7.7 we obtained the proton contamination correction of order 50 ppm, i.e. about 1% of the size of the statistical error of the measured asymmetry, and

therefore negligible.

### 7.7.3 Electronics deadtime

When the counting rates in detectors are high, the data acquisition system may start losing events. This is known as *deadtime*. The experimental deadtime can be divided into *computer* deadtime (loss of events due to the BUSY status of the DAQ) and *electronics* deadtime. The computer deadtime is taken care of by the data stream preprocessor (see Section 6.2) and thus we only need to correct for the electronics deadtime.

The loss of events in electronics occurs due to overlap of signals that have a finite time width. Since the principal trigger in the experiment was the HMS trigger, the neutron detector electronics did not contribute to the deadtime.

The HMS electronics generated HMS gates of 4 different widths: 30 ns, 60 ns, 90 ns and 120 ns. By observing the dependence of the event rate on the gate width and extrapolating it to 0 ns one can find the “ideal” HMS rate. The deadtime is then the difference between the 30 ns gate rate and this 0 ns extrapolated value.

Three randomly chosen runs were studied. Typical results are shown in Figure 7.9. The values of the correction is of the order of 15-30 ppm and thus is negligible given the statistical accuracy of the experiment.

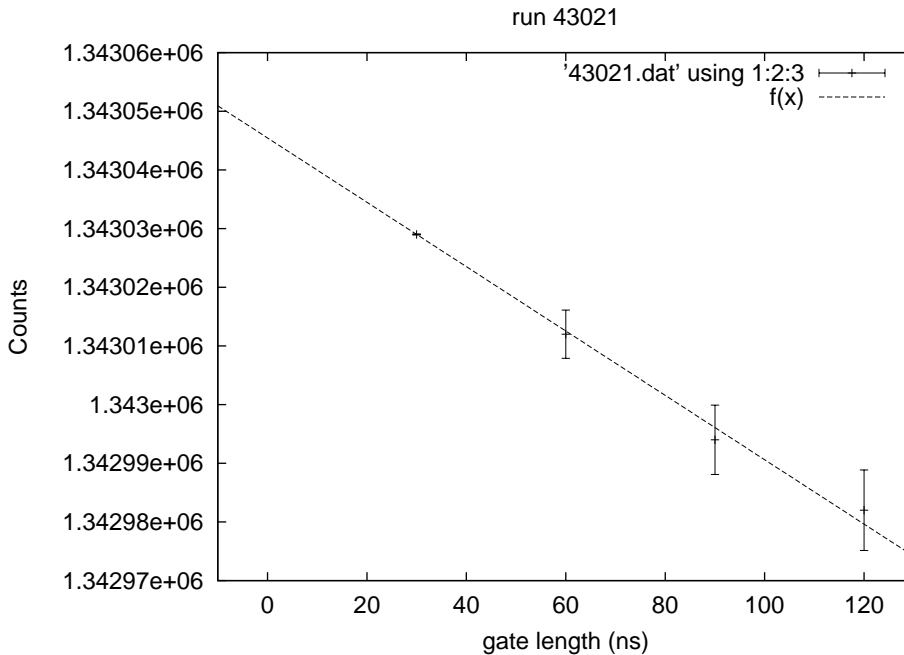


Figure 7.9: The number of HMS events as a function of the gate width (run 43021).

#### 7.7.4 Accidental background subtraction

Although most of the unwanted background is eliminated from the analyzed data by the coincidence timing cut ( $-5 \text{ ns} < \Delta t < 3 \text{ ns}$ ), some of it survives this and other cuts. As the asymmetry associated with the background may (and most likely will) differ from the neutron asymmetry, it is desirable to estimate the level of the background and correct for its effects.

It is straightforward to calculate the fraction of accidental *hits* under the coincidence peak. This can be done by examination of the hit meantime spectra (see Figure 7.10). Determination of the number of accidental *tracks* within the coincidence window requires more sophistication, because the relation between hits and tracks is very non-trivial. There are generally three possibilities. An accidental hit

can:

- form a new track
- combine with an existing track
- destroy an existing track by pushing its averages outside the cut windows.

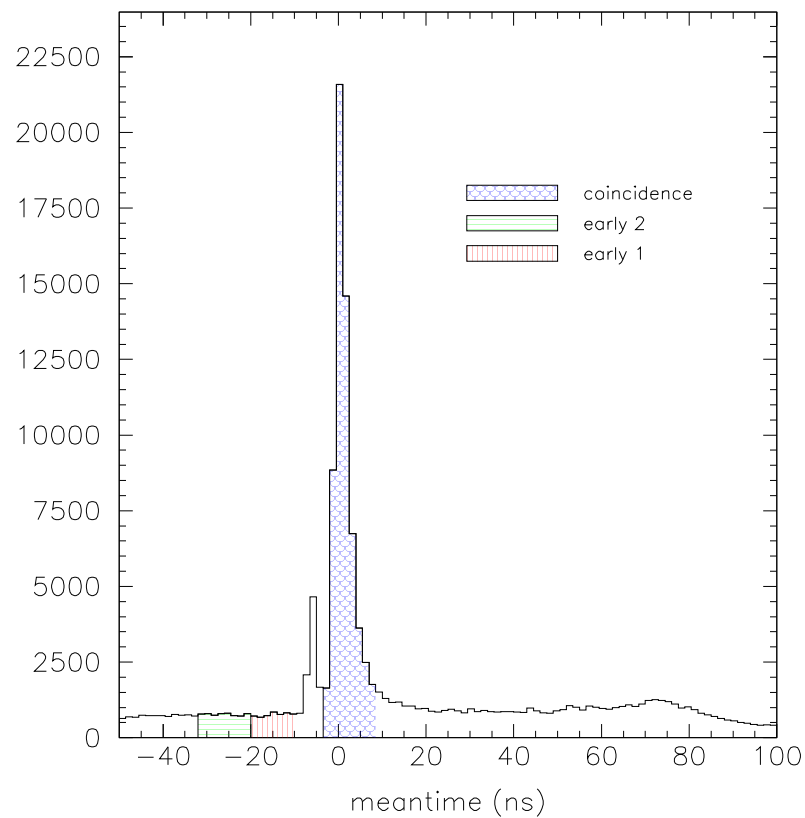


Figure 7.10: Hits meantime distribution. Note that the tail of delayed events after the coincidence peak.

It is hard to estimate the relative contributions of these mechanisms on analytic grounds. Instead, a simpler approach was adopted. It was assumed, that

the relationship between the total number of tracks and the number of accidental hits is approximately linear (for reasonably low background). Then the number of “pure” tracks (no accidentals) can be obtained by extrapolating the dependence of the track number on the level of background hits to zero background. The number of background hits was controlled by adding extra coincidence windows.

Two such windows were used, “early 1” ( $-21.5 \text{ ns} < \Delta t < -11.0 \text{ ns}$ ) and “early 2” ( $-32.0 \text{ ns} < \Delta t < -21.5 \text{ ns}$ ), both having the same width as the nominal coincidence window ( $-3 \text{ ns} < \Delta t < 7.5 \text{ ns}$ ). The results are shown in Figure 7.11. A straight line fit to the data points shows that our assumption of a linear relationship between the number of background hits and the number of resulting tracks is valid.

The relative background (defined as the ratio of background to “clean” coincidence tracks) is slightly different from the relative excess (ratio of background tracks to all tracks) plotted in Figure 7.11. The relative background averages over the entire sample of analyzed data (16 runs) are given in the Table 7.6. The global average was calculated from background in windows early1, early2 and early12 using weighting factors of 30%, 30% and 40% respectively, and was found to be  $0.51 \pm 0.23\%$ .

Table 7.6: Background study results. ”Early12” refers to tracks with both early1 and early2 windows open. The numbers are relative backgrounds (%), as defined in the text.

counts	early 1	early 2	early12	average	error
44583	0.62	0.43	0.49	0.51	0.23

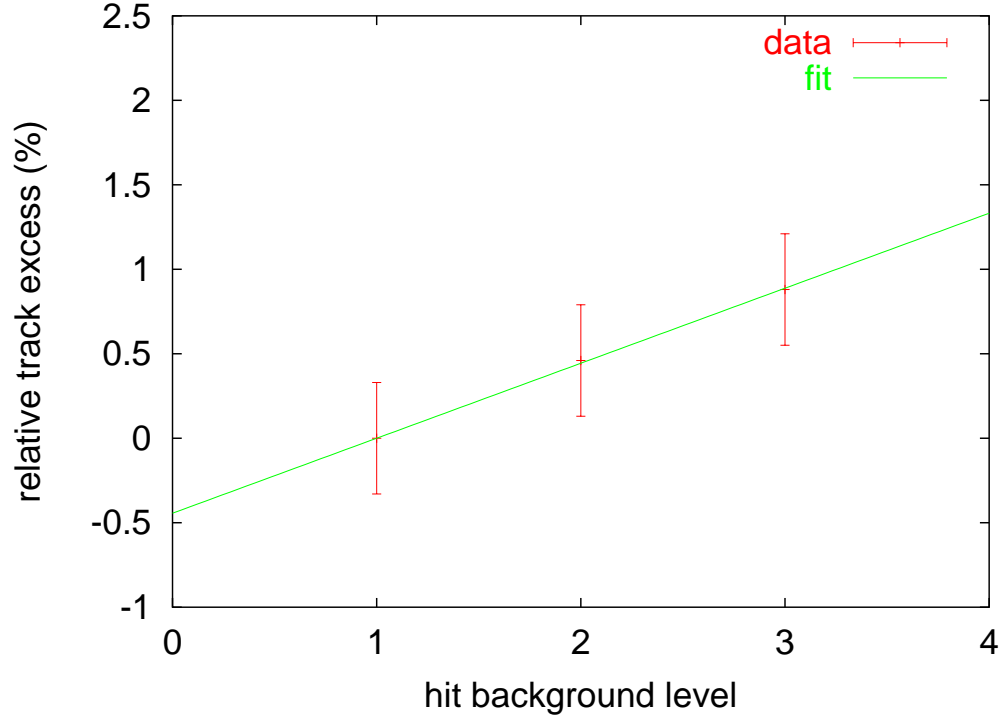


Figure 7.11: Relative track excess (i.e. relative change in the number of tracks due to additional background) versus the background level. The three points correspond to normal data (coincidence window only), one extra “early” window, and both “early” windows.

### 7.7.5 Multi-step reactions contamination

The vast majority of neutrons detected in the neutron detector come from quasielastic  $\vec{d}(\vec{e}, e'n)$  scattering in the target material. However, a small fraction of neutron events are brought up by charge exchange reactions in the lead curtain and the target material. Additionally, decay of pions generated in the lead produces photons that cannot be distinguished from neutrons. Contributions from these reaction mechanisms carry proton asymmetry, which has the opposite sign compared to the neutron one, and therefore it is important to correct for these effects.

In the analysis of E93-026 the following multi-step reactions were investigated:

- in the lead shielding
  - $d(e, e'p)$  followed by  $^{208}\text{Pb}(p, n)$
  - $d(e, e'p)$  followed by  $^{208}\text{Pb}(p, \pi^0)$  and  $\pi^0 \rightarrow \gamma\gamma$
- in the target material
  - $d(e, e'p)$  followed by  $^{15}\text{N}(p, n)$

Charge exchange in the deuteron itself is included in the theoretical calculations as a part of final state interactions and does not require a correction. Charge exchange in other target materials does contribute to the scattering asymmetry, but is negligible compared to the nitrogen.

### Charge exchange in the lead

The size of the contribution of the charge exchange in the lead was estimated using Monte Carlo simulations. For proton kinematics, actual distributions from experimental data were used. The proton energy was corrected for the energy loss suffered in the lead. The emitted neutron was generated using  $^{208}\text{Pb}(p, n)$  cross section from the charge exchange studies of the Basel  $G_M^n$  experiment [73]. Since the angular dependence of the  $^{208}\text{Pb}(p, n)$  cross section is not known, two extreme cases were considered:

- same angular dependence as free  $p - n$  scattering
- no angular dependence

The straight average of the results for the two cases was used in the simulation. The difference between the two answers (26.7%) was included in the systematic uncertainty.

For simplicity, the neutron detector in the simulations was replaced with a cube of dimensions given by the enclosure of all bar planes except the extended top of plane 3. Neutron detection efficiency  $\epsilon$  was calculated as a function of the pathlength  $x$ ,  $\epsilon = \exp(-\alpha x)$ . The constant  $\alpha$  was calculated using the KSUVAX program [71] and was found to be independent of neutron energy (within 10%) above the threshold energy of 55 MeV.

As we noted earlier, the neutrons generated by charge exchange carry the proton asymmetry, therefore the simulation used actual proton asymmetries measured in E93-026 as functions of various kinematic variables.

The resulting correction is  $-3.15\% \pm 3.01\%$ . The error is dominated by the uncertainty in the charge exchange cross-section [74].

## 7.8 Results

### 7.8.1 Extraction of $G_E^n$

The  $G_E^n$  extraction procedure is very straightforward. First, one calculates run by run asymmetries (see Figure 7.13) and their statistically weighted average. Then all relevant corrections are applied (accidental background, radiative effects, charge

exchange etc.). In parallel, one averages the theoretical asymmetry over the detector acceptance for different values of  $G_E^n$ . Finally, the  $G_E^n$  is found as the solution of the equation  $A_{exp} = A_{theor}(G_E^n)$  (see Figure 7.12).

The time evolution of neutron asymmetries is shown in Figure 7.13(a). In order to improve the statistical resolution, group averages (rather than run-by-run asymmetries) are plotted there, where the groups are defined by changes in beam and target polarizations. The scatter of individual points is purely statistical, as confirmed by Figure 7.13(b) where a  $\chi^2$  distribution for run-by-run asymmetries is plotted in comparison with the theoretical curve.

The asymmetry was also calculated for proton events. Since proton form factors are better known at our kinematics, proton asymmetries can be compared to the theoretical predictions, thus providing a check of experimental systematics. Also, we have much (roughly by a factor of six) more proton events than neutron ones, and they carry a larger asymmetry, so the statistical resolution is much better for protons. The results of the proton asymmetry study are shown in Figure 7.14. The agreement between the theoretical calculations and experimentally measured proton asymmetries is excellent.

The global average for the neutron asymmetry (corrected for beam and target polarizations only) was found to be  $4.031 \pm 0.471\%$ . After applying the dilution factor and other corrections it becomes  $6.641 \pm 0.776\%$ . The linear interpolation <sup>7</sup> between the  $A_{ed}^V$  values for  $G_E^n = 1.1 G_{Galster}$  and  $G_E^n = 1.3 G_{Galster}$  gives  $0.0423 \pm 0.00506$

---

<sup>7</sup>Higher order effects are smaller than 0.05% (relative) and thus need not be considered.

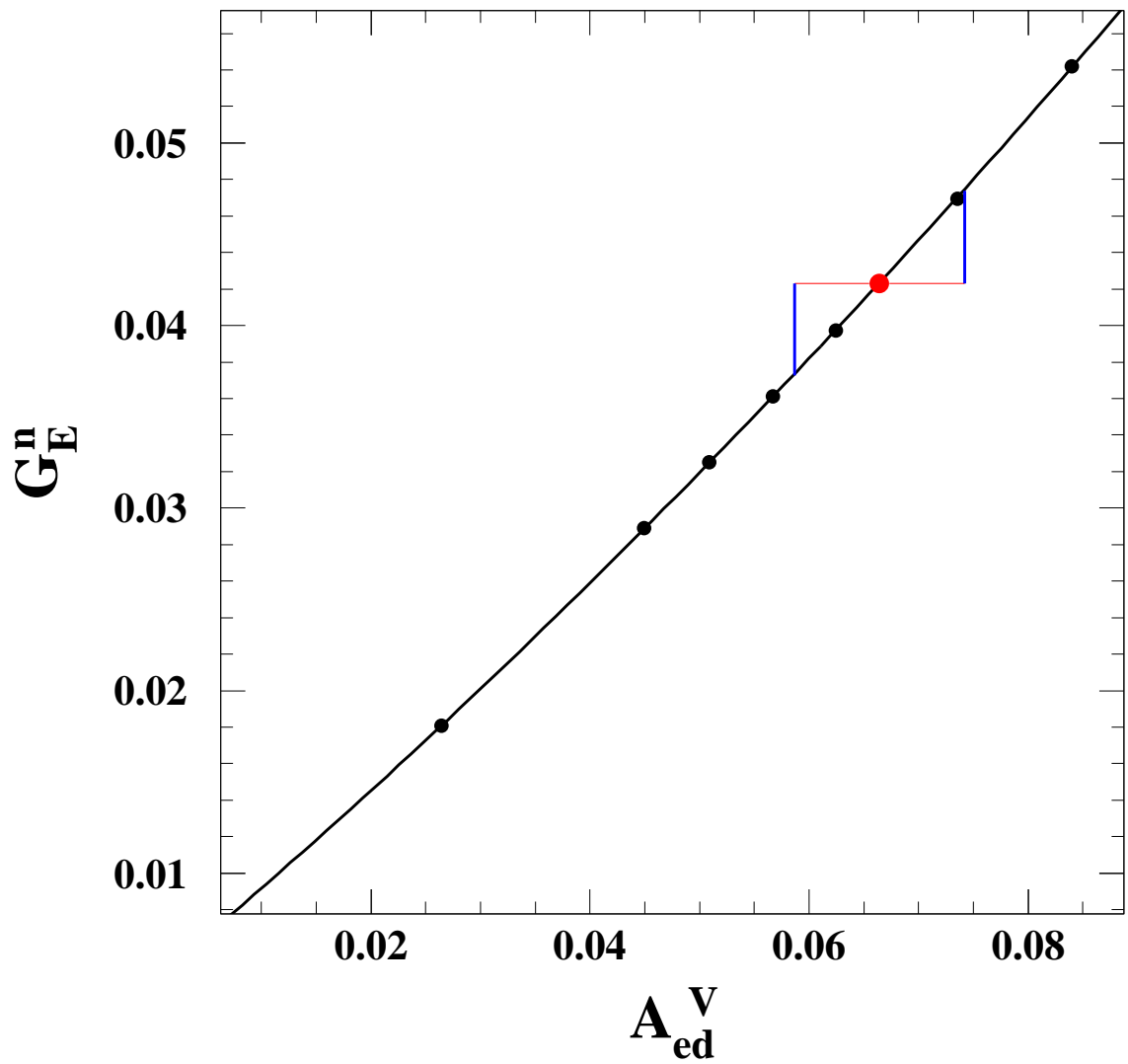
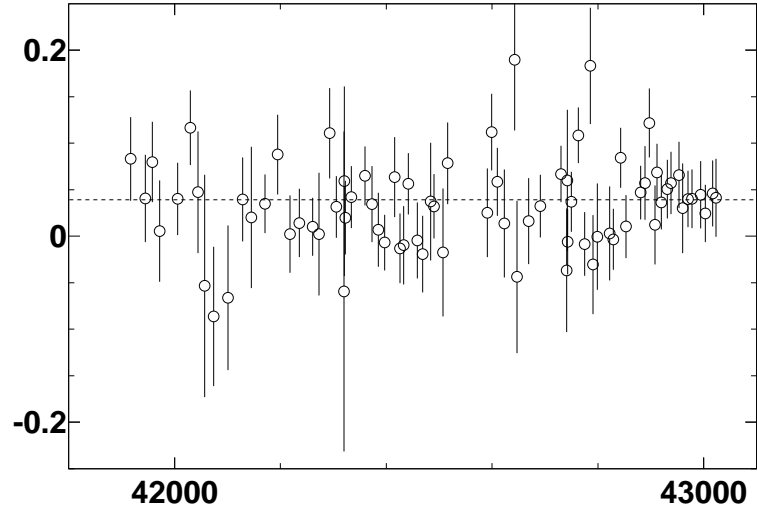
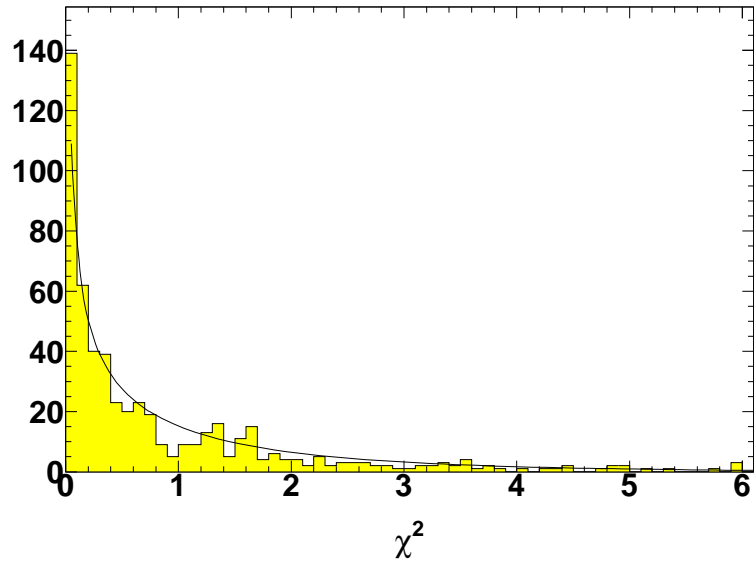


Figure 7.12: The  $G_E^n$  extraction plot. The charge form factor of the neutron is plotted as the function of the measured asymmetry. The solid line is the fit to the sampled points (black) points. The red point is the corrected experimental asymmetry ( $6.64 \pm 0.78\%$ ).



(a)



(b)

Figure 7.13: Statistical properties of neutron asymmetries: (a) neutron asymmetries  $\epsilon_i$  versus run number  $i$  (the dashed line corresponds to the global statistically weighted average), (b) distribution of  $\chi_i^2 = [(\epsilon_i - \langle\epsilon\rangle)/\Delta\epsilon_i]^2$  compared with the theoretical  $\chi^2$  distribution with one degree of freedom (solid line).

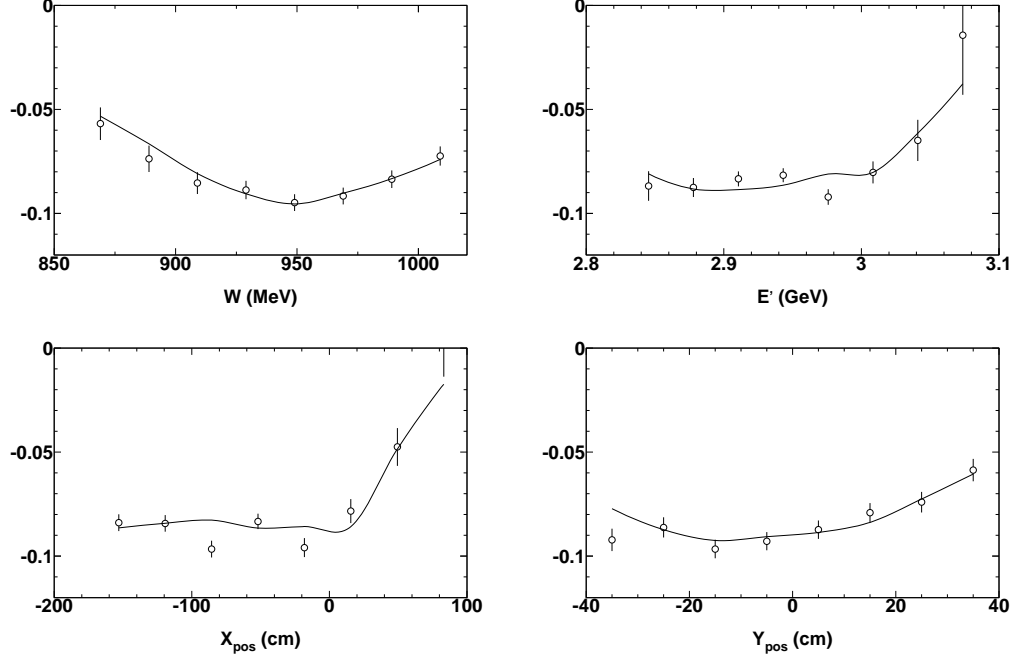


Figure 7.14: Proton asymmetries: Monte Carlo (solid line) compared to data (open circles).

for the  $G_E^n$  ( $1.172 G_{Galster}$ ). When calculating the theoretical asymmetries, the dipole parametrization for the magnetic form factor of the neutron was assumed. However, recent measurement indicate that the true value of  $G_M^n$  deviates from the dipole parametrization:  $G_M^n/G_D = 1.072 \pm 0.014$  [75]. Monte Carlo simulations with different values of  $G_M^n$  showed that its effect on the  $G_E^n$  is linear. With this, the final value for the  $G_E^n$  becomes:

$$G_E^n = 0.0454 \pm 0.0054, \quad (7.8)$$

where the uncertainty is statistical. Systematic uncertainties will be considered in the remainder of the section.

## 7.8.2 Kinematic uncertainties

The leading kinematic uncertainty is due to the horizontal position of the neutron detector. The initial comparison between  $y_{pos}$  (i.e. horizontal position of the nucleon track at the 3rd plane) spectra of the data and the Monte Carlo revealed a 4 cm discrepancy which was attributed to a bias in the survey measurement of the neutron detector angle. In order to determine the impact of this uncertainty, the data analysis was repeated with a shifted neutron detector position.

This showed that a 5 mrad shift in the neutron detector angle changes the  $A_{ed}^V$  (and therefore,  $G_E^n$ ) by 2.4%. Since a 4 cm shift in  $y_{pos}$  corresponds to a 6.4 mrad shift in the angle, the uncertainty due to the neutron detector position is 3.22%.

The next largest kinematic uncertainty is the one due to the field angle. This quantity was measured by surveyors to the accuracy of  $0.1^\circ$ , which propagates to 0.99% uncertainty in  $A_{ed}^V$ , as found by Monte Carlo simulation with a shifted target field orientation. Other kinematic uncertainties were also studied using Monte Carlo simulations and were found to have a small impact (see Table 7.7).

## 7.8.3 Other experimental uncertainties

The combined kinematic uncertainty together with other sources of the systematic error are given the Table 7.8. The largest uncertainty is the one related to the target polarization (4.6%). Other important contributions include the combined kinematic uncertainty, beam polarization error and the charge exchange uncertainty.

Table 7.7: Kinematic uncertainties.

quantity	original error	propagated error
beam energy	1.7 MeV	0.29%
spectrometer momentum	2.8 MeV	0.36%
spectrometer angle	1 mrad	0.6%
target field	0.1°	0.99%
vertical position of the nDet	4.8 mrad	0.58%
horizontal position of the nDet	6.4 mrad	3.22%
total	—	3.47%

Table 7.8: Systematic uncertainties.

quantity	relative error
target polarization	4.60%
beam polarization	3.30%
dilution factor	2.63%
charge exchange	3.01%
magnetic form factor	2.29%
total kinematic uncertainty	3.47%
radiative correction	0.50%
accidental background	0.23%
total	8.10%

Since the asymmetry depends not only on the charge form factor of the neutron, but also on the magnetic one, which is known with a limited accuracy, the  $G_M^n$  uncertainty of 2.29% must also be included. The overall error is obtained by combining all partial errors in quadrature and is found to be 8.10%. With this, the final result of the experiment becomes:

$$G_E^n(Q^2 = 1.0) = 0.0454 \pm 0.0054(stat) \pm 0.0037(sys). \quad (7.9)$$

#### 7.8.4 Reaction mechanism dependence

In order to investigate the effects of various aspects of the reaction mechanism on the extracted value of  $G_E^n$  the extraction procedure was repeated with the values of the theoretical asymmetries calculated in two simplified models: PWIA+RC (relativistic impulse approximation) and FSI+RC (the former plus final state interactions). Since we are only interested in the relative size of various nuclear corrections and since the relation between the extracted  $G_E^n$  and the model value of  $G_M^n$  is linear, the dipole parametrization was used for  $G_M^n$  for all three models.

The results of this study are presented in Table 7.9. The effects of the meson exchange currents and isobar configurations are thus small (of order of 2%), whereas the effect of the final state interactions is somewhat bigger ( $\sim 5\%$ ).

These numbers compare very favorably to analogous estimates for the unpolarized measurements, where the effects of nuclear corrections of 10 – 30% are

typical. Also, comparison with calculations for  $Q^2 = 0.5$  (10.5% difference from the full calculation for PWBA+RC and 2.4% for FSI+RC) show that these corrections become relatively less important at higher  $Q^2$ .

The impact of the choice of the  $N - N$  potential on the  $A_{ed}^V$  is negligible for quasifree kinematics [36].

Table 7.9: Reaction mechanism dependence of  $G_E^n$ . All calculations assume dipole parametrization for  $G_M^n$ .

model	$G_E^n$	impact(%)
Full	0.0423	–
PWBA + RC	0.0397	6.1
FSI + RC	0.0415	1.9

### 7.8.5 Parametrization of $G_E^n$

Traditionally,  $G_E^n$  is parametrized using the so-called Galster parametrization

$$G_{Galster} = -\frac{a\mu_n\tau}{1+b\tau}G_D, \quad (7.10)$$

with  $a = 1$ ,  $b = 5.6$ ,  $G_D = (1+Q^2/\Lambda^2)^{-2}$  and  $\Lambda = 0.71$  (GeV/c)<sup>2</sup>. This parametrization, based on low- $Q^2$  data from early 1970's [16], continues to work well even for higher  $Q^2$  data. However, the improved precision data from this experiment and the results of a recent recoil polarimetry measurement in JLab Hall C [27] now reveal a sizeable deviation from the conventional Galster fit.

We performed a fit to the world  $G_E^n$  database using the traditional Galster form (7.10). The fitting procedure yielded  $a = 0.86 \pm 0.04$  and  $b = 3.06 \pm 0.46$

with the  $\chi^2$  per degree of freedom of 0.71. The charge radius measurement [10] was included into the fitted database to constrain the slope of  $G_E^n$  at low  $Q^2$ . The comparison of the fit with the experimental data can be seen in Figure 7.15.

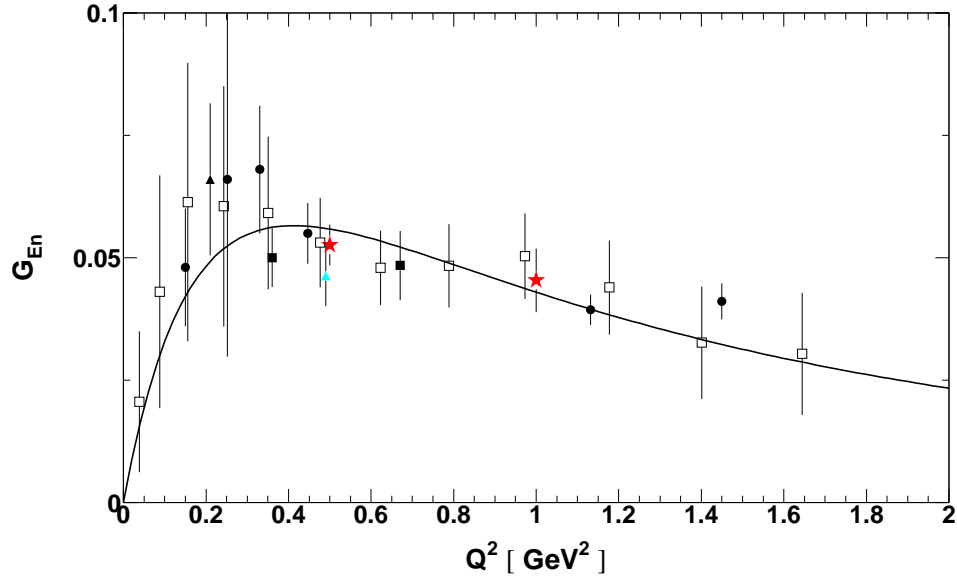


Figure 7.15: Results of the 2001 run of E93-026 (2001 run – red stars, 1998 run – cyan triangle) compared with other experimental data (see Figure 8.7 for description of the markers). The solid line is the improved Galster fit of Section 7.8.5.

# Chapter 8

## Theoretical predictions of $G_E^n$

### 8.1 Asymptotic behavior

Modern physics sees the nucleon as three valence quarks dressed with a sea of quark-antiquark pairs, interacting by means of gluon exchange. The ultimate description of the nucleon is to be given by quantum chromodynamics (QCD). At the low and intermediate momentum transfers the QCD calculations are not feasible (due to extreme nonlinearity of the interaction). At the high momentum transfers, however, the quarks behave as free particles (this feature of QCD is known as *asymptotic freedom*). Therefore, for large  $Q^2$  the running coupling constant of the strong interaction  $\alpha_s(Q^2)$  becomes small and perturbative techniques can be applied.

#### 8.1.1 Dimensional scaling laws

Certain conclusions about the asymptotic behavior of the form factors can be made without performing the actual perturbative QCD (pQCD) calculations. Consider

high energy  $e - N$  scattering. In order for the nucleon to keep its identity and remain in the ground state after the interaction (i.e. for the scattering to occur *elastically*), it is necessary that all the quarks continue to move collinearly after the virtual photon is absorbed. Therefore, the struck quark must share its momentum with the other constituents by means of gluon exchange. In the most general case of  $n$  constituents, this involves  $n - 1$  gluon exchanges. As each gluon propagator brings in a factor of  $1/Q^2$ , this means that the scattering amplitude would go like  $1/(Q^2)^{n-1}$ . Hence the Fock states involving gluons and sea quarks are suppressed compared to the leading order contribution from two gluon exchange between the three valence quarks (Figure 8.1).

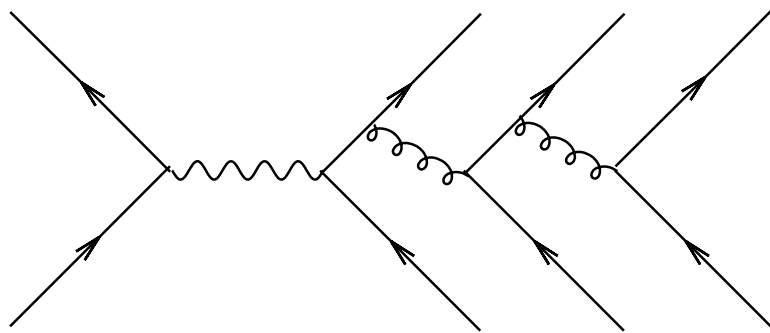


Figure 8.1: Elastic  $e - N$  scattering amplitude at high  $Q^2$ .

Since a nucleon helicity flip requires a flip of helicity of a nearly massless quark, the spin-flip amplitude (described by the Pauli form factor  $F_2$ ) is suppressed relative to the non-flip one (described by the Dirac form factor  $F_1$ ). Analyticity suggests that the suppression factor depends rather on  $Q^2$  than on  $Q$ , and a natural assumption (but not a rigorous prediction) is  $1/Q^2$ . With this, the asymptotic behavior for the

Dirac and Pauli form factors becomes [76]

$$F_1 \sim 1/Q^4, \tag{8.1}$$

$$F_2 \sim F_1/Q^2. \tag{8.2}$$

The equations 8.1 and 8.2 are known as *dimensional scaling laws*.

If one expresses  $F_1$  and  $F_2$  in terms of Sachs form factors, one arrives at the  $1/Q^4$  asymptotic dependence for both  $G_E$  and  $G_M$ .

### 8.1.2 Perturbative QCD calculations.

#### Magnetic form factors

The dimensional scaling laws only give the leading power asymptotic behavior for  $Q^2 \rightarrow \infty$ . More information (normalizations, logarithmic corrections, etc.) can be obtained by performing the actual pQCD calculations.

The perturbative approach is based on QCD factorization theorems, which allow scale separation between the short-distance and long-distance motion of the partons. The short-distance (high momentum) motion corresponds to hard (perturbative) physics, while long-distance (low momentum) motion corresponds to soft (non-perturbative) physics.

For the helicity conserving form factor of the nucleon<sup>1</sup> one has in pQCD :

$$F_1(Q^2) = \int_0^1 [dx_i] \int_0^1 [dy_i] \phi^\dagger(x_i, Q) T_H(x_i, y_i, Q) \phi(y_i, Q), \quad (8.3)$$

where  $T_H(x_i, y_i, Q)$  is the hard scattering amplitude,  $\phi(x_i, Q)$  is the minimum Fock-state wave function integrated over transverse momenta,  $x_i$  is the longitudinal momentum fraction carried by the  $i$ -th valence quark, and  $[dx_i] = dx_1 dx_2 dx_3 \delta(1 - \sum_i x_i)$ . It is straightforward to express  $T_H$  in terms of momentum fractions  $x_i$ . The situation is more complicated with the soft wavefunction  $\phi(y_i, Q)$ . By using QCD sum rules, one can extract the moments of this wavefunction from the experimental data. Since only a finite number of moments is known, such parameterizations are model-dependent. If one is only interested in the logarithmic corrections, one can use an expansion of  $\phi(x_i, Q)$  in a series of eigensolutions of the evolution equation [77].

$$\phi(x_i, Q) = x_1 x_2 x_3 \sum_{n=0}^{\infty} a_n \phi_n(x_i) \left( \ln \frac{Q^2}{\Lambda^2} \right)^{-\gamma_n}, \quad (8.4)$$

where  $\Lambda$  is the QCD scale parameter, and  $a_n$  and  $\gamma_n$  are some constants. Calculations performed with the soft wavefunction (8.4) give for the form factor  $F_1$ :

$$F_1(Q^2) = \frac{32\pi^2}{9} \frac{\alpha_s^2(Q^2)}{Q^4} \sum_{n,m} b_{n,m} \left( \ln \frac{Q^2}{\Lambda^2} \right)^{-\gamma_n - \gamma_m} [1 + O(\alpha_s(Q^2), m/Q)]. \quad (8.5)$$

Since the helicity-flip amplitude (associated with the Pauli form factor  $F_2$ ) is sup-

---

<sup>1</sup>Or more generally, any baryon.

pressed for high  $Q^2$ , for the leading term of the left-hand side of the Equation 8.5 can be replaced with  $G_M$ :

$$G_M(Q^2) \rightarrow \frac{32\pi^2}{9} C^2 \frac{\alpha_s^2(Q^2)}{Q^4} \left( \ln \frac{Q^2}{\Lambda^2} \right)^{-4/3\beta} (e_{\parallel} - e_{-\parallel}), \quad (8.6)$$

where  $e_{\parallel}$  ( $e_{-\parallel}$ ) is the mean charge of quarks with helicity parallel (antiparallel) to the baryon's helicity (for nucleons  $e_{\parallel}^p = 1$ ,  $e_{-\parallel}^p = 0$ ,  $e_{\parallel}^n = -\frac{1}{3}$  and  $e_{-\parallel}^n = \frac{1}{3}$ ),  $\beta = 11 - (2/3)n_{flavor}$ .

### Electric form factors

The contribution of the Pauli form factor  $F_2$  to the electric form factor  $G_E$  is amplified by a factor of  $Q^2$  and therefore cannot be neglected in the limit of  $Q^2 \rightarrow \infty$ . As we have already mentioned earlier,  $F_2$  is related to the helicity-flip amplitude. There are two mechanisms of a hadron helicity flip: quark masses and quark orbital angular momentum. Since the quark masses are small, it is generally believed that the latter mechanism is dominant.

Therefore, calculating the Pauli form factor  $F_2$  requires augmentation of the standard formalism with the parton orbital momentum. This technology has been recently developed by Burkardt, Ji and Yuan [78]. Based on it, Belitsky, Ji and Yuan have performed the calculations [79]. By using so called collinear expansion (expansion of the hard part of the diagram in  $k_i^2/Q^2$ , where  $k_i$  are quark transverse

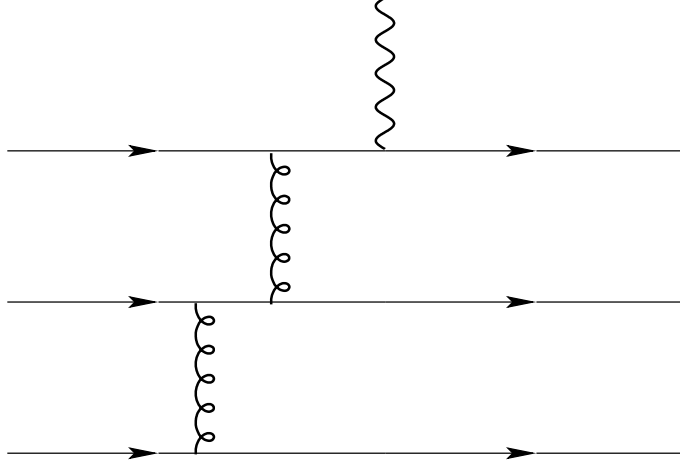


Figure 8.2: A two-gluon exchange hard scattering diagram for  $F_2^p$ . Permutations and mirror images need to be added.

momenta), they express  $F_2^p$  in terms of twist-3 and 4 amplitudes  $\Phi_3$ ,  $\Phi_4$  and  $\Psi_4$  as

$$F_2^p(Q^2) = \int [dx][dy] \{x_3 \Phi_4(x_1, x_2, x_3) T_\Phi(\{x\}, \{y\}) + x_1 \Psi_4(x_2, x_1, x_3) T_\Psi(\{x\}, \{y\}) \Phi_3(y_1, y_2, y_3)\}, \quad (8.7)$$

where  $\{x\} = (x_1, x_2, x_3)$ , the square brackets have the same meaning as in (8.3), and  $T_{\Psi, \Phi}$  are hard scattering diagrams (Figure 8.2 and its permutations and reflections). The exact solutions for the wavefunctions  $\Phi_3$ ,  $\Phi_4$  and  $\Psi_4$  can only be obtained by solving QCD non-perturbatively. However, their asymptotic form for large  $Q^2$  is known [80]:

$$\Phi_3 \sim x_1 x_2 x_3, \Phi_4 \sim x_1 x_2, \Psi_4 \sim x_1 x_3. \quad (8.8)$$

When trying to calculate (8.7) with wavefunctions (8.8) one ends up with diver-

gent (due to end-point singularities) integrals. The authors argue that higher-order pQCD resummation (the Sudakov form factor) provides an effective cut-off for the integrals at small  $x \sim \Lambda^2/Q^2$ , where  $\Lambda$  is a soft scale parameter related to the size of the nucleon. As a result, the Pauli form factor receives an additional logarithmic correction compared to the Dirac form factor, and the high- $Q^2$  prediction (8.2) modifies to:

$$Q^2 F_2(Q^2)/F_1(Q^2) \sim \ln^{2+8/(9\beta)} Q^2/\Lambda^2. \quad (8.9)$$

where for practical purposes the  $8/(9\beta)$  term can be neglected.

### 8.1.3 Comparison with experiment

At the moment, accurate high- $Q^2$  data is available only for  $G_M^p$ .  $G_M^n$  and  $G_E^p$  have only been measured at moderate  $Q^2$  (up to 4 and 6 (GeV/c)<sup>2</sup> correspondingly), while  $G_E^n$  is yet to be explored at  $Q^2 > 1.5$  (GeV/c)<sup>2</sup>.

The Figure 8.3 shows the magnetic form factor of the proton (for convenience plotted as  $Q^4 G_M^p$ ). The asymptotic behavior appears to set in at approximately 5 (GeV/c)<sup>2</sup> (the slow variations observable at high  $Q^2$  can be ascribed to log corrections).

Whether or not this means that pQCD is valid at the  $Q^2$  of a few (GeV/c)<sup>2</sup>, is still an open question. Skeptics believe that the agreement between the  $G_M^p$  behavior and the pQCD predictions is mere luck. It has even been claimed that no reasonable wavefunction can reproduce the correct normalization of the form factors

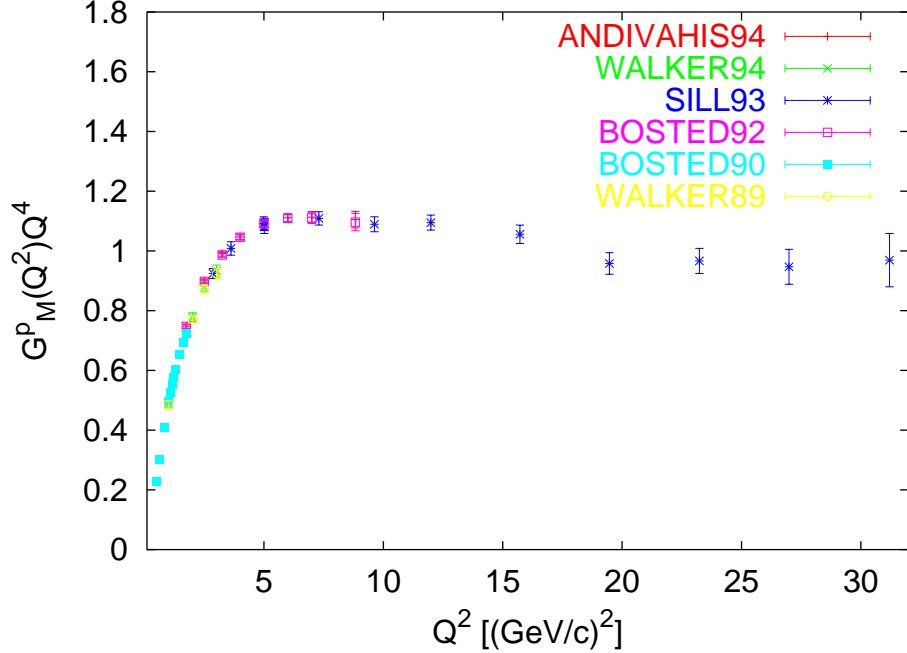


Figure 8.3: Asymptotic behavior of the proton magnetic form factor. The data are: red horizontal bars [81], green x's [82], blue asterisks [83], magenta squares [84], cyan squares [85] and yellow circles [86].

[87]. Carlson and Gross have shown that such a wavefunction does exist, although our present level of knowledge is not sufficient to tell whether this wavefunction realistically describes the actual distribution of the parton momentum fractions in the nucleon [88].

This discussion was further stimulated by recent results on the form factor ratio of the proton,  $G_E^p/\mu_p G_M^p$  [89], [90], [91], which exhibit a linear decline<sup>2</sup> of the ratio from 1 at 0 down to 0.27 at  $5.5 (\text{GeV}/c)^2$ . This corresponds to  $Q^2 F_2/F_1$  continuing to climb up, rather than setting in accordance with the naïve pQCD expectation

---

<sup>2</sup>It is probably worth mentioning here that these new results badly disagree with the older ones, obtained with the Rosenbluth separation (see [92] for a review) where this ratio stays roughly constant up to  $Q^2 = 6 (\text{GeV}/c)^2$ . A number of theorists suggested that the disagreement is due to the  $2\gamma$  exchange [93], [94].

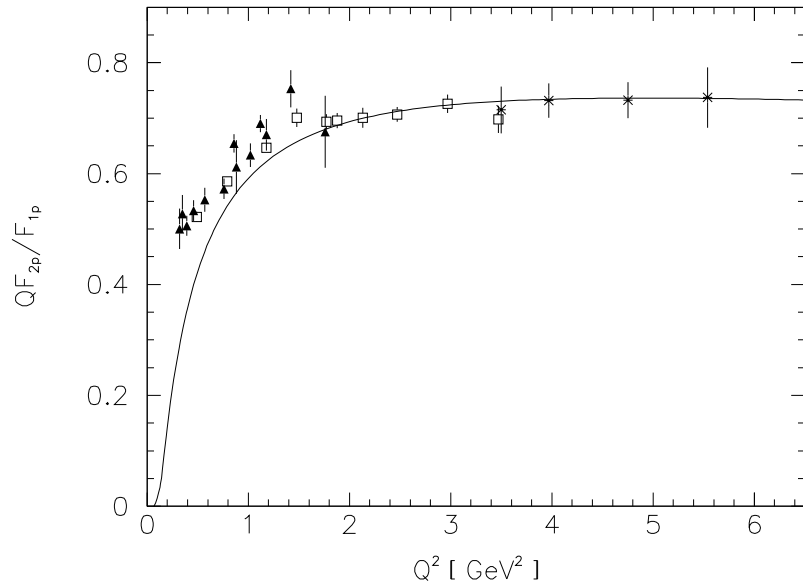
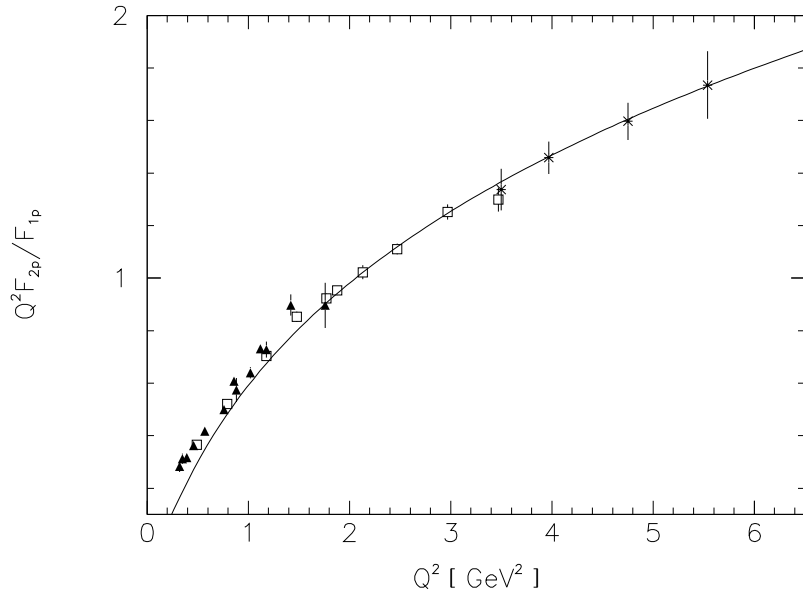


Figure 8.4: Recent data on the proton form factor ratio ( $F_2^p/F_1^p$ ) compared with the traditional pQCD scaling  $\sim 1/Q^2$  and helicity non-conserving scaling  $\sim 1/Q$ . The data points are: open squares [89], asterisks [90], filled squares [91]. The solid line shows Ji's scaling  $Q^2 F_2^p/F_1^p \sim \log Q^2/\Lambda^2$  [79] with the QCD scale parameter  $\Lambda = 0.3 \text{ GeV}/c$ .

$Q^2 F_2/F_1 \sim 1$  (see Figure 8.4). One possible explanation is that the truly asymptotic regime does not occur until much higher  $Q^2$  (of at least  $10 \text{ (GeV}/c)^2$ ), and the early scaling of  $G_M^p$  is accidental.

As an alternative explanation, some theorists have pointed to the violation of hadron helicity conservation (HHC) rule [95]. The HHC rule is a natural consequence of the pQCD factorization scheme. The hard scattering kernel is azimuthally symmetric to the leading order. The dependence on the azimuthal angle comes from the quark transverse momenta,  $k^\pm = (k_x \pm ik_y) = |\vec{k}_\perp| \exp(\pm i\phi)$ , which are small compared to the large momentum transfer,  $|\vec{k}_\perp| \sim \Lambda_{QCD} \ll Q$  [96]. If the quark orbital angular momentum in the initial and the final states differs by  $\Delta m$  units, the integrand in the pQCD factorization integral will receive a factor of  $\exp(i\Delta m\phi)$ . In order to survive the integration by  $d\phi$  this factor needs to be cancelled by a corresponding term from the expansion of the hard kernel in the transverse momentum. As a result, the contribution from the quark orbital angular momentum (OAM) becomes suppressed by  $(k_\perp^\pm/Q)^{\Delta m} \sim (\Lambda_{QCD}/Q)^{\Delta m}$ . Since quark current masses are small and cannot flip the hadron helicity, suppression of the contribution from the quark OAM leads to the conservation of the helicity of the hadron, i.e. the HHC rule.

Critics of the HHC stress that despite the theoretical attraction of the HHC rule, there are many experimental situations in which helicity conservation is not observed [97]. Further, it is argued that by making some simple assumptions (which

are not in conflict with the pQCD itself, but rather with the specific “*asymptotic short distance*” approach used in HHC derivation) one arrives at the scaling law of

$$QF_2/F_1 \sim \text{const}, \quad (8.10)$$

which fits the observed data quite well [95], [98].

However, the result of the direct pQCD calculation by Belitsky, Ji and Yuan described in the previous section, is also in an excellent agreement with the JLab data. Thus, the behavior of the  $F_2/F_1$  ratio for the proton can be interpreted as a consequence of the QCD logarithmic corrections (as earlier suggested by Brodsky [77]) rather than an evidence in favor of the HHC violation. It should be noted though, that the authors do not insist that the observed scaling of the JLab data with (8.9) is a truly asymptotic behavior. They remark that their calculation of  $Q^6 F_2^p(Q^2)$  with asymptotic wavefunctions of [99] recovers only 1/3 of the JLab experimental value at  $Q^2 = 5 \text{ (GeV}/c)^2$ . From that they conclude that higher-order corrections and higher-twist effects are still important at this kinematics, and suggest that the scaling may be a precocious one which owes its existence to some subtle cancellations in the ratio.

## 8.2 Dispersion relations

In the theory of functions of a complex variable, the analyticity of a function requires its real and imaginary parts to be related to each other by means of so called dispersion relations (DR). If one defines the four momentum transfer on the complex plane and imposes some constraints due to the properties of the scattering matrix and the analytic behavior of the scattering amplitudes (so called *unitarity* and *superconvergence* requirements), then one arrives to a set of integral equations relating elastic form factors  $F_{1,2}$  to the absorptive ones  $\mathcal{F}_{1,2}$  [4]:

$$F_{1,2}(Q^2) = F_{1,2}(0) - \frac{Q^2}{\pi} \int_{4m_\pi^2}^{\infty} dz \frac{\mathcal{F}_{1,2}(z)}{z(z + Q^2 - i\epsilon)}. \quad (8.11)$$

The relations (8.11) are also known as spectral mass representations, and the absorptive form factors are called spectral functions. The spectral functions characterize the nucleon structure as probed by a timelike (i.e.  $Q^2 < 0$ ) virtual photon and contain contributions from all states coupled to the  $N\bar{N}$  state that can be produced electromagnetically. Thus it is difficult to calculate the right-hand side (8.11) on purely analytical grounds. Therefore, in order to use the dispersion relations formalism for calculation of the elastic form factors, one needs to make further assumptions about the form of the spectral functions.

The simplest way to address the dispersion relations (8.11) is by assuming complete dominance of its right-hand side by low-lying resonances. This approach

(known as vector meson dominance) will be discussed in the next subsection.

A recent DR analysis of the elastic form factors of the nucleon by Mergell *et al.* [100] employs a more sophisticated model, which uses the extended unitarity relation of Frazer and Fulco [101] to express the absorptive isovector form factors in terms of the  $\pi N$  P-wave partial wave amplitude and the pion form factor corrected for  $\rho - \omega$  mixing. In addition to the two-pion contribution, three heavier excitations  $\rho'$ ,  $\rho''$  and  $\rho'''$  were added to the model and were found to have a significant impact. The low- $Q^2$  behavior of the form factor was fixed by the experimental data on nucleon charge radii, whereas the asymptotic behavior at high- $Q^2$  was determined by built-in constraints from the perturbative QCD.

### 8.3 Vector Meson Dominance

The concept of the vector meson dominance (VMD) was introduced by Sakurai [102]. The basic idea is that the interaction of a (virtual) photon with a nucleon is dominated by quark-antiquark pairs which overlap with vector meson states. In the language of dispersion relations this means that the mass spectral functions can be well approximated by a set of delta functions corresponding to sharp meson resonances:

$$\mathcal{F}_1^{V,S}(Q^2) = \sum_i A_i \delta(Q^2 + m_i^2), \quad (8.12)$$

where the superscripts  $V, S$  refer to isovector (V) and isoscalar (S) form factors,  $i = \rho, \omega, \phi \dots$  is the mesonic index,  $m_i$  is the mass of the meson, and  $A_i$  are constants depending on photon-meson and meson-nucleon coupling strengths. It is straightforward to see from Equation 8.11 that each delta function will result in a pole-like term

$$A_i/(1 + Q^2/m^2). \quad (8.13)$$

The pole-like form factors of VMD were very successful in describing the early (low  $Q^2$ ) form factor data. In fact, the prediction of existence of the  $\rho$  meson by Nambu in 1957 was inspired by the experimental results on the proton and neutron form factors [103]. However, the asymptotic behavior of the monopole form factors (8.13) is at odds with the dimensional scaling laws (8.1) and (8.2). Therefore, modern VMD models are forced to have a correct asymptotic behavior by either using “intrinsic” form factors or adding phenomenological terms.

The first work to include the pQCD asymptotics into a VMD model was that of Gari and Krümpelmann [104]. They used the extended version of VMD (EVMD) where the photon-nucleon interaction has a purely photonic part in addition to the traditional meson poles. A complete decoupling of the  $\phi$  meson from the nucleon with accordance to the OZI rule<sup>3</sup> [105] was assumed. Thus, the isovector and

---

<sup>3</sup>The OZI (Okubo-Zweig Iizuka) rule states that the disconnected (“hairpin”) diagrams are suppressed with respect to the continuous quark line graphs. According to this rule, non-strangeness of the nucleon means that coupling with the strange mesons ( $\phi$ ,  $K$ ) is small [105], [106], [107], [108].

isoscalar form factors were determined by the  $\rho$  and  $\omega$  mesons correspondingly:

$$F_1^{IV}(Q^2) = \left[ \frac{m_\rho^2}{m_\rho^2 + Q^2} \frac{g_\rho}{f_\rho} + \left( 1 - \frac{g_\rho}{f_\rho} \right) \right] F_1(Q^2) \quad (8.14)$$

$$\kappa_V F_2^{IV}(Q^2) = \left[ \frac{m_\rho^2}{m_\rho^2 + Q^2} \frac{\kappa_\rho g_\rho}{f_\rho} + \left( \kappa_V - \frac{\kappa_\rho g_\rho}{f_\rho} \right) \right] F_2(Q^2) \quad (8.15)$$

$$F_1^{IS}(Q^2) = \left[ \frac{m_\omega^2}{m_\omega^2 + Q^2} \frac{g_\omega}{f_\omega} + \left( 1 - \frac{g_\omega}{f_\omega} \right) \right] F_1(Q^2) \quad (8.16)$$

$$\kappa_V F_2^{IS}(Q^2) = \left[ \frac{m_\omega^2}{m_\omega^2 + Q^2} \frac{\kappa_\omega g_\omega}{f_\omega} + \left( \kappa_S - \frac{\kappa_\omega g_\omega}{f_\omega} \right) \right] F_2(Q^2). \quad (8.17)$$

The intrinsic Dirac and Pauli form factors were taken in a form providing the pQCD high- $Q^2$  behavior:

$$F_1(Q^2) = \frac{\Lambda_1^2}{\Lambda_1^2 + \hat{Q}^2} \frac{\Lambda_2^2}{\Lambda_2^2 + \hat{Q}^2} \quad (8.18)$$

$$F_2(Q^2) = \frac{\Lambda_1^2}{\Lambda_1^2 + \hat{Q}^2} \left[ \frac{\Lambda_2^2}{\Lambda_2^2 + \hat{Q}^2} \right]^2, \quad (8.19)$$

where  $\hat{Q}^2 = Q^2 \log \left( \frac{\Lambda_2^2 + Q^2}{\Lambda_{QCD}^2} \right) / \log \left( \frac{\Lambda_2^2}{\Lambda_{QCD}^2} \right)$ . A simultaneous fit to available at that moment cross-section data yielded an excellent  $\chi^2$  per degree of freedom of 0.43 and the values of free fit parameters were found to be close to the SU(3) expectations (or experimental values).

In a later work [109] Gari and Krümpelmann upgraded their model to include the effects of the strangeness content of the nucleon and introduced a helicity-flip scale. By that time (1992), more experimental data on the nucleon form factors have become available, including SLAC measurements of the  $G_E^p/G_M^p$  ratio with the Rosenbluth method. It was demonstrated that the increase of the  $G_E^p$  over the

dipole value  $G_D$  could be achieved by setting the helicity-flip scale to the meson scale, whereas the traditional model with the helicity-flip scale equal to the QCD scale  $\Lambda_{QCD}$  results in a decline of  $G_E^p$  with respect to the  $G_D$ . Another interesting result of this work is that the  $G_E^n$  is sensitive to the contribution from the  $\phi$  meson at moderate  $Q^2$ , and therefore can serve as a probe of the strange content of the neutron.

The work in this direction was continued by Lomon [110]. He studied two families of models: three models based on the original Gari-Krümpelmann approach (“GK models”) and four models with the  $\rho$ -meson pole replaced by a  $\rho'(1450)$ -meson pole plus an approximation for the  $\rho$ -meson term in the dispersion-relations integral from [100] (“DR-GK” models). The members of a model family differ between themselves only by details of cut-off and normalization parameters. It was found that the GK-DR model generally give a better agreement with the data than the GK fits. The relatively high  $\chi^2$  of the fits (about twice the number of degrees of freedom) was explained by inconsistencies between different experimental data sets.

## 8.4 Quark models

### 8.4.1 Nonrelativistic quark models

The picture of a nucleon<sup>4</sup> as consisting of three quarks in a confining potential started to emerge in early 1960-s in pioneering works of Zweig [106], Gell-Mann [111]

---

<sup>4</sup>More generally, any baryon.

and many others. Despite its simplicity, the model had remarkable successes in explaining hadronic mass spectra and radiative transition amplitudes, and is still widely used nowadays.

The key element of the model is the SU(6) spin-flavor symmetry<sup>5</sup> which allows to make two important predictions about the form factors without even making any specific assumptions about the quark-quark interaction potential. Namely, the ratios of the form factors for finite  $Q^2$  remain same as for the static case ( $Q^2 = 0$ ), i.e.  $G_M^n/G_M^p = -2/3$ ,  $G_E^n/G_E^p = 0$  [112].

One example of a non-relativistic quark model is the model of Isgur, Karl and Sprung [113] built on the analogy between QCD and QED. The confining potential is just the harmonic oscillator potential. The potential responsible for lifting the degeneracy of the mass multiplets of hadrons is analogous to magnetic-dipole-magnetic-dipole interactions of electromagnetism. Their results for the proton and neutron charge form factors

$$G_E^n(Q^2) = \frac{1}{6} \langle r^2 \rangle_n Q^2 e^{-Q^2/6\alpha^2}, \quad (8.20)$$

$$G_E^p(Q^2) = e^{-Q^2/6\alpha^2}. \quad (8.21)$$

are in a qualitative agreement with the experiment for low  $Q^2$ . However, the model is only valid for  $Q$  up to the constituent quark mass (i.e. a few hundred MeV/ $c^2$ ).

---

<sup>5</sup>This symmetry is only approximate (unlike e.g. exact SU(3) color symmetry).

## 8.4.2 Relativistic constituent quark models

The naïve picture of the nucleon sketched in the previous section is obviously an oversimplification. In reality the  $u$  and  $d$  quarks are about two orders of magnitude lighter than the hadrons they make up, and in addition to the three *valence* quarks there are gluons and quark-antiquark pairs (*sea* quarks). The success of the simple quark model suggests that sea and glue degrees of freedom are frozen, while their effects are hidden in the *constituent* (as opposed to physical, or *current* quarks) quark masses. However, one problem still remains: quark momenta are much higher than their masses, i.e. the quarks are highly relativistic. There have been a number of attempts to add relativity to the constituent quark model.

In the relativistic case there exists three distinct forms of the Hamiltonian dynamics, differing by what generators of the Poincaré group<sup>6</sup> are kinematical (i.e. interaction-free): instant form, point form and light-cone form [114]. In the point form (PF) and light-cone (LC) representations boosts are kinematic, and therefore they are particularly suitable for studying the form factors (it is easy to transform results obtained in one frame into any other frame).

### Light-cone

The light-cone dynamics is formulated in so-called light front variables,  $x^1$ ,  $x^2$ ,  $x^-$  and  $x^+$ , rather than ordinary world-point coordinates  $x^1$ ,  $x^2$ ,  $x^3$  and  $x^4$ . As was first

---

<sup>6</sup>Poincaré group is also known as the inhomogeneous Lorentz group. It is an extension of the traditional Lorentz group of Lorentz boosts and spatial rotations by space-time translations.

demonstrated by Berestetskiy and Terentiev [115], this substitution leads to significant simplifications in form factor calculations. Consider the relativistic energy-momentum relation:

$$p^\mu p_\mu + m^2 = 0. \quad (8.22)$$

In terms of the light-cone variables  $p^+$ ,  $p^-$  and  $\vec{p}^\perp = (p^1, p^2)$  this becomes:

$$2p^+p^- - (p_\perp)^2 + m^2 = 0. \quad (8.23)$$

On the LC, the plus component of the momentum has the meaning of the Hamiltonian,  $H = -p_+$ . If we introduce notation  $\mu = p_-$  we put Equation 8.23 into a familiar form:

$$H = (p_\perp^2 + m^2)/2\mu, \quad (8.24)$$

which is nothing else than the nonrelativistic Schrödinger equation for a particle of mass  $\mu$  on a two-dimensional plane. This analogy with the non-relativistic case is very helpful, since it implies impossibility of creating virtual pairs with finite energies due to conservation of  $\mu = p_-$  [115].

Chung and Coester [116], inspired by these advantages, performed an exploratory computation of nucleonic form factors using exactly Poincaré-covariant wavefunction, Gaussian in the quark momenta, from [117]:

$$\phi(M_0) = \frac{N(m_q/\Lambda_{QCD})}{\Lambda_{QCD}^2} \exp(-M_0^2/2\Lambda_{QCD}^2), \quad (8.25)$$

where  $M_0^2 = \left( \sum_i \sqrt{m_i^2 + \vec{q}_i^2} \right)^2$ ,  $m_i = m_q$  are quark masses (assumed to be equal),  $q_i$  are the quark relative momenta,  $N$  is the normalization factor and  $\Lambda_{QCD}$  is the familiar confinement scale. They found that the data can be satisfactorily described by the model if one uses small quark masses (0.24 GeV as opposed to the traditional value of 0.33 GeV) and a somewhat large QCD scale parameter (0.635 GeV). The quark form factors did not have any  $Q^2$  dependence.

The most recent studies within the framework of the light-cone dynamics were carried out by Cardarelli and Simula [1], [118], [119]. In [118] the authors consider Isgur's cancellation mechanism and confirm the result of [11] to show that  $G_E^n$  can indeed be interpreted as a measure of the charge distribution in the neutron. They establish that retaining the leading order in the relativistic expansion of [11] corresponds to neglecting the transverse motion of quarks in the Melosh rotations of the initial state, and show that in this approximation (which they call the *zitterbewegung* approximation) the non-relativistic SU(6) result  $G_E^n = 0$  still holds. Further, they use an example of a harmonic oscillator wavefunction of [113] to show that full Melosh rotations break SU(6) symmetry and generate non-zero  $G_E^n$  on a level that qualitatively explains the existing experimental data (although only 40% of the neutron charge radius could be reproduced).

In [1] Cardarelli and Simula further improved their model by including dynamical SU(6) symmetry breaking via spin-dependent quark-quark interactions and by using the  $y$ -component of the electromagnetic current (rather than the *plus* compo-

ment)<sup>7</sup> for the magnetic form factors. They show that although both non-relativistic and zitterbewegung approximations fail to describe the experimental data even with the dynamic SU(6)-breaking effects included, full light-cone calculations with the wavefunction of the one-gluon exchange model [120] agree with the experimental data on the EMFFN (including the JLab results on  $G_E^p/G_M^p$  [91]) fairly well. However, the neutron charge form factor is still underestimated (only 65% of the experimental value was reproduced).

A better agreement with the experiment can be achieved by using constituent quark form factors, as done by Simula in [119]. There he uses the low- $Q^2$  experimental data (up to 1 GeV/c) to fix the parameters of the constituent quark form factors, so the higher  $Q^2$  predictions can be considered to be in a sense parameter-free.

### Point-form

In the point-form representation all interaction is contained in the four-momentum operators, which commute among themselves and thus can be simultaneously diagonalized. As with the light-cone dynamics, boost operators are interaction-free.

The point-form dynamics formalism was recently applied to the studies of the nucleon form factors by Wagenbrunn *et al.* [121]. The nucleon is considered through the prism of spontaneous breaking of chiral symmetry  $SU(3)_L \times SU(3)_R$  down to  $SU(3)_V$  vector symmetry associated with Goldstone bosons. The quark-quark in-

---

<sup>7</sup>For the full current the situation is rotationally covariant, i.e. it does not matter which component is used in the calculation. However, that is not necessarily the case when only one-body currents are included (i.e. an impulse approximation is made) as in [1].

teraction potential consists of two parts: phenomenological linear confinement potential and instantaneous one-boson-exchange potential. The model has been very successful in describing the excitation spectra of light and strange baryons.

The Hamiltonian is diagonalized using the stochastic variational method [122], yielding eigenstates in the center-of-momentum frame. The form factors are then expressed in terms of the standard single-particle current operator for the quarks evaluated between the eigenstates, and several Wigner rotations. The authors emphasize that their model allows to obtain a satisfactory agreement with the experimental data without any adjustments (like constituent quark form factors, pionic cloud, etc.).

## 8.5 Diquark model

The diquark model was originally put forward in order to explain the experimental results on deep inelastic lepton-nucleon scattering, which suggested that only the struck parton participates in the interaction, while the rest of the nucleon behaves as a spectator quasiparticle (see [123] and references therein). It also provided an explanation for missing resonances in the baryonic mass spectrum by reducing the number of available degrees of freedom via coupling of two quarks into a bound state (a *diquark*).

With respect to exclusive reactions (including nucleon form factors), the diquark approach is tempting because it allows to extend the applicability of pQCD

factorization scheme<sup>8</sup> to lower  $Q^2$  by introducing an additional subasymptotic scale associated with the diquark. In the diquark picture, the nucleon is viewed as a bound state of a diquark and a quark at intermediate  $Q^2$ , whereas at high  $Q^2$  (when the individual quarks within the diquark are resolved by the virtual photon) the diquark models turns into the traditional pQCD, thus guaranteeing correct asymptotic behavior of the form factors.

This approach was adopted by Anselmino *et al.* [123]. They constructed the photon-diquark Feynman rules in a complete analogy with the standard Björken-Drell prescription [124], which was then generalized for the case of the gluon-diquark vertex:

$$-iG_S\lambda^\alpha/2(q_1 + q_2)^\mu$$

for the scalar ( $S = 0$ ) diquark and

$$-i\lambda^\alpha/2[G_1(q_1 + q_2)^\mu g^{\kappa\nu} - G_2(q_2^\kappa g^{\mu\nu} + q_1^\mu g^{\mu\kappa}) + G_3(q_1 + q_2)^\mu q_1^\nu q_2^\kappa]$$

for the vector ( $S = 1$ ) diquark. The form factors  $G_1$ ,  $G_2$ ,  $G_3$  and  $G_S$  are parametrized in the form:  $G_3 = 0$ ,  $G_S = g_S F_S(Q^2)$  and  $G_1 = G_2 = g_S F_V(Q^2)$ , where  $g_S$  is related to the strong coupling constant  $\alpha_S$  by  $g_S = \sqrt{4\pi\alpha_S}$ . Finally, the form factors  $F_V$  and  $F_S$  are parametrized by pQCD considerations in the following form:  $F_S(Q^2) = \frac{\alpha_S(Q^2)Q_0^2}{Q_0^2+Q^2}$ , and  $F_V(Q^2) = \frac{\alpha_S(Q^2)Q_1^2}{Q_1^2+Q^2}$  for zero helicity vertices with  $\tilde{F}_V(Q^2) = \frac{Q_2^2}{Q_2^2+Q^2}F_V(Q^2)$

---

<sup>8</sup>Also known as Brodsky-Farrar-Lepage factorization scheme.

otherwise.

With this, the pQCD factorization procedure (with appropriate modifications) for the form factors yields

$$G_M^p = \frac{8\pi C_F}{3Q^2} \left\{ \int dx dy \phi_S^*(y) \frac{\alpha_S(\hat{Q}^2) F_S(\hat{Q}^2)}{(1-x)(1-y)} \phi_S(x) - \frac{Q^2}{8m^2} F_V(Q^2) \int dx dy \phi_V^*(y) \frac{\alpha_S(\tilde{Q}^2)(1-x)(1-y) F_V(\tilde{Q}^2)}{xy} \phi_V(x) \right\}, \quad (8.26)$$

$$F_2^p(Q^2) = -\frac{2\pi C_F}{Q^2 \kappa} F_V(Q^2) \int dx dy \phi_V^*(y) \frac{\alpha_S(\tilde{Q}^2) F_V(\tilde{Q}^2)}{xy} \phi_V(x), \quad (8.27)$$

$$G_M^n = \frac{4\pi C_F}{3Q^2} \left\{ \int dx dy \phi_S^*(y) \frac{\alpha_S(\hat{Q}^2) F_S(\hat{Q}^2)}{(1-x)(1-y)} \phi_S(x) - \frac{Q^2}{12m^2} F_V(Q^2) \int dx dy \phi_V^*(y) \frac{\alpha_S(\tilde{Q}^2)(1-x)(1-y) F_V(\tilde{Q}^2)}{xy} \phi_V(x) \right\}. \quad (8.28)$$

A study along these lines was conducted by Kroll, Schürmann and Schweiger [125]. They used distribution amplitudes of the form

$$\phi_S(x_1) = \phi_V(x_1) = Ax_1 x_2^3 \exp \left[ -b^2 \left( \frac{m_q^2}{x_1} + \frac{m_D^2}{x_2} \right) \right] \quad (8.29)$$

where quark and diquark masses are taken to be  $m_q = 330$  MeV and  $m_D = 580$  MeV, and  $x_{1,2}$  are usual light-cone momentum fractions. The dependence of the full wavefunction on the transverse momentum  $k_T$  is assumed to be of the form

$$\sim \exp \left[ -b^2 \frac{k_T^2}{x_1 x_2} \right], \quad (8.30)$$

where  $b$  is a harmonic oscillator scale parameter, fixed in such a manner that  $\sqrt{\langle k_T^2 \rangle} = 600$  MeV. The results for the  $G_M^p$  compare quite favorably with the experimental database available at that moment (1991) which has not changed significantly since then. The authors did not make a direct comparison with the low- $Q^2$  data available for the other three nucleonic form factors because of the perturbative nature of their calculations.

In a recent work by Ma, Qing and Schmidt [126] the diquark model is formulated on the light cone. The authors use a general form of the proton wavefunction

$$\Psi_p^{\uparrow\downarrow}(qD) = \sin\theta\phi_V|qV\rangle^{\uparrow\downarrow} + \cos\theta\phi_S|qS\rangle^{\uparrow\downarrow}, \quad (8.31)$$

$$|qV\rangle^{\uparrow\downarrow} = \pm\frac{1}{3}[V^0(ud)u^{\uparrow\downarrow} - \sqrt{2}V^{\pm 1}(ud)u^{\uparrow\downarrow} \quad (8.32)$$

$$-\sqrt{2}V^0(uu)d^{\uparrow\downarrow} + 2V^{\pm 1}(uu)d^{\uparrow\downarrow}] \quad (8.33)$$

$$|qS\rangle^{\uparrow\downarrow} = S(ud)u^{\uparrow\downarrow}, \quad (8.34)$$

where  $\theta$  is the mixing angle that breaks the SU(6) symmetry (if  $\theta \neq \pi/4$ ), and  $V^{Sz}$  and  $S^{Sz}$  are vector and scalar diquark instant form Fock states. However, in the actual calculations only the SU(6)-symmetric case  $\phi = \pi/4$  is studied. The momentum wavefunction used in the model is of the harmonic oscillator type

$$\phi_D(x, \vec{k}_\perp) = A_D \exp \left\{ -\frac{1}{8b^2} \left[ \frac{m_q^2 + \vec{k}_\perp^2}{x} + \frac{m_D^2 + \vec{k}_\perp^2}{1-x} \right] \right\}, \quad (8.35)$$

while the spin part of the wavefunction is obtained by transforming instant states

into light-cone states via standard spin-1/2 Melosh rotations for the quark and via prescription of Ahluvalia and Sawicki for Melosh rotation of the vector diquark [127] (for the scalar diquark there is obviously no Melosh transform, since there is no spin).

As usual in the light-cone formalism, the form factors are expressed in terms of the helicity-flip and helicity-nonflip matrix elements of the plus component of the electromagnetic current:

$$\langle \uparrow | \frac{J^+(0)}{2P^+} | \uparrow \rangle = F_1^N(Q^2), \quad (8.36)$$

$$\langle \uparrow | \frac{J^+(0)}{2P^+} | \downarrow \rangle = -(q_1 - iq_2) \frac{F_2^N(Q^2)}{2M}. \quad (8.37)$$

With the choice of the proton wavefunction given by Equation 8.35 the results for the proton form factors<sup>9</sup>

$$F_1^p(Q^2) = 3 \int \frac{d^2k_\perp dx}{16\pi^3} \frac{2}{3} \cos^2 \theta w'_q w_q [(k'^+ + m_q)(k^+ + m_q) + k'^L k^R_\perp] \phi_S(x, \vec{k}'_\perp) \phi_S(x, \vec{k}_\perp). \quad (8.38)$$

$$F_2^p = \frac{6M}{-q^L} \int \frac{d^2k_\perp dx}{16\pi^3} \frac{2}{3} \cos^2 \theta w'_q w_q [(k'^+ + m_q)k^L_\perp - (k_q^+ + m_q)k'^L_\perp] \phi_S(x, \vec{k}'_\perp) \phi_S(x, \vec{k}_\perp), \quad (8.39)$$

where  $k^{R,L} = k^1 \pm k^2$  (and similarly for  $q$ ), and  $\vec{k}'_{\perp i} = \vec{k}_{\perp i} + (1 - x_i)\vec{q}_\perp$  for the struck

---

<sup>9</sup>The results for the neutron form factors are more cumbersome. The interested reader should refer to the appendix of the discussed article.

quark and  $\vec{k}'_{\perp i} = \vec{k}_{\perp i} - x_i \vec{q}_{\perp}$  for each spectator.

## 8.6 Soliton model

Solitons (solitary nonlinear waves) were first observed in XIX century in hydrodynamics. With the rapid development of the numerical methods (due to advent of computers) in the second half of the XX century, studies of solitons in application to various branches of physics and other sciences have gained a wide popularity. Two distinctive features, localization in space and preservation of identity through collisions, made solitons interesting for particle physicists.

Long before QCD, in 1960 Skyrme has suggested a field theory with classical soliton solutions and an  $SU(2) \otimes SU(2)$  symmetry spontaneously broken to  $SU(2)$  as the theory of strong interactions [128]. The traveling waves in this model were interpreted as pions, and the solitons were identified with baryons. The interest to this model was reignited when it was shown that a theory of this kind arises in the  $1/N_c$  expansion for QCD. The theory was relatively successful in describing static nucleon properties [129], however, first studies with the nucleon form factors [130] have shown that the bare Skyrme model is not sufficient for explaining the experimental data and inclusion of vector meson effects is necessary.

Recently, Holzwarth conducted a study of the chiral soliton model [131], where he has investigated two models representing two distinct ways of including vector

meson effects into the form factors into the standard pionic Skyrme Lagrangian:

$$\mathcal{L}^{(\pi)} = \mathcal{L}^{(2)} + \mathcal{L}^{(4)} \quad (8.40)$$

$$\mathcal{L}^{(2)} = \frac{f_\pi^2}{4} \int (-\text{Tr} L_\mu L^\mu + m_\pi^2 \text{Tr}(U + U^\dagger - 2)) d^3x, \quad (8.41)$$

$$\mathcal{L}^{(4)} = \frac{1}{32e^2} \int \text{Tr}[L_\mu, L_\nu]^2 d^3x, \quad (8.42)$$

where  $L_\mu$  denotes the chiral gradient  $L_\mu = U^\dagger \partial_\mu U$ ,  $m_\pi = 138$  MeV is the pion mass, is the pion decay constant  $f_\pi = 93$  MeV and  $e = 4.25$  is the Skyrme parameter.

In Model A the vector meson effects were accounted for by multiplying the form factors by

$$\Lambda_I(Q^2) = \lambda_I \left( \frac{m_I^2}{m_I^2 + Q^2} \right), \quad (8.43)$$

where the label  $I$  refers to the isospin (and  $m_0$  and  $m_1$  are masses of the isoscalar  $\rho$  and isovector  $\omega$  mesons, correspondingly).

In Model B vectors mesons terms are explicitly included into the Lagrangian:

$$\mathcal{L} = \mathcal{L}^{(\pi)} + \mathcal{L}^{(\rho)} + \mathcal{L}^{(\omega)}, \quad (8.44)$$

$$\mathcal{L}^{(\rho)} = \int \left( -\frac{1}{8} \text{Tr} \rho_{\mu\nu} \rho^{\mu\nu} + \frac{m_\rho^2}{4} \text{Tr}(\rho_\mu - \frac{i}{2g_\rho}(l_\mu - r_\mu))^2 \right) d^3x, \quad (8.45)$$

$$\mathcal{L}^{(\omega)} = \int \left( -\frac{1}{4} \omega_{\mu\nu} \omega^{\mu\nu} + \frac{m_\omega^2}{2} \omega_\mu \omega^\mu + 3g_\omega \omega_\mu B^\mu \right) d^3x, \quad (8.46)$$

with the topological baryon current  $B_\mu = \frac{1}{24\pi^2} \epsilon_{\mu\nu\rho\sigma} \text{Tr} L^\nu L^\rho L^\sigma$ , and  $l_\mu = \xi^\dagger \partial_\mu \xi$ ,

$r_\mu = \partial_\mu \xi \xi^\dagger$ , where  $\xi^2 = U$ .

Both models give a satisfactory description of charge and magnetization radii and magnetic moments of the neutron and proton.

## 8.7 Overview

In this section we shall compare the predictions of various nucleon models to existing experimental data on nucleon form factors. For each model described in the previous sections of the chapter we chose the most successful fit<sup>10</sup>.

Not surprisingly, the best agreement with the experimental data is obtained by Lomon's fits [110]. This is due to the semi-phenomenological nature of the model (i.e. built-in pQCD behavior) and the large number of free parameters of the model. Other models may provide better physical insight, but none of them provides an adequate description of all nucleon form factors for the entire range of the momentum transfer.

Let us consider the magnetic form factors first (as the experimental data is less ambiguous here). Figure 8.5 shows the results for the magnetic form factors presented in the traditional form (with the dipole form factor  $G_D = (1 + Q^2/\Lambda_D)^{-2}$  divided out). Only Simula's light-cone calculation based on one-gluon exchange wavefunction [119] describes both magnetic form factors well (although the results of the calculation are only available up to 10 (GeV/c)<sup>2</sup>). The soliton model [131]

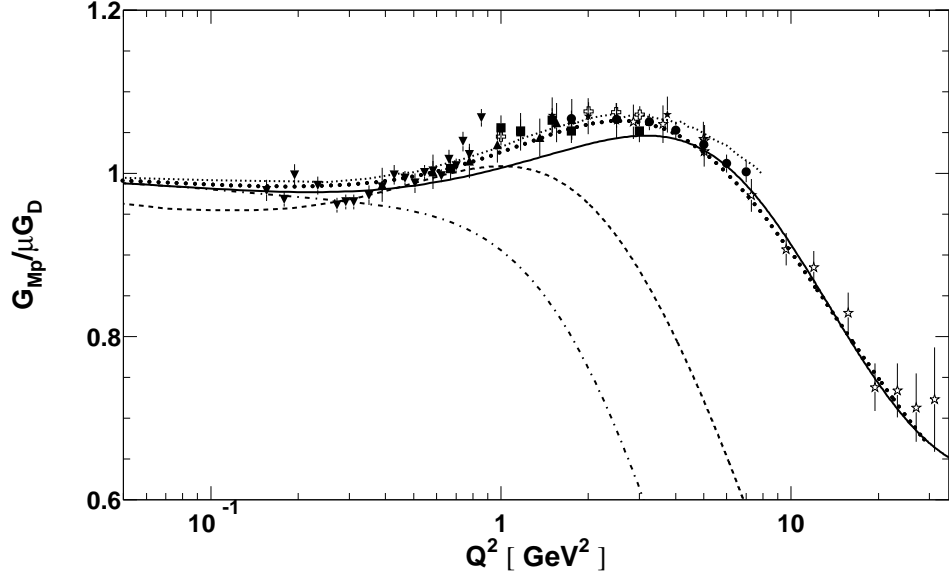
---

<sup>10</sup>The results of the dispersion relations analysis of Mergell *et al.* [100] are not included into this overview since they are essentially contained in the later study of Lomon [110].

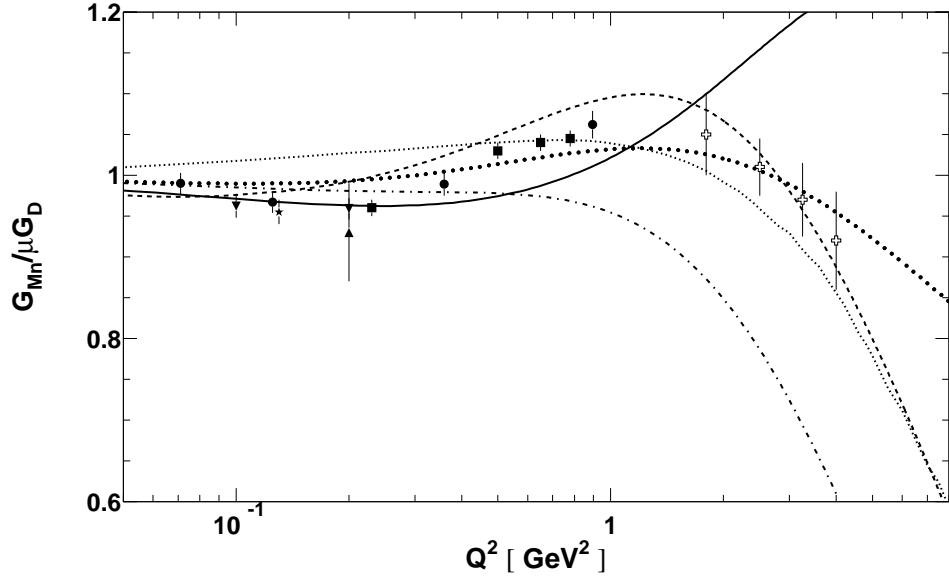
does a very good job for the  $G_M^p$ , but the prediction for  $G_M^n$  starts deviating from the data at about  $1 \text{ (GeV}/c)^2$ . The case is the opposite for the point-form Goldstone-boson-exchange model of [121]. Finally, the predictions of the light-cone diquark model [126] fall short of the data for the both form factors.

The experimental data on the  $G_E/G_M$  ratio of the proton is not helpful in evaluating performance of different models before the controversy between Rosenbluth [81], [133], [134], [139] and polarized [90], [140] measurements is resolved.

Finally, let us consider the charge form factor of the neutron (the discussion of results of the present experiment is postponed until later). None of the models provides an accurate description of the data within the entire measured  $Q^2$  range. Recent recoil polarized measurements at the JLab [27] (which provide the most accurate high  $Q^2$  data at the moment) seem to favor the Simula's prediction; the prediction of the diquark model also is not far off. The soliton model, although successful for describing  $G_E^n$  data at low- $Q^2$ , tends to underpredict the data starting at  $1 \text{ (GeV}/c)^2$ .



(a) Proton.



(b) Neutron.

Figure 8.5: Magnetic form factors of the nucleon. The models shown are: soliton B1 [131] (solid), point-form spectator approximation [121] (dashed), light-cone one-gluon exchange [119] (dotted), light-cone diquark [126] (dash-dotted) and the DR-VMD fit [110] (bold-dotted). The experimental data are from [81], [82], [83], [132], [133], [134], (for the proton) and [13], [135], [136], [137], [138], [75] (for the neutron).

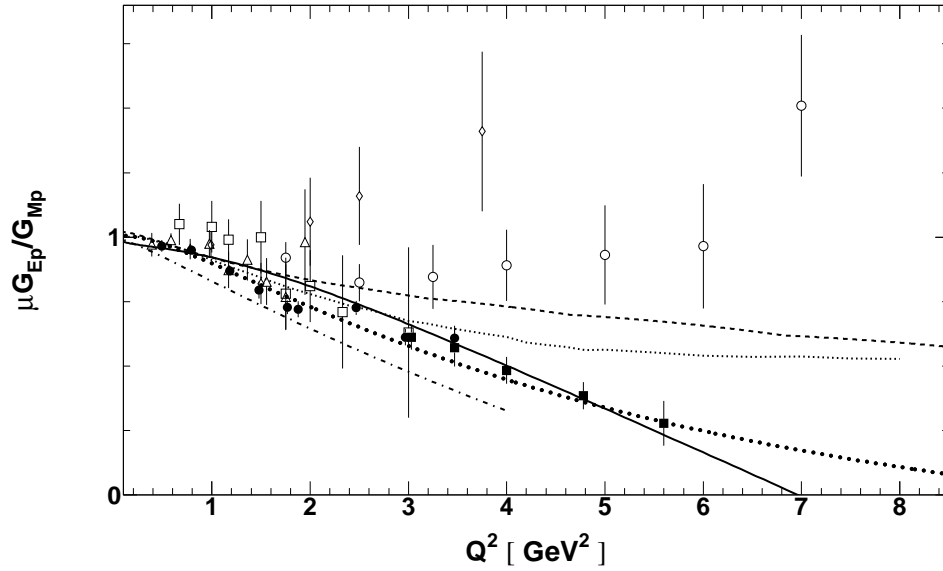


Figure 8.6: The  $G_E/G_M$  ratio for the proton. Open symbols are Rosenbluth data [81], [133], [134], [139], filled symbols are polarized data [90], [140]. Models are the same as in Figure 8.5.

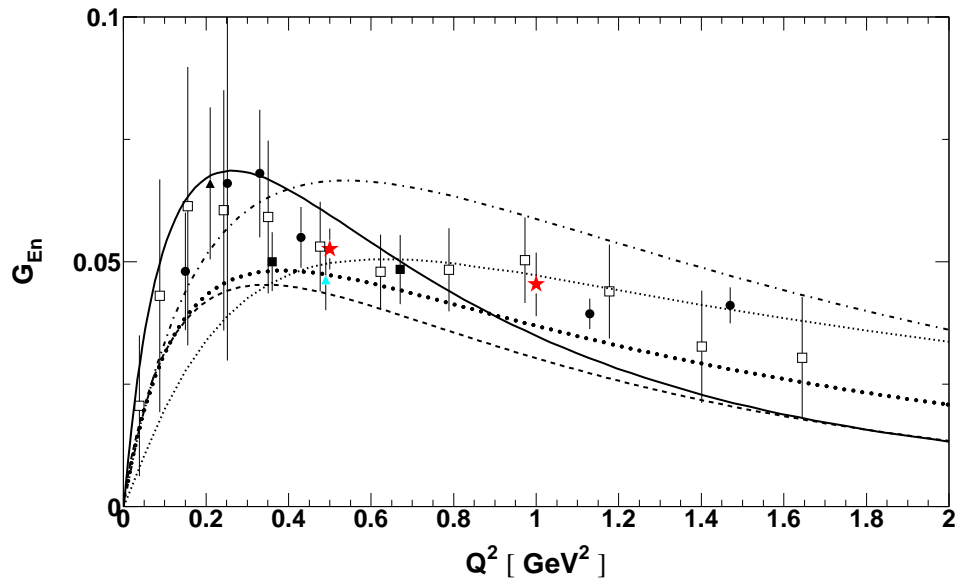


Figure 8.7: The electric form factor of the neutron. The E93-026 2001 run results are shown with red stars. Other data are: open squares – analysis of the deuteron quadrupole form factor [22], filled circles – recoil polarization [25], [141], [27], filled squares –  $\vec{H}e^3$  target [31], [33], filled triangles –  $\vec{d}$  target [35], [34]. Models are the same as in Figure 8.5.

# Chapter 9

## Discussion

As we have seen in the previous two sections, the results of the present experiment, as well as those of other recent experiments, can be described by a simple parametrization (7.10). This gives us confidence that the formalism employed by the experimental methods is adequate (at least in this kinematic regime) and the measurements are free of major problems.

This consistency is especially important in light of the recent controversy for the charge form factor of the proton, where the disagreement between the Rosenbluth and polarization measurements is interpreted by many theorists as an evidence of the two-photon exchange. If the importance of the two-photon exchange contribution is confirmed, the entire formalism of the electron-nucleon scattering will be challenged (for example, it will be longer possible to represent the electromagnetic structure of the nucleon in terms of just two form factors [94]).

Unfortunately, the accurate  $G_E^n$  data is only available up to the region where the Rosenbluth and polarized results for the proton begin to diverge. More accurate

data taken with several approaches is needed at  $Q^2 \geq 2\text{GeV}/c^2$ .

The Galster parametrization (7.10) has been traditionally considered as having no fundamental physical significance. Recently, Kaskulov [142] has shown that under some approximations  $G_E^n$  can be obtained as:

$$G_E^n(Q^2) = \frac{\langle r^2 \rangle^n}{6} Q^2 F_\pi(Q^2) G_D(Q^2), \quad (9.1)$$

where  $F_\pi(Q^2)$  is the form factor of the pion, which has monopole  $Q^2$ -dependence. The parametrization (9.1) is of the same form as the Galster fit (7.10). Therefore, the success of the Galster form at low  $Q^2$  can be considered as a manifestation of the chiral content of the nucleon. For higher  $Q^2$ , exchange currents are expected to become important.

A careful examination of Figure 7.15 shows that the Galster parameterization is less successful at  $Q^2 < 0.4 \text{ GeV}/c^2$  than elsewhere. The fact that it is hard to keep the nuclear corrections under control for lower  $Q^2$ , and the large error bars at this kinematics, preclude any definitive conclusions. However, if one believes that the grouping of these data above the Galster line is neither coincidental nor due to some common flaw in the data analysis, then one can see that the  $G_E^n$  database can be better fitted with a superposition of a broad Galster-like fit and a low- $Q^2$  “bump”. Such an ansatz was made by Friedrich and Walcher [143]. They convincingly argue that the “bump” can be identified with the pion cloud, which reaches as far out as 2 fm, whereas the broader part corresponds to the constituent quark dynamics. The

authors stress the need for accurate data at moderate  $Q^2$  to test their hypothesis.

Even though none of the QCD-inspired models considered in the previous chapter provides a complete description for all four electromagnetic form factors within the entire experimental range, it should be noted that all of them successfully reproduce the most essential features of the data: the dipole behavior of the magnetic form factors at modest  $Q^2$  and positive non-zero  $G_E^n$ . Non-relativistic SU(6) models could not recover these features, and thus one can conclude that both relativistic effects and dynamical SU(6) breaking via spin-dependent quark-quark interaction are important for understanding the electromagnetic structure of the nucleon.

The results of the presented experiment and another recent JLab experiment [27] had an appreciable impact on the extracted charge density of the neutron [5] (see Figure 9.1). One distinctive new feature of the updated densities is a positive bump at about 1-1.5 fm, which is not consistent with the traditional interpretation of the charge distribution neutron in terms of a positive core and a negative pion cloud. The author states that this is a stable and model-independent feature of the analysis which cannot be eliminated without damaging the quality of the form factor fits at  $Q^2 \sim 1 \text{ GeV}/c^2$ . As suggested by the author, such oscillatory behavior of the charge density may be a signature of the  $d$ -state component of the wavefunction which is probably broader spatially than that of the  $s$ -state.

Recent accurate measurements of  $G_E^n$  with the polarized target had a pronounced positive impact on our understanding of the electromagnetic structure of

the nucleon. It could be of interest to apply this experimental method to the proton form factors. Measuring  $G_E^p/G_M^p$  with a polarized target could not only help to resolve the controversy between Rosenbluth and polarized data, but also provide useful information for quantitative studies of the effects two gamma exchange if the latter are found to be of significance. In that case, extraction of the three form factors (traditional  $G_{E,M}$  and the one associated with the two photon exchange) will require measurements with two or more independent experimental methods.

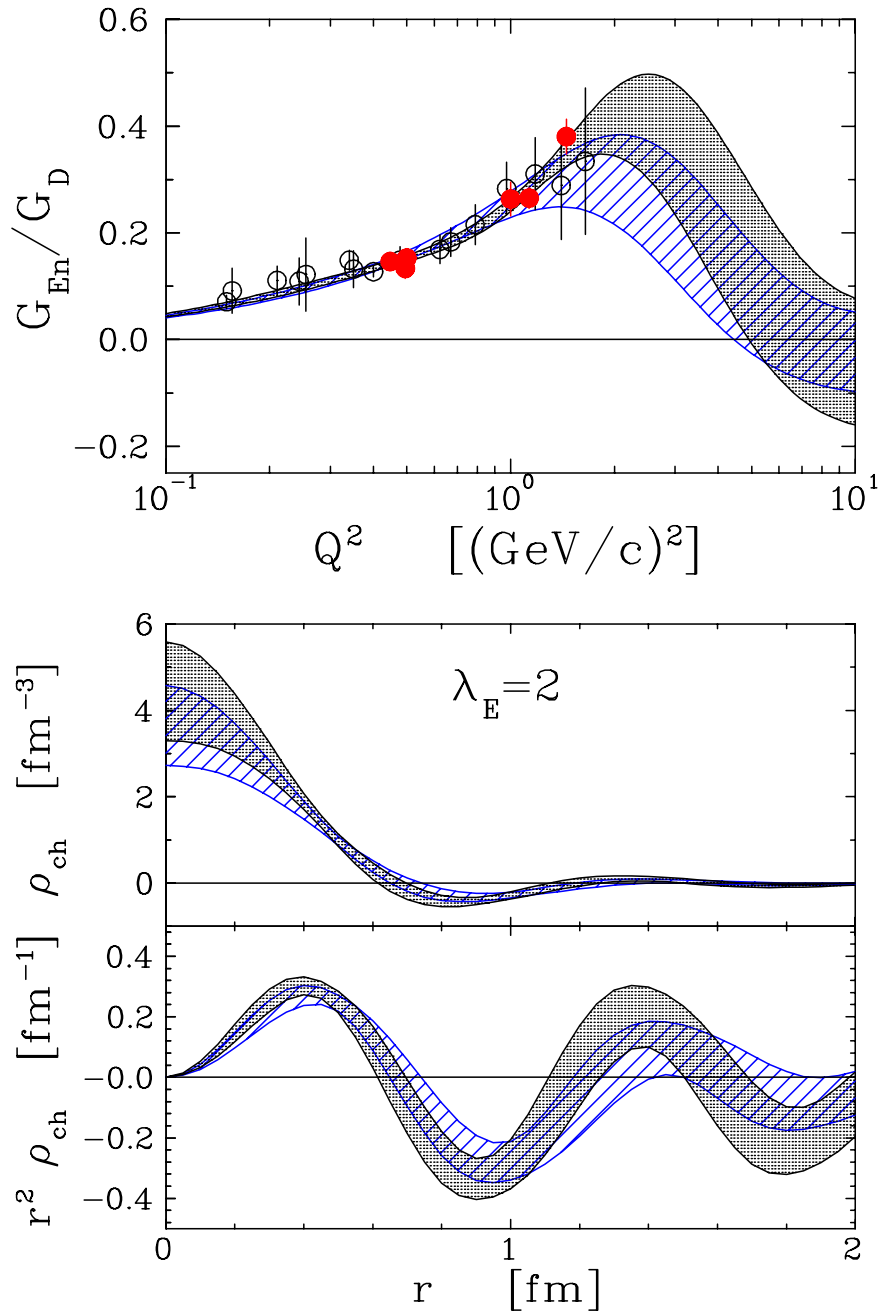


Figure 9.1: Charge and magnetization densities of the neutron. Top panel:  $G_n^E$  data used in the extraction. Recent JLab data points (the present experiment and [27]) are shown in red. Bottom panel: extracted charge densities before (blue hatches) and after (grey hatches) the recent JLab measurements.

# Chapter 10

## Summary and outlook

In the experiment described here (JLab E93-026) the charge form factor of the neutron was measured at  $Q^2 = 0.5$  and  $1.0$   $(\text{GeV}/c)^2$ . The data analysis for  $Q^2 = 1.0$  was discussed. The result is:

$$G_E^n(Q^2 = 1.0) = 0.0454 \pm 0.0054(\text{stat}) \pm 0.0037(\text{sys}). \quad (10.1)$$

This data point is the highest  $Q^2$  datum measured with a polarized target. Together with another recently published JLab experiment (E93-038), this experiment provides the only accurate direct measurements of  $G_E^n$  at  $Q^2 > 1.0$   $(\text{GeV}/c)^2$ .

The theoretical calculations used in the extraction of  $G_E^n$  included the relativistic effects as well as contributions from meson exchange currents, isobar configurations and final state interactions. Studies of the reaction mechanism dependence confirm the prediction of the Arenhövel's model [36] that the sensitivity of this method of measurement to meson exchange currents and the final state interactions is small (2% and 5% respectively) and decreases with the increase of  $Q^2$ .

Based on our and other experimental results, an improved Galster parametrization was suggested:

$$G_E^n = \frac{0.86\mu_n\tau}{1 + 3.06\tau}(1 + Q^2/0.71)^{-2}, \quad (10.2)$$

where as usual  $\tau = Q^2/4m^2$  and the units of  $Q^2$  are assumed to be  $(\text{GeV}/c)^2$ .

Our experimental results are consistent with the recoil polarimetry measurement by Madey *et al.* and the deuteron quadrupole form factor analysis by Sick and Schiavilla.

The experiment E93-026 has been a part of massive experimental program at the JLab and other nuclear facilities (NIKHEF, MAMI, MIT-Bates) aiming at improvement of our knowledge of the electromagnetic structure of the neutron. Thanks to this ongoing effort by many experimentalists, the typical uncertainties in  $G_E^n$  have been reduced from 30 – 40% ten years ago to 10%. The situation will be further improved upon completion of two other experiments. The JLab experiment E02-013 will extend our knowledge of  $G_E^n$  to higher  $Q^2$ , whereas the BLAST experiment at MIT-Bates will improve the accuracy of the world  $G_E^n$  database at low and intermediate  $Q^2$ .

# Appendix A

## Principles of operation of the E93026 polarized target

### A.1 Dynamic nuclear polarization

Unpaired nuclear spins align with the direction of the external magnetic field. Therefore, the simplest method of polarizing a material is by placing it into a strong magnetic field. Statistical physics gives the relation between the polarization and spin  $J$  of the nucleus as follows [50]:

$$P = \frac{2J+1}{2J} \coth\left(\frac{2J+1}{2J} \frac{\mu B}{kT}\right) - \frac{1}{2J} \coth\left(\frac{1}{2J} \frac{\mu B}{kT}\right), \quad (\text{A.1})$$

where  $\mu$  is the magnetic moment of the nucleus,  $B$  is the magnetic field,  $T$  is the spin temperature <sup>1</sup> and  $k$  is the Boltzmann's constant.

For the particular case of a spin-1 system this expression simplifies to:

---

<sup>1</sup>In thermal equilibrium the spin temperature is equivalent to the temperature of the system.

$$P = \frac{4 \tanh(\mu B/2kT)}{3 + \tanh^2(\mu B/3kT)}. \quad (\text{A.2})$$

For realistic experimental values of  $B$  and  $T$  the nuclear polarization is low. For example, for the values of this experiment,  $B = 5$  Tesla and  $T = 1$  K, the deuteron thermal polarization is only 0.14%. However, the electron polarization is very high (99.8%), and this high polarization can be transferred to nuclei using mechanism which bears name of dynamic nuclear polarization (DNP).

Let us consider how DNP works in  $NH_3$  targets<sup>2</sup>. When the material is placed in a magnetic field, degeneration in  $m$ , the quantum number for projection of spin onto the field direction, is lifted due to Zeeman terms of the Hamiltonian. The energy eigenstates are pure spin states.

If then the material is doped with paramagnetic radicals, providing free electrons, the spin-spin interaction with unpaired electron spins makes nucleon energy eigenstates mixed spin states (Figure A.1):

$$|e \downarrow N \uparrow\rangle \rightarrow |1\rangle = |e \downarrow N \uparrow\rangle + \epsilon_1 |e \downarrow N \downarrow\rangle \quad (\text{A.3})$$

$$|e \downarrow N \downarrow\rangle \rightarrow |2\rangle = |e \downarrow N \downarrow\rangle + \epsilon_1^* |e \downarrow N \uparrow\rangle \quad (\text{A.4})$$

$$|e \uparrow N \uparrow\rangle \rightarrow |3\rangle = |e \uparrow N \uparrow\rangle + \epsilon_2 |e \uparrow N \downarrow\rangle \quad (\text{A.5})$$

---

<sup>2</sup> $ND_3$  is more complicated due to quadrupole moment and higher spin of deuteron, but all essential features are the same.

$$|e \uparrow N \downarrow\rangle \rightarrow |4\rangle = |e \uparrow N \downarrow\rangle + \epsilon_2^* |e \uparrow N \uparrow\rangle, \quad (\text{A.6})$$

where mixing coefficients  $\epsilon_{1,2}$  are small ( $|\epsilon_{1,2}| \ll 1$ ).

The double-flip transitions, forbidden in the absence of the spin-spin interaction due to dipole selection rules, are now allowed. By bombarding the material with photons of frequency  $(\mu_e + \mu_N)B/h$  it is possible to cause transitions from state  $|2\rangle$  (nucleon spin anti-aligned) to state  $|3\rangle$ . Since electron relaxation time is small (a few orders of magnitudes larger than that of nucleons), this transition is almost immediately followed by a decay of the  $|3\rangle$  to a  $|1\rangle$ . As a result, the positive polarization of the material is increased. In exactly the same way a negative polarization of material can be achieved by using photons of frequency  $(\mu_e + \mu_N B)/h$ .

The polarization is further enhanced by a mechanism, known as spin diffusion. In this process the nuclear polarization is transferred to neighboring nuclei via dipole-dipole coupling.

## A.2 NMR polarization measurement

### NMR system

The target polarization was measured using NMR technique [144]. The idea of the method is based on the fact that the polarization of a material placed in a varying magnetic field of frequency  $\omega$  is related to the absorptive part of the magnetic susceptibility of the material [144]:

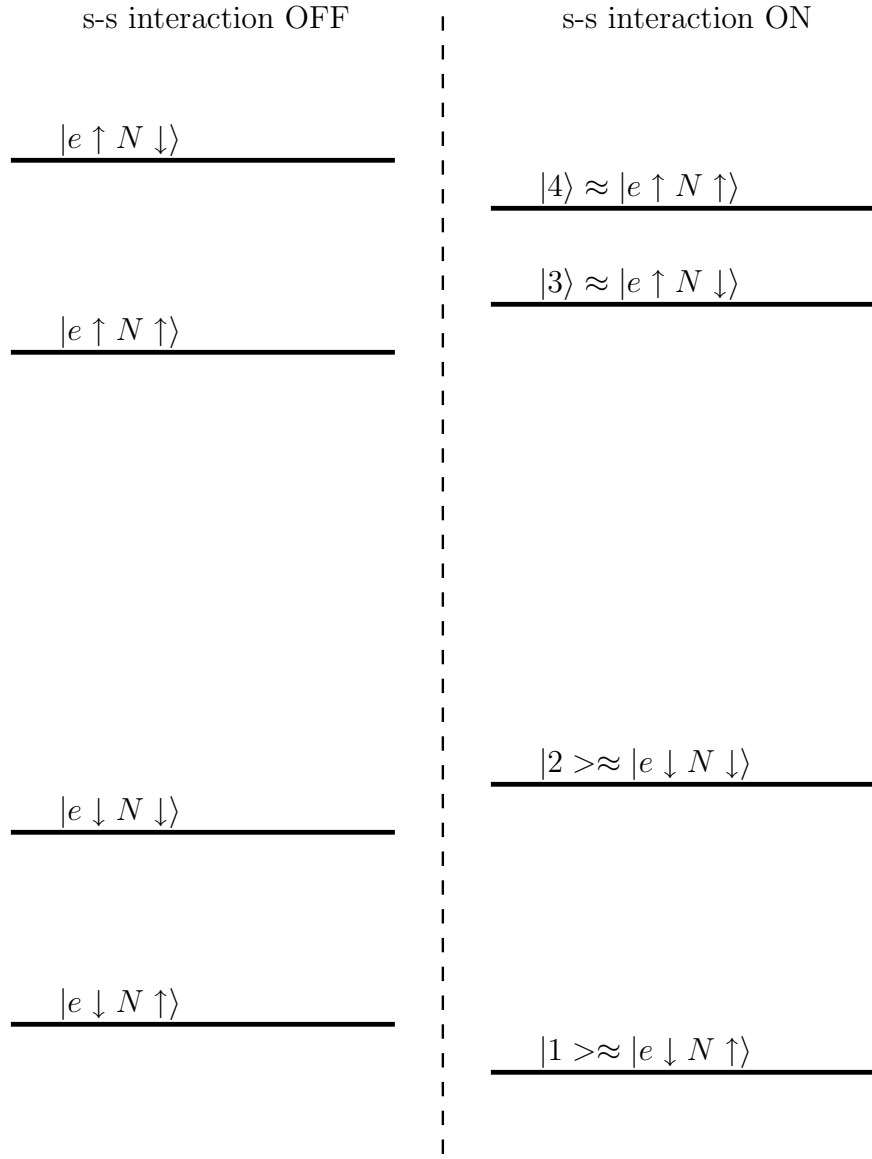


Figure A.1: The effect of spin-spin interaction on levels and states of an electron-nucleon system in an external magnetic field. On the left: pure spin levels in absence of spin-spin interaction. On the right: spin-spin interaction shifts the energy levels and mixes pure spin states, making previously forbidden double-flip transitions allowed.

$$P = \frac{2}{\mu_0 \pi \hbar \gamma^2 N J} \int_0^\infty \chi''(\omega) d\omega, \quad (\text{A.7})$$

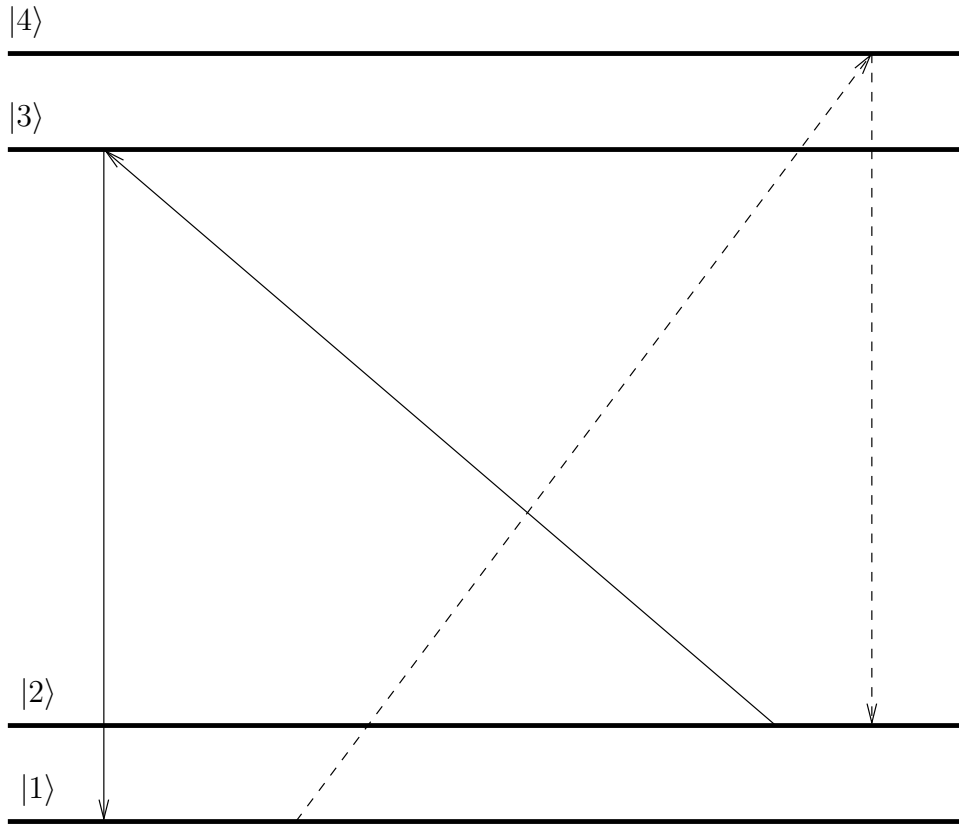


Figure A.2: Positive (solid line) and negative (dashed line) polarization enhancement. Notations for energy levels are explained in Figure A.1.

where  $\gamma$  is the nuclear gyromagnetic ration,  $J$  is the spin of the species being measured, and  $N$  is the spin density of the material. To measure the absorption signal one places an inductor (NMR coil) into the target material. Due to the interaction with the target material the inductance of the coil changes and becomes

$$L(\omega) = L_0 [1 + 4\pi\eta\chi(\omega)], \quad (\text{A.8})$$

where  $L_0$  is the inductance of the coil with unpolarized material and  $\eta$  is the filling factor, describing the coupling between the material and the NMR coil. The

impedance of the coil is in its turn measured by including the coil into a resonant LCR circuit tuned to the Larmor frequency of the deuteron.

# Appendix B

## Measuring beam polarization with the Hall C Møller polarimeter

Møller measurements employ polarized electron-electron scattering for determination of the beam polarization. Since Møller scattering is a pure QED process, the analyzing power can be calculated to a very high accuracy, thus makes possible very accurate polarization measurements.

For the longitudinal polarization of both beam ( $P_b$ ) and target ( $P_t$ ) spins the scattering cross-section in the center-of-mass quantities is [47]:

$$\frac{d\sigma}{d\Omega} = \left( \frac{d\sigma}{d\Omega} \right)_0 [1 + P_t P_b A_{zz}(\theta)], \quad (\text{B.1})$$

where  $(\frac{d\sigma}{d\Omega})_0 = (\alpha(3 + \cos^2 \theta)/(2E \sin^2 \theta))^2$  is the unpolarized scattering cross section,  $\alpha$  is the fine structure constant,  $E$  and  $\theta$  are the incident electron energy and the scattering angle in the center-of-mass frame, and  $A_{zz}(\theta) = -\sin^2 \theta(8 - \sin^2 \theta)/(4 - \sin^2 \theta)^2$  is the analyzing power. The analyzing power reaches a maximum of  $-\frac{7}{9}$  at  $90^\circ$ . Therefore, the detectors are arranged such that to emphasize this kinematic

region. The  $A_{zz}$  needs to be corrected for the Levchuk effect [145] which takes into account the initial motion of the atomic electrons.

The Equation B.2 gives the expression for the beam-target asymmetry:

$$\epsilon = \frac{N_+ - N_-}{N_+ + N_-} = \overline{A_{zz}} P_b P_t, \quad (\text{B.2})$$

which can be rewritten for the beam polarization as follows:

$$P_b = \frac{\epsilon}{\overline{A_{zz}} P_t}. \quad (\text{B.3})$$

Here  $\overline{A_{zz}}$  is the acceptance averaged analyzing power. From the Equation B.3 one can see that the error on the beam polarization has statistical contributions from the Møller counts and Monte Carlo statistics, and a systematic contribution (Monte Carlo systematics and the target polarization).

The systematic error is dominated by the Levchuk effect, which is 10% relative with the size of the effect about 3%, i.e. the contribution is 0.3%. The spin polarization in iron is known to 0.25%. Other systematic uncertainties (multiple scattering, beam position and direction, target field value and orientation etc.) are small ( $\leq 0.15\%$ ). The overall systematic error was found to be 0.47% [47].

# Bibliography

- [1] F. Cardarelli and S. Simula, Phys. Rev. **C62**, 065201 (2000).
- [2] J. Kelly, Advances in Nuclear Physics **23**, 75 (1996).
- [3] R. Sachs, Phys. Rev. **126**, 2256 (1962).
- [4] A. W. Thomas and W. Weise, *The Structure of the Nucleon* (Wiley-VCH, Berlin, 2001).
- [5] J. J. Kelly, Phys. Rev. **C66**, 065203 (2002).
- [6] X. Ji, Phys. Lett. **B254**, 456 (1991).
- [7] G. Holzwarth, Z. Phys. **A356**, 339 (1996).
- [8] A. Licht and A. Pagnamenta, Phys. Rev. **D2**, 1156 (1970).
- [9] A. Mitra and I. Kumari, Phys. Rev. **D15**, 261 (1977).
- [10] S. Kopecky *et al.*, Phys. Rev. Lett. **74**, 2427 (1995).
- [11] N. Isgur, Phys. Rev. Lett. **83**, 272 (1999).
- [12] R. Hofstadter and C. de Vries, Phys. Rev. Lett. **6**, 290 (1961).

- [13] A. Lung *et al.*, Phys. Rev. Lett. **70**, 718 (1993).
- [14] W. Bartel *et al.*, Phys. Lett. **39B**, 407 (1972).
- [15] K. Hanson *et al.*, Phys. Rev. **D8**, 753 (1973).
- [16] S. Galster *et al.*, Nucl. Phys. **B32**, 221 (1971).
- [17] D. Drickey and L. Hand, Phys. Rev. Lett. **9**, 521 (1962).
- [18] B. Grossetête, Phys. Rev. **141**, (1966).
- [19] D. Benaksas, Phys. Rev. **148**, 1327 (1966).
- [20] G. Simon *et al.*, Nucl. Phys. **A364**, 285 (1981).
- [21] S. Platchkov *et al.*, Nucl. Phys. **A508**, 343 (1990).
- [22] R. Schiavilla and I. Sick, Phys. Rev. **C64**, 041002 .
- [23] G. Hoehler *et al.*, Phys. Rev. Lett. **B114**, 505 (1976).
- [24] N. Dombey, Rev. Mod. Phys. (1969).
- [25] T. Eden *et al.*, Phys. Rev. **C50**, R1749 (1994).
- [26] C. Herberg *et al.*, Eur. Phys. J. **A5**, 131 (1999).
- [27] R. Madey *et al.*, Phys. Rev. Lett. **91**, 122002 (2003).
- [28] B. Blankleider and R. Woloshyn, Phys. Rev. **C29**, 538 .

- [29] M. Meyerhoff *et al.*, Phys. Lett. **B327**, 201 (1994).
- [30] J. Becker *et al.*, Eur. Phys. J. **A6**, 329 (1999).
- [31] J. Golak *et al.*, Phys. Rev. **63**, 034006 (2001).
- [32] D. Rohe, Phys. Rev. Lett. **83**, 4257 (1999).
- [33] J. Bermuth *et al.*, Phys. Lett. **B564**, 199 (2003).
- [34] H. Zhu *et al.*, Phys. Rev. Lett. **87**, 1 (2001).
- [35] Passchier *et al.*, Phys. Rev. Lett. **82**, 4988 (1999).
- [36] H. Arenhövel, W. Leidemann, and E. Tomusiak, Phys. Rev. **C46**, 455 (1992).
- [37] H. Arenhövel, private communication.
- [38] W. Fabian and H. Arenhövel, Nucl. Phys. **A314**, 253 (1979).
- [39] H. Arenhövel *et al.*, Phys. Rev. **C61**, 034002 (2000).
- [40] H. Zhu, Ph.D. thesis, University of Virginia, 2000.
- [41] C. M. Harris, Ph.D. thesis, University of Virginia, 2001.
- [42] C. Sinclair, Technical Report No. TN-97-021, TJNAF (unpublished).
- [43] C. Yan, P. Adderley, *et al.*, Nucl. Inst. Meth. **A365**, 261 (1995).
- [44] D. Neuffer, C. Yan, and R. Carlini, Technical Report No. TN-92-054, TJNAF (unpublished).

- [45] P. Gueye, E. Joe, and R. Wallace, Status of the actual beam position monitors in the Hall C beamline, TJNAF Technical Report, 1995, unpublished.
- [46] D. Mack, private communication.
- [47] M. Hauger *et al.*, nucl-ex/9910013, 1999.
- [48] C. Yan, Technical Report No. TN-97-004, TJNAF (unpublished).
- [49] C. Yan, Technical Report No. TN-97-036, TJNAF (unpublished).
- [50] P. McKee, Ph.D. thesis, University of Virginia, 2000.
- [51] D. Crabb and D. Day, Nucl. Instr. Meth. **A356**, 9 (1995).
- [52] P. McKee, Offline target polarization analysis, TJNAF Technical Report, unpublished.
- [53] P. Mckee, in *Proceedings of the 15th International Spin Physics Symposium* (World Scientific, Singapore, 2002), to be published.
- [54] H. Mkrtchyan, Laser Pulser Gain Monitoring System in Hall C, TJNAF Technical Report, unpublished.
- [55] G. Warren, Neutron detector gain matching with cosmics, TJNAF Technical Report, 1998, unpublished.
- [56] J. R. Arrington, Ph.D. thesis, California Institute of Technology, 1998.
- [57] *CEBAF On-line Data Acquisition*, CEBAF, 1993.

- [58] F. Wesselmann, Gen01 syncfilter preprocessor, TJNAF Technical Report, unpublished.
- [59] S. Wood, The CEBAF Test Package: A Symbolic and Dynamic Test, Histogram, and Parameter Package for On- and Off-line Particle Physics Data Analysis, TJNAF Technical Report, unpublished.
- [60] D. Dutta, Ph.D. thesis, Northwestern University, 1999.
- [61] J. Lightbody and J. O'Connell, Computers in Physics 57 (1988).
- [62] F. Krautschneider, Ph.D. thesis, Bonn University, 1976.
- [63] M. Frodyma *et al.*, Phys. Rev. **C 47**, 1599 .
- [64] S. Stein, E. Bloom, *et al.*, Phys. Rev. D **12**, 1884 (1975).
- [65] L. Mo and Y. Tsai, Rev. Mod. Phys. **41**, (1969).
- [66] D. Day *et al.*, Phys. Rev. Lett. **59**, 427 (1987).
- [67] L. B. Weinstein, Ph.D. thesis, Massachusetts Institute of Technology, 1988.
- [68] T. De Forest, Nucl. Phys. **A392**, 232 (1983).
- [69] V. P. R. Schiavilla and R. Wiringa, Nucl. Phys. **A449**, 219 (1986).
- [70] P. Ulmer, *MCEEP: Monte Carlo for Electro-Nuclear Coincidence Experiments*, version 3.5 ed., Old Dominion University, 2000.

- [71] R. Madey *et al.*, Nucl. Inst. Meth. **161**, 439 (1979).
- [72] R. Brun, O. Couet, C. Vandoni, and P. Zanmarini, *PAW Users Guide, Program Library Y250* (CERN, Geneva, 1991).
- [73] G. Kubon, Ph.D. thesis, University Basel, 1999.
- [74] M. Zeier, Contamination by multi step reactions in GEn01, TJNAF Technical Report, 2003, unpublished.
- [75] G. Kubon, Phys. Lett. **B524**, 26 (2002).
- [76] S. Brodsky and G. Farrar, Phys. Rev. **D11**, 1309 (1975).
- [77] P. G. Lepage and S. J. Brodsky, Phys. Rev. **D22**, 2157 (1980).
- [78] M. Burkardt, X. Ji, and F. Yuan, Nucl. Phys. **B652**, 383 .
- [79] A. Belitsky, X. Ji, and F. Yuan, Phys. Rev. Lett. **91**, 092003 (2003).
- [80] G. Lepage and S. Brodsky, Phys. Rev. Lett. **43**, 545 (1979).
- [81] L. Andivahis, Phys. Rev. **D50**, 5491 (1994).
- [82] R. Walker *et al.*, Phys. Rev. **D49**, 5671 (1994).
- [83] A. Sill *et al.*, Phys. Rev. **D48**, 29 (1993).
- [84] P. Bosted *et al.*, Phys. Rev. Lett. **68**, 3841 (1992).
- [85] P. Bosted *et al.*, Phys. Rev. **C42**, 38 (1990).

- [86] R. Walker *et al.*, Phys. Lett. **B224**, 353 (1989).
- [87] N. Isgur and C. Llewelyn Smith, Phys. Rev. Lett. **52**, 1080 (1984).
- [88] C. E. Carlson and F. Gross, Physical Review **D36**, 2060 .
- [89] V. Punjabi *et al.*, nucl-ex/0307001.
- [90] O. Gayou *et al.*, Phys. Rev. Lett. **88**, 092301 (2002).
- [91] O. Gayou *et al.*, Phys. Rev. **C64**, 038202 (2001).
- [92] J. Arrington, Phys. Rev. **C68**, 034325 (2003).
- [93] P. Blunden, W. Melnitchouk, and J. Tjon, Phys. Rev. Lett. **91**, 142304 (2003).
- [94] P. Guichon and M. Vanderhaeghen, Phys. Rev. Lett. **91**, 142303 (2003).
- [95] J. Ralston and P. Jain, hep-ph/0302043.
- [96] V. Chernyak, hep-ph/9906387v2.
- [97] J. Ralston and P. Jain, hep-ph/9212243.
- [98] G. Miller, Phys. Rev **C66**, 065205 (2002).
- [99] V. Braun *et al.*, Nucl. Phys. **B589**, 381 (2000).
- [100] P. Mergell, U.-G. Meißner, and D. Drechsel, Nucl. Phys. **A596**, 367 .
- [101] W. R. Frazer and J. R. Fulco, Phys. Rev. **117**, 1603 .

- [102] J. Sakurai, *Currents and mesons* (University of Chicago Press, Chicago, 1969).
- [103] Y. Nambu, Phys. Rev. **106**, 1366 (1957).
- [104] M. Gari and W. Krümpelmann, Z. Phys. **A 322**, 689 (1985).
- [105] S. Okubo, Phys. Lett. **5**, 165 (1963).
- [106] G. Zweig, CERN Report Nos. TH-401 and TH-412, 1964.
- [107] J. Iizuka, Prog. Theor. Phys. Suppl. **37-38**, 21 (1966).
- [108] J. Iizuka *et al.*, Prog. Theor. Phys. **35**, 1061 (1966).
- [109] M. Gari and W. Krümpelmann, Phys. Lett. **B 274**, 159 (1992).
- [110] E. L. Lomon, Phys. Rev. **C64**, 035204 .
- [111] M. Gell-Mann, Phys. Lett. **8**, 214 (1964).
- [112] K. Barnes, P. Carruthers, and F. von Hippel, Phys. Rev. Lett. **14**, 82 (1965).
- [113] N. Isgur, G. Karl, and D. Sprung, Phys. Rev. **D23**, 163 (1981).
- [114] P. Dirac, Rev. Mod. Phys. **21**, 392 (1949).
- [115] V. Berestetskiy and M. Terentiev, Sov. J. Nucl. Phys. **25**, 347 (1977).
- [116] P. Chung and F. Coester, Phys. Rev. **D44**, 229 (1991).
- [117] S. Brodsky *et al.*, in *Particles and fields 2*, edited by A. Capri and A. Kamal (Plenum, New York, 1983), p. 143.

- [118] F. Cardarelli and S. Simula, Phys. Lett. **B467**, 1 (1999).
- [119] S. Simula, nucl-th/0105024.
- [120] S. Capstick and N. Isgur, Phys. Rev. **34**, 2808 (1986).
- [121] R. Wagenbrunn, B. S., K. W., *et al.*, Phys. Lett. **B511**, 33 (2001).
- [122] Y. Suzuki and K. Varga, *Stochastic Variational Approach to Quantum-Mechanical Few-Body Problems* (Springer-Verlag, Berlin, 1998).
- [123] M. Anselmino, P. Kroll, and B. Pire, Z. Phys. **C36**, 89 (1987).
- [124] J. Björken and S. Drell, *Relativistic Quantum Mechanics* (McGraw-Hill, New York, 1964).
- [125] P. Kroll, M. Schürmann, and W. Schweiger, Z. Phys. **A 338**, 339 (1991).
- [126] B.-Q. Ma, D. Qing, and I. Schmidt, Phys. Rev. **C65**, 035205 (2002).
- [127] D. Ahluwalia and M. Sawicki, Phys. Rev. **D47**, 299 (1993).
- [128] T. H. R. Skyrme, Nucl. Phys. **31**, 556 (1962).
- [129] G. Adkins, C. Nappi, and E. Witten, Nucl. Phys. **B228**, 552 (1983).
- [130] E. Braaten, S.-M. Tse, and C. Willcox, Phys. Rev. Lett. **56**, 2008 (1986).
- [131] G. Holzwarth, hep-ph/0201138.
- [132] T. Janssens *et al.*, Phys. Rev. **142**, (1966).

- [133] C. Berger *et al.*, Phys. Lett. **B35**, 87 (1971).
- [134] W. Bartel *et al.*, Nucl. Phys. **B58**, 429 (1973).
- [135] P. Markowitz *et al.*, Phys. Rev. **48**, R5 (1993).
- [136] H. Anklin *et al.*, Phys. Lett. **B336**, 313 (1994).
- [137] H. Anklin *et al.*, Phys. Lett. **B428**, 248 (1998).
- [138] W. Xu *et al.*, Phys. Rev. Lett. **85**, 2900 (2000).
- [139] J. Litt *et al.*, Phys. Lett. **31**, 40 (1970).
- [140] M. Jones *et al.*, Phys. Rev. Lett. **84**, 1398 (2000).
- [141] M. Ostrick *et al.*, Phys. Rev. Lett. **83**, 276 (1999).
- [142] M. M. Kaskulov and P. Grabmayr, nucl-th/0308015v1.
- [143] J. Friedrich and T. Walker, hep-ph/0303054v2.
- [144] B. Adeva *et al.*, Nucl. Instr. and Meth. **A349**, 334 (1994).
- [145] L. Levchuk, Nucl. Instr. and Meth. **A394**, 496 (1994).